Direct observation of
mode-selective phonon excitation for bulk material
by MIR-FEL

Kyohei Yoshida

Abstract

Coherent control of lattice vibrations (using mode-selective phonon excitation: MSPE) in a bulk material is an important tool for developing functional devices for the generation of energy and reduction of energy consumption (e.g., solar cells, photocatalysts, superconductors, *etc*.). This is because MSPE can yield clear information about a particular phonon that plays a significant role in the physical properties of the material. A mid-infrared (MIR) pulse laser has been suggested for selective resonant excitation of a phonon mode in the MIR region. However, MSPE of a bulk material by an MIR pulse laser has not yet been directly demonstrated. Thus, this thesis aims to demonstrate MSPE of a bulk material using an MIR pulse laser via anti-Stokes Raman scattering spectroscopy.

To this end, the Kyoto University Free Electron Laser (KU-FEL) was selected as the light source, because it can radiate light with high power and a pulse shorter than the relaxation of a phonon in the MIR region. Additionally, the wavelength of the KU-FEL can be changed continuously and quickly over a wide tunable range from 5 to 20 μm, which corresponds to the resonant absorption wavelength of phonons. Therefore, the KU-FEL is suitable for direct observation of MSPE. However, the experimental apparatus for the KU-FEL application needed to be prepared.

To use the KU-FEL, the construction of a free electron laser (FEL) beam transportation line was required to transport the FEL beam from the out-coupling hole to user stations. For efficient FEL beam transportation, the FEL beam propagation was calculated and the beam sizes at the user stations were estimated. Afterwards, the beam size in the FEL transportation line was measured and evaluated. Finally, FEL transportation ratios through user stations A (transportation distance: 12 m) and B

(transportation distance: 24 m) were measured at an FEL wavelength of 12 μm to confirm the effectiveness of the constructed FEL beam transportation system.

Because water vapor and carbon dioxide (CO_2) absorb light in the MIR region, the FEL beam transportation line was covered by plastic pipes filled with nitrogen (N_2) gas. To confirm that the N_2 gas filling efficiently prevented loss to absorption by air in the FEL beam transportation system, the spectra with and without the N_2 gas filling were compared. Additionally, the difference in the transportation ratios between the cases with and without the N_2 gas filling was measured.

Before the MSPE study, the spectrum of the visible region of FEL was measured to check for the contamination of high harmonics induced by the effect of microbunching of the electron beam because the high harmonic photons may prevent the MSPE measurement by producing unexpected peaks.

After these preparations, MSPE of a bulk material by an MIR pulse laser was demonstrated. A bulk single-crystal silicon carbide (semi-insulator 6H-SiC : SiC) and a second harmonic of an Nd-YAG laser were used as the sample and the light source, respectively, for anti-Stokes Raman scattering spectroscopy, which can directly observe the phonon status. The KU-FEL beam and a second harmonic of an Nd-YAG laser were applied to the sample, which was cooled down to 14 K to prevent non-mode-selective phonon excitations due to thermal effects.

Thus, the FEL beam transportation line was constructed and the transportation ratios through user stations A and B were found to be 87% and 73%, respectively. Additionally, it was confirmed that the N_2 gas filling prevented the absorption of the MIR-FEL beam by air, and the transportation ratio with the N_2 gas filling was three times that without the N_2 gas filling. It was confirmed that high harmonics, up to the

10th, were contaminated in the FEL beam, and it was found that a long-pass filter was essential to prevent this contamination in the measurements. Finally, irradiation of SiC by an MIR-FEL, whose photon energy corresponds to the photon-absorption energy of a particular phonon mode, and an Nd-YAG laser at 14 K produced a peak in the Raman shift corresponding to a photon energy of 119 meV (10.4 μm).

Consequently, MSPE of a bulk material by the KU-FEL was successfully observed via anti-Stokes Raman scattering spectroscopy. From this result, it was shown that it was possible to excite a specific phonon mode by an MIR pulse laser. This will aid in the development of functional materials by clarifying the role of a particular phonon in the physical properties of a material.

Contents

1 Introduction

1-1 Background

The coherent control of a particular molecular vibration or a lattice vibration [using selective excitation of a molecular vibration (SEMV), or mode-selective phonon excitation (MSPE)] is an attractive tool for material development and research in solid-state physics, chemistry, and medicine. A mid-infrared (MIR) pulse laser is used for SEMV and MSPE because the MIR region of light corresponds to the absorption wavelength of the molecular vibration.

SEMV using an MIR pulse laser has been investigated or employed for applications in environmental chemistry, medicine, analytical chemistry, and so on. For example, the isomerization of a chemical substance without any reagent [1] and the control of the chemical reaction path [2] using SEMV have been reported. In addition, the selective dissociation of a particular chemical bond is possible via multiphoton dissociation induced by SEMV. For instance, the selective remove of harmful substances (*e.g.*, Freon, dioxins, PCB, *etc.*) in air or soil has been reported [3, 4]. The selective removal of cholesterol ester from the human body has been also reported as a medical application of SEMV [5]. As an example of a practical application, selective dissociation by SEMV has been employed in infrared multiphoton dissociation, a mass spectroscopy technique for chemical analysis [6].

In addition to SEMV, MSPE in solid materials is important. For example, ultrafast dynamics (*e.g.*, electron–phonon interaction or phonon–phonon interaction) affect the physical properties of solid materials (*e.g.*, electron mobility). Especially, the physical property of the bulk material affects the performance of the devices. Therefore, study of ultrafast dynamics of the bulk material is essential for the development of the solid material devices. MSPE will be a powerful tool to study ultrafast dynamics because it can be used to control the state of a particular phonon mode [7]. Additionally, MSPE can be used as a tool to control electronic, magnetic, and structural phases of materials [8]. Phase control of a material through optical manipulation is important for developing ultrafast switching for optical communications [9]. Thus, MSPE is an attractive physical phenomenon for solid state physics.

MSPE can be observed through two methods: coherent phonon generation (CPG) by a typical ultrafast laser (*e.g.*, a Ti:sapphire laser), and resonant excitation of the infrared-active phonon mode by an MIR pulse laser.

MSPEs observed via CPG have been reported for strongly correlated electron systems, super-lattices, nanomaterials, semiconductors, *etc*. [7, 10–17]. Takahashi et al. used CPG to control the lattice vibrations of Ba–O and Cu–O in chemical bonds of $YBa_2Cu_2O_{7-\delta}$, which is a superconductive material [12]. As examples of MSPE of semiconductors, Yee *et al.* and Kasai *et al.* demonstrated MSPE of the E1 mode in GaN and of an optical phonon mode in ZnTe, respectively [7, 11]. Hurley *et al.* found that the acoustic mode in GaAs can be selectively excited [10]. Hase *et al.* and Kawanabe *et al.* both demonstrated MSPE of metals using CPG: Hase *et al.* selective excited Bi-Bi chemical bond [15, 16], and Kawanabe *et al.* selectively excited the Cs-Pt stretching mode in a Pt surface covered with submonolayer cesium atoms [17]. Additionally, Kim *et al.* and Heinecke *et al.* observed MSPE of carbon nanotubes and a GaAs/AlAs super lattice, respectively [13, 14].

There are two main types of mechanism for MSPE via CPG. One is the displacive excitation of coherent phonon [18], which has been adopted for non-transparent materials such as semiconductors. The other is impulsive stimulated Raman scattering (ISRS) [19]. Coherent phonons in transparent materials are generated by ISRS. In both mechanisms, the excited phonon mode depends on the pulse conditions of the ultrashort laser. For example, a pulse width of 6 fs is necessary to excite a vibration mode at 2000 cm^{-1} (absorption wavelength: 5 μm) [20], while a shorter pulse width is required to excite a higher energy phonon mode. In addition, for MSPE via CPG, the pulse conditions of the ultrashort pulse laser must be optimized to a specific pulse width or a specific repetition rate so that the repetition rate matches the phonon mode frequency [15]. Therefore, MSPE via CPG has been used to selectively excite phonons mainly in the terahertz domain, which corresponds to phonon modes of low energy.

For MSPE in the MIR region (5–25 μm), the resonant excitation of the infrared-active phonon mode by an MIR pulse laser has been examined. This method resonantly excites a phonon mode via the absorption of photons whose energy corresponds to the phonon energy. Rini *et al.* used an MIR pulse laser to irradiate $Pr_{0.7}Ca_{0.3}MnO_3$, which is a strongly-correlated electron system, to selectively excite the vibration mode of the Mn–O chemical bonds [8], and observed a metal–insulator transition phenomenon induced by MSPE. In addition, Forst *et al.* controlled the magnetism of $La_{0.5}Sr_{1.5}MnO_4$ and experimentally demonstrated ionic Raman scattering by MSPE with an MIR pulse laser [21, 22]. In this manner, a phenomenon induced by MSPE with an MIR pulse laser has been observed in strongly correlated electron systems.

Although MSPE by an MIR pulse laser has been indirectly demonstrated through the observation of phenomena induced by MSPE, MSPE in a bulk material using an

MIR pulse laser has not yet been demonstrated directly for the following reasons. An MIR pulse laser with a pulse width less than a picosecond (several hundred femtoseconds) is required for MSPE to prevent thermal excitation, but such an MIR pulse laser is expensive and has not yet been generalized. Secondly, the present main objective of MSPE is to create a tool to control the material phase via optical manipulation. Therefore, MSPE by an MIR pulse laser as a tool to investigate the ultrafast dynamics in solid materials has not been a focus of research, in spite of the importance of investigating ultrafast dynamics. In addition, direct observation of MSPE by an MIR pulse laser using a conventional method is difficult. Generally, a pump–probe experiment is conducted to observe the MSPE. Therefore, precise synchronization between a pump laser (an MIR pulse laser with a pulse width on a femtosecond order) and a probe laser (a Ti:sapphire laser) is required (on a femtosecond scale). Such an experimental setup is complex and difficult.

For these reasons, it is considered that MSPE in a bulk material by an MIR pulse laser has not yet been demonstrated directly. Thus, the objective of this research is to directly demonstrate MSPE in a bulk material using an MIR pulse laser. In Chapter 2, phonons, phonon spectroscopy, and the mechanism of the method for MSPE are described.

1-2 **Light source for MSPE**

For the light source of an MIR pulse laser, optical parametric generation, an optical parametric oscillator, difference frequency generation (DFG), and a free electron laser (FEL) are all considered. Although a quantum cascade laser (QCL) is a compact MIR light source, the pulse width of the QCL is on the picosecond scale, which is too long for MSPE [23]. To prevent thermal effects due to laser irradiation, the pulse width for MSPE must be less than the period for phonon decay time, which is on the sub-picosecond scale. The development of an MIR pulse laser with a solid medium has advanced, and a tunable MIR femtosecond laser via DFG with a tunable wavelength from 5 to 20 μm is commercially available. Additionally, an MIR-FEL has been developed as a light source. The MIR-FEL was employed for MSPE because of its unique characteristics (*e.g.*, tunable wavelength, high power, and short pulse). The main difference between a conventional MIR pulse laser and the MIR-FEL (the Kyoto University Free Electron Laser (KU-FEL)) is the power (peak power and average power) and the pulse structure. An FEL does not use a nonlinear optical material to tune the wavelength. Therefore, the peak power and average power of an FEL are not limited by the damage threshold of a nonlinear optical material, and the FEL can operate with high peak power and high average power. In addition, an FEL has unique pulse structures, called macropulses and micropulses. A macropulse in the KU-FEL consists of several thousand micropulses. Each micropulse has an interval of 350 ps in the case of the KU-FEL. Therefore, by using the KU-FEL, multistage excitation of a phonon mode may be possible because the decay time of a particular phonon mode in a material such as amorphous silicon is on the nanosecond scale [24]. Additionally, the KU-FEL can quickly change wavelength over a wide tunable range by changing the gap of the undulator. The KU-FEL was thus selected as a light source for MSPE, owing to the advantages of the MIR-FEL (KU-FEL) in this application.

In Chapter 3, the FEL facilities and the KU-FEL are described.

1-3 Preparation of the KU-FEL for the experiment

The goal of this research is to directly demonstrate MSPE in a solid material using an MIR-FEL. Therefore, the experimental setup with the KU-FEL should be constructed. The KU-FEL was upgraded to widen its tunable wavelength. The undulator was changed from 1.6 m to 1.8 m. In addition, the out-coupling hole diameter installed at the mirror in the optical cavity was changed from 2 mm to 1 mm to reduce the out-coupling loss of the FEL optical resonator, which alters the divergence of the FEL from the out-coupling hole. An FEL quasi-parallel beam system was constructed using a spherical mirror to transport the FEL beam from the out-coupling hole to the user stations [25]. However, after the upgrade, the FEL beam was not transported effectively because the quasi-parallel beam system could not parallelize the FEL beam. Therefore, the construction of a new FEL quasi-parallel beam system was planned to transport the FEL beam effectively. The design and construction of a new FEL quasi-parallel beam system were required. In this research, the beam size of the FEL beam in the FEL beam transportation line was estimated in order to design a new FEL quasi-parallel beam system. After the estimation, the beam size of the FEL was measured and evaluated using the optics calculation software, Zemax. Finally, it was essential to confirm that the constructed FEL beam transportation system could transport the FEL beam effectively. Therefore, the FEL transportation ratio was measured.

Because light of the MIR region corresponds to the absorption wavelength of water vapor and carbon dioxide (CO_2), these gases absorbed the FEL beam as it was transported from the out-coupling hole to a user station. Therefore, it is necessary to prevent the absorption of the FEL beam by air. For this method, the optical path of the FEL beam was covered by plastic pipes, and the pipes were filled with nitrogen (N_2) gas to remove air containing water vapor and CO_2. After construction of the N_2 gas filling system, it was necessary to confirm that absorption of the MIR-FEL beam by air had been prevented. Therefore, the differences in the spectra and the transportation ratios between the cases with and without N2 gas filling were measured.

Harmonic generation of a laser is an important tool to enhance the tunable wavelength. High harmonics of the FEL beam have been reported in an optical cavity without a nonlinear optical material, owing to the effect of microbunching [26-28]. Consequently, the high harmonics from FEL have been used to investigate the electron beam quality as well as to enhance the tunable wavelength [27]. However, harmonics may prevent the application of the FEL to measure photoluminescence and Raman scattering spectra, because the light of the harmonics may contaminate the spectrum. Therefore, it is necessary to confirm the existence of the harmonics in the FEL beam. Thus, in this research, the presence of harmonics in the FEL beam and the origin of these harmonics were investigated.

The design of the FEL quasi-parallel beam system in the FEL beam transportation line, the FEL transportation ratios through user stations A and B, the investigation of the effectiveness of the nitrogen filling, and the observation of the high harmonics are all discussed in Chapter 4.

1-4 **Direct observation of MSPE**

To demonstrate MSPE, it is important to observe the states of the phonons. Generally, to demonstrate MSPE, a pump–probe experiment (Fig. 1.1) is conducted.

An ultrashort pulse laser is used as the pump and the probe light by dividing the light with a beam splitter for the pump–probe experiment. The timing between the pump and the probe light is adjusted by a translational stage. To observe the phonon state, the transient change of reflectivity or transmittance is observed because the reflectivity or the transmittance is adjusted by the phonon excitation [29]. Therefore, irradiation with an ultrashort pulse laser causes the phonon oscillation to be observed as a change in reflectivity or transmittance (Fig. 1.2). The period of a phonon oscillation (*T*) and the phonon decay time are studied from the time-resolved waveform. Additionally, the spectrum of the frequency domain was calculated via a Fourier transformation of the time-resolved waveform. The calculated spectra show the status of the phonon, which can also be provided by Raman scattering spectroscopy.

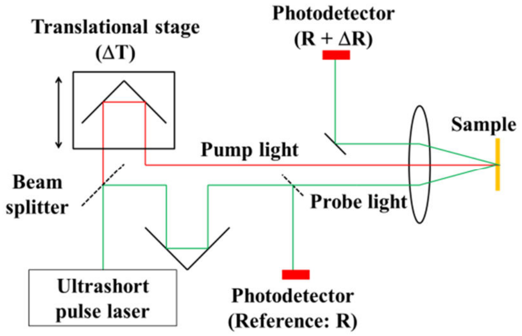

Fig. 1.1. Schematic of pump–probe experiment to observe MSPE via CPG

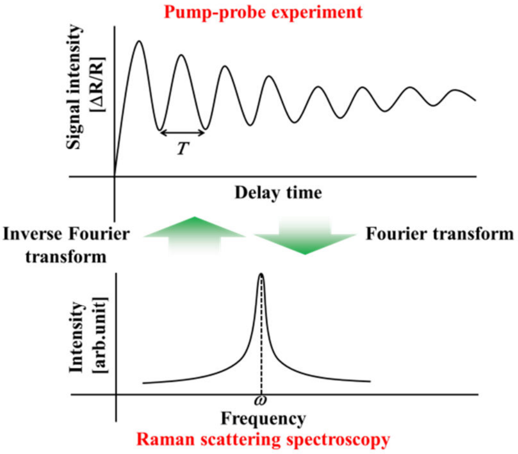

Fig. 1.2. Schematic of the observed signal in the pump–probe experiment via CPG, and the relation between the phonon pump-probe experiment (time domain measurement) and Raman scattering spectroscopy (frequency domain measurement)

However, this pump–probe experiment has several problems for the direct demonstration of MSPE by an MIR pulse laser. One is the difficulty of synchronization between a pump laser and a probe laser. Precise synchronization (on a femtosecond order) between the pump light and the probe light is required to conduct the experiments. However, this is difficult owing to the limited electrical response when an MIR-FEL is used as a pump light source, because the timing of the MIR-FEL and the probe light is controlled by an electrical trigger system. The other problem is that the pump–probe experiments cannot observe the states of phonons directly. To observe the state of a phonon using the pump–probe experiment, measurement of the waveform of the signal in the time domain is first required. After the measurement, Fourier transformation is necessary to confirm the state of the phonon. Therefore, two stages —signal observation and Fourier transformation— are required for the observation of MSPE in the conventional method.

In this research, Raman scattering spectroscopy was performed because this can observe the state of the phonon directly in one stage with easy timing control. Raman scattering spectroscopy is a type of vibrational spectroscopy. There are two types of Raman scattering: Stokes scattering and anti-Stokes scattering. Stokes scattering occurs as the result of the interaction between electrons in the ground state and the incident photons, while anti-Stokes scattering occurs as a result of the interaction between electrons in the vibrationally excited state and the incident photons. Therefore, the intensities of the Stoke scattering and the anti-Stokes scattering depend on the electron population in the ground states and vibrationally excited states, respectively. In this way, the state of a phonon can be observed directly in one stage by the observation of photons modulated by electron–photon interaction.

Next, synchronization between the pump light and the probe light is required as an experimental condition to observe MSPE through Raman scattering spectroscopy. However, precise timing control at the femtosecond scale between the pump laser and the probe laser is not required because Raman scattering spectroscopy does not observe the transient change of the phonon in the time domain. Therefore, the timing control at the nanosecond scale is sufficient in the case of Raman scattering spectroscopy, and the experimental setup and experimental conditions are easier than for the conventional pump–probe experiment.

Additionally, the temperature of the material surface, which represents the phonon population of the material, can be observed via the measurement of the intensity ratio between the Stokes scattering light and the anti-Stokes scattering light. Therefore, it may be possible to observe the population of a selectively excited phonon mode using Raman scattering spectroscopy. For these reasons, anti-Stokes Raman scattering spectroscopy was employed as a novel method to directly demonstrate MSPE by an MIR pulse laser.

Silicon carbide (SiC) was selected as a sample material for MSPE. SiC is an attractive material for various fields (electronics, solid physics, nuclear fusion, *etc.*) and it is studied to improve its physical properties (*e.g.*, electron mobility and electronic resistance). Because ultrafast dynamics play an important role in the physical properties of SiC, they must be understood in order to realize high-performance devices [30]. Thus, MSPE technology is required for such ultrafast dynamics. The phonon modes in SiC absorb photons in the MIR region. Additionally, SiC is a chemically and mechanically stable material, and it has high damage threshold for a pulse laser. Therefore, SiC is a suitable material for demonstration of MSPE by an MIR pulse laser, and thus it is selected as the sample material in this research.

In Chapter 5, the results of the direct demonstration of MSPE for SiC by a MIR pulse laser with anti-Stokes Raman scattering spectroscopy are described.

1-5 **Importance of this work**

This experiment is the first to apply the KU-FEL to solid-state physics. To do that, it was required to setup the experimental environment for KU-FEL users. In this research, the experimental environment of KU-FEL has been prepared.

Moreover, in this work, it can be confirmed that a specific phonon can be excited by irradiation by an MIR pulse laser. Therefore, the application of MSPE will enhance fundamental research in condensed matter physics, such as the role of a particular phonon mode in the physical properties of a solid material, the phase control of materials exhibiting metal–insulator transition, superconductivity, *etc*. Such fundamental research will aid the development of functional materials (*e.g.*, photocatalysts, solar cells, super conductive materials, *etc.*).

2 Vibrational spectroscopy and method for MSPE

2-1 Introduction

In this chapter, information and background crucial to this research are described. Section 2-2 introduces the concept of phonons, while Section 2-3 discusses vibrational spectroscopy methods. Section 2-4 presents overviews of the two mode-selective phonon excitation (MSPE) methods. Finally, Section 2-5 specifies the light source for the mid-infrared (MIR) region.

2-2 **Phonons**

2-2-1 **Lattice consisting of one atom**

To discuss a phonon, first consider the case of a one-dimensional lattice that consists of only one type of atom, where the atoms are connected by springs. (Fig. 2.1).

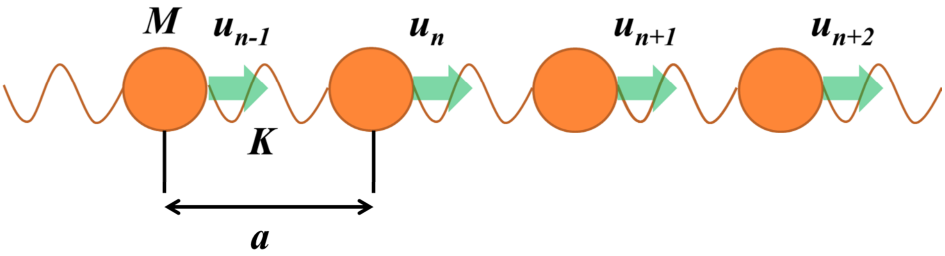

Fig. 2.1. Schematic of a one-dimensional lattice consisting of one atom.

In the figure, K is the spring constant, a is the lattice constant, M is the mass of the atom, u_n is the displacement from an equilibrium position of the nth atom. By using these parameters, $\frac{\boldsymbol{d}^2\boldsymbol{u_n}}{\boldsymbol{dt}^2}$, which is the equation for a simple harmonic motion, can be expressed as:

$$\boldsymbol{M}\frac{\boldsymbol{d}^2\boldsymbol{u_n}}{\boldsymbol{dt}^2} = \boldsymbol{K}\left(\boldsymbol{u_{n+1}} + \boldsymbol{u_{n-1}} - 2\boldsymbol{u_n}\right)\cdot \tag{1}$$

The total number of the atoms is defined as *N*.

From the periodic boundary condition, the following relation is extracted:

$$u_n = u_{n+N}\,. \tag{2}$$

Thus, the equation of motion for a simple harmonic motion can be expressed as:

$$\frac{\boldsymbol{d}^2\boldsymbol{u_n}}{\boldsymbol{dt}^2} = -\omega^2\boldsymbol{u_n}, \tag{3}$$

where ω is the vibration frequency.

In this case, the solution of u_n is:

$$u_n = u\exp(-i\omega t)\exp(ikna)\,. \tag{4}$$

where *k* is the wavenumber, and its value is determined by the periodic boundary condition as:

$$k = \frac{2\pi n}{aN},\ n = 0, \pm 1, \pm\left(\frac{N}{2} - 1\right), \pm\frac{N}{2}\,. \tag{5}$$

Substituting Eqs. (3) and (4) into Eq. (1) gives:

$$\begin{aligned}
&M\frac{d^2u_n}{dt^2} = K\left(u_{n+1} + u_{n-1} - 2u_n\right)\\
&-M\omega^2 u\exp(-i\omega t)\exp(ikna) =\\
&K\{u(-i\omega t)\exp[ik(n+1)a] + u(-i\omega t)\exp[ik(n-1)a] - 2u\exp(-i\omega t)\exp(ikna)\}\\
&-M\omega^2 = K(\exp(ika) + \exp(-ika) - 2)
\end{aligned}$$

Here, by using the relation:

$$\cos\theta = \frac{\exp(i\theta) + \exp(-i\theta)}{2} \text{ and } \sin^2\left(\frac{\theta}{2}\right) = \frac{1-\cos(\theta)}{2}$$

then:

$$M\omega^2 = 4K(2 - 2\cos ka) \tag{6}$$

$$M\omega^2 = 4K\sin^2\left(\frac{ka}{2}\right).$$

Figure 2.2 shows the dispersion curve using Eq. (6), while Fig. 2.3 schematically depicts the lattice vibration of one atom in one dimension. As shown in Fig. 2.3, when k is π/a, the wavelength of the oscillation (λ) becomes $2a$, because k is 2π/λ. When k is close to 0, the wavelength of the oscillation becomes almost infinite, indicating that the oscillation in space diminishes and that all the lattice points oscillate uniformly (Fig. 2.3).

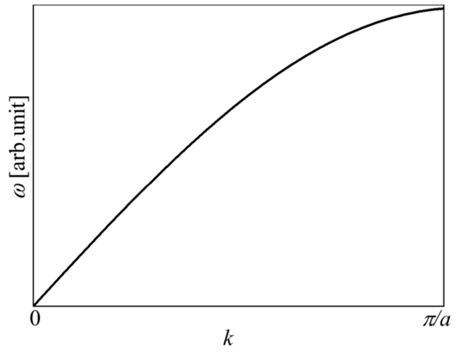

Fig. 2.2. Dispersion curve of a one-dimensional lattice consisting of one atom.

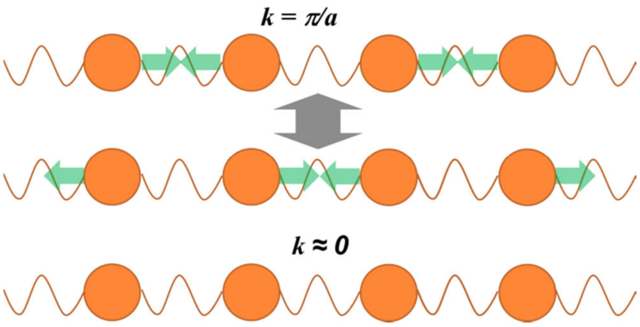

Fig. 2.3. Schematic of a one-dimensional lattice vibration composed of one type of atom.

2-2-2 **Lattice consisting of two atoms**

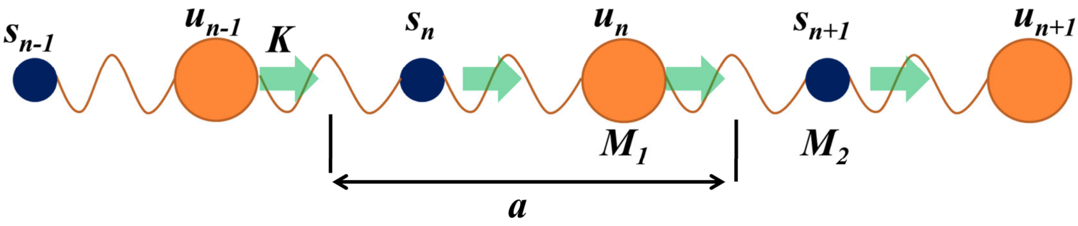

Fig. 2.4. Schematic of a one-dimensional lattice consisting of two types of atoms.

Next, consider the case of a one-dimensional lattice composed of two different atoms (Fig. 2.4). Here, s_n and u_n are the displacement of the nth unit cells, M_1 and M_2 are the masses of the atoms, K is the spring constant, and a is the lattice constant. These conditions give the following equations of motion:

$$M_1 \frac{d^2 u_n}{dt^2} = K(s_{n+1} + s_n - 2u_n) \quad \text{and} \tag{7}$$

$$M_2 \frac{d^2 s_n}{dt^2} = K(u_n + u_{n-1} - 2s_n). \tag{8}$$

By the periodic boundary condition and the equation of motion for simple harmonic oscillation, the following equations are derived similar to Section 2-2-1, where *ω* is the vibration frequency:

$$u_n = u\exp(-i\omega t)\exp(ikna) \quad \text{and} \tag{9}$$

$$s_n = s\exp(-i\omega t)\exp(ikna) \tag{10}$$

Substituting Eqs. (9) and (10) into Eqs. (7) and (8) yields,

$$\begin{aligned}
&M_1\frac{d^2u_n}{dt^2} = -\omega^2 M_1 u\exp(-i\omega t)\exp(ikna) \\
&= K\{s\exp(-i\omega t)\exp[ik(n+1)a] \\
&+ s\exp(-i\omega t)\exp(ikna) - 2u\exp(-i\omega t)\exp(ikna)
\end{aligned}$$

The following equation is extracted:

$$\begin{aligned}
&-u\omega^2 M_1 = K(s\exp(ika) + s - 2u) \\
&(2K - \omega^2 M_1)u - K[\exp(ika)+1]s = 0
\end{aligned} \tag{11}$$

$$\begin{aligned}
&M_2\frac{d^2s_n}{dt^2} = -\omega^2 M_2 s\exp(-i\omega t)\exp(ikna) \\
&= K\{u\exp(-i\omega t)\exp(ikna) \\
&+ u\exp(-i\omega t)\exp[ik(n-1)a] - 2s\exp(-i\omega t)\exp(ikna).
\end{aligned}$$

The following equation is extracted:

$$\begin{aligned}
&-s\omega^2 M_2 = K(u + u\exp(-ika) - 2s) \\
&-K[1+\exp(-ika)]u + (2K - \omega^2 M_2)s = 0.
\end{aligned} \tag{12}$$

If the following relation holds, then Eqs. (11) and (12) can be solved:

$$\begin{vmatrix} 2K - \omega^2 M_1 & -K[\exp(ika)+1] \\ -K[1+\exp(-ika)] & 2K - \omega^2 M_2 \end{vmatrix} = 0\,. \tag{13}$$

From Eq. (13), the following equation is derived:

$$\omega^2{}_{\pm} = \frac{K}{M_1 M_2}\{M_1 + M_2 \pm \sqrt{(M_1+M_2)^2 - 4M_1M_2\sin^2\left(\frac{ka}{2}\right)}\}\,. \tag{14}$$

The dispersion relation calculated by Eq. (14) is shown in Fig. 2.5, where the black and red lines show the dispersion curves of *ω*+ and *ω*-, respectively. The mode *ω*+ is referred to as the optical mode and the mode ω_- is referred to the acoustic mode.

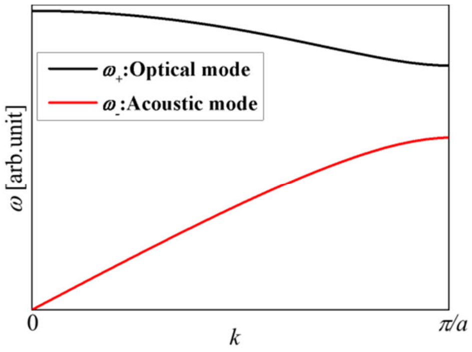

Fig. 2.5. Dispersion curves of a one-dimensional lattice composed of two different atoms.

When k is 0, the following equations hold:

$$\omega_+ = \sqrt{2K\left(\frac{1}{M_1}+\frac{1}{M_2}\right)} \quad \text{and} \tag{15}$$

$$\omega_- = 0. \tag{16}$$

Substituting Eqs. (15) and (16) into Eqs. (11) or (12) gives the motion of each phonon mode as:

$$\frac{s}{u} = -\frac{M_1}{M_2} \quad \text{and} \tag{17}$$

$$\frac{s}{u} = 1. \tag{18}$$

Equation (17) shows the motion of the optical phonon mode in which each atom moves to the opposite phase. Equation (18) shows the motion of the acoustic phonon mode in which each atom moves in the same phase. In addition to these modes, longitudinal waves and transverse waves can contribute to the vibration pattern. In total, there are four phonon modes (Fig. 2.6).

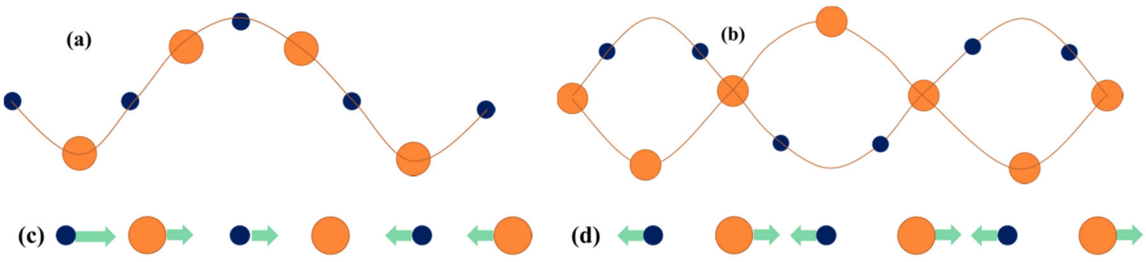

Fig. 2.6. Schematics of the motions of each phonon mode

(a): transverse acoustic mode, (b): transverse optical mode

(c): longitudinal acoustic mode, and (d): longitudinal optical mode

2-3 **Conventional methods for vibrational spectroscopy**

In this section, vibrational spectroscopies are introduced briefly.

2-3-1 **Selection rules for infrared-active and Raman-active modes**

The vibration modes (*e.g.,* frequency, lifetime, excitation state, *etc.*) can be investigated using infrared spectroscopy and Raman scattering spectroscopy. A vibration mode that absorbs infrared light is called an infrared-active phonon mode. Infrared absorption is induced by a change in the dipole moment. Therefore, materials that do not display a change in the dipole moment do not exhibit infrared absorption (*e.g.*, monoatomic molecular and mono-atomic solids). On the other hand, a vibration mode that shows a change in the polarizability experiences the so-called Raman effect, in which it gains or loses energy to/from an incident photon to produce a scattering photon, and exhibits a peak in the Raman scattering spectrum [31]. A phonon mode observed by Raman scattering is called a Raman-active mode.

An important issue in vibration spectroscopy is the mutual exclusion principle. This rule states that no phonon mode can be both infrared- and Raman-active in a crystal that possesses a center of symmetry [32]. Therefore, infrared spectroscopy and

Raman scattering spectroscopy are considered complementary, and both are necessary to investigate all the phonons in a crystal with a center of symmetry.

2-3-2 **Infrared spectroscopy**

Infrared absorption originates from a change in the dipole moment. An electromagnetic wave interacts with the dipole of a material, which is schematically depicted in Fig. 2.7. In organic chemistry, infrared absorption is an important measurement technique because it depends on the functional groups within a compound. Therefore, infrared absorption spectroscopy provides information about the chemical structure, especially, in the region below 1500 cm^{-1}, which is called the "fingerprint region". The fingerprint region can be used to identify chemicals.

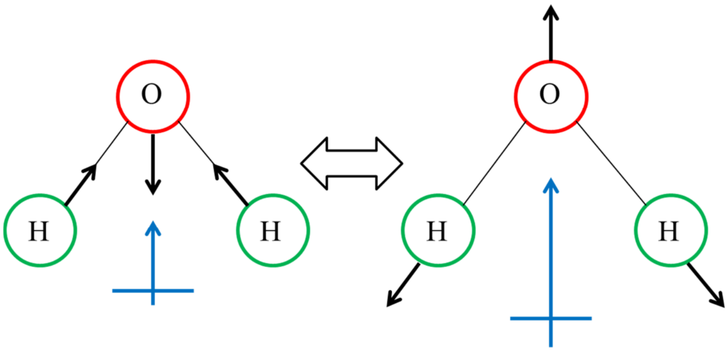

Fig. 2.7. Schematic of an example of change in dipole moment.

In the case of a solid, infrared absorption is observed for optical phonon modes because they induce a change in the dipole moment. In addition, because the electromagnetic wave is a transverse wave, only a phonon of the transverse optical mode is observed in infrared spectroscopy when infrared light is injected at an incidence perpendicular to the sample surface. To observe a longitudinal optical mode, infrared light is injected at an oblique incidence to the sample surface. In addition to infrared spectroscopy with an oblique incidence, the frequency of the longitudinal optical phonon mode can be calculated by the relationship between the transverse optical phonon mode and the longitudinal optical phonon mode (Lyddane-Sachs-Teller (LST) relationship) [32].

Infrared spectroscopy in a solid material is also used to investigate microelectronics, because the infrared energy corresponds to the shallow level created by impurities in a semiconductor, such as silicon. Infrared spectroscopy of microelectronics is performed at low temperatures to prevent thermal excitation. Impurities in semiconductors (e.g., P, As, B, and Al) have been identified by infrared spectroscopy [33].

2-3-3 **Raman spectroscopy**

2-3-3-1 **Overview of Raman scattering spectroscopy**

In 1928, Raman and Krishnan first observed Raman scattering [34]. Because Raman scattering spectroscopy can directly observe the states of molecular vibration and lattice vibration, it can be used to investigate phonon dynamics [35]. In addition, the Raman spectrum depends on the type of molecule or crystal. Therefore, Raman scattering spectroscopy has been used to identify molecules and crystals [36, 37]. There are two types of Raman scattering: Stokes scattering, and anti-Stokes scattering. The mechanisms of Stokes scattering and anti-Stokes scattering are explained in Section 2-3-3-2. This has been applied to semiconductor devices to identify the plane direction and to evaluate carrier mobility [9, 38, 39]. In addition, because the ratio between the intensity of Stokes scattering and that of anti-Stokes scattering depends on the electron population in the vibration state, which depends on temperature, Raman scattering spectroscopy can be used as a non-contact temperature sensor [40].

2-3-3-2 **Principle and theory of Raman scattering spectroscopy**

In this section, the classical theory of Raman scattering is discussed.

Light can be depicted as an electromagnetic wave.

$$\vec{E} = \vec{E}_0 \cos(2\pi\nu t - kr), \tag{19}$$

where $\vec{\boldsymbol{E}}$ is the electric field composed of electromagnetic waves, k is the wavenumber vector, t is the measurement time, $\vec{\boldsymbol{E}}_0$ is a vector representing the amplitude and polarization of the electric field. Here, k is expressed as:

$$k = \frac{2\pi\nu}{c}, \tag{20}$$

where c is the velocity of light.

Moreover, $\vec{\boldsymbol{E}}_0$ is given by:

$$\vec{E}_0 = E_0 \vec{e}, \tag{21}$$

where $\vec{e}$ is the unit vector.

These equations can be used to consider the relation between a molecule and an electromagnetic wave. When an electromagnetic wave is irradiated into a molecule, it can be expressed as:

$$\vec{E}_i = E_{i0} \vec{e} \cos(2\pi\nu_i t). \tag{22}$$

It should be noted that the origin of the coordinates ($r = 0$) is defined as the position of the molecule in Eq. (19).

Irradiating a molecule with an electromagnetic wave alters the distribution of the electron, which induces a dipole moment $\vec{\boldsymbol{P}}$. When the intensity of the electronic field is weak, $\vec{\boldsymbol{P}}$ is proportional to the intensity of the electronic field:

$$\vec{P} = \alpha \vec{E}_i = \alpha E_i \vec{e} \cos(2\pi \nu_i t) . \tag{23}$$

Because $\vec{P}$ and $\vec{E}_i$ are vectors, α becomes a second-rank tensor, which is referred to as the polarizability tensor.

In addition, a molecule vibrates periodically. Therefore, α is expressed as:

$$\alpha = \alpha_0 + \alpha_1 \cos(2\pi \nu_r t) , \tag{24}$$

where α_0 is the component that is independent of time and α_1 is the component that depends on time. Using Eq. (24), Eq. (23) can be converted into:

$$\begin{aligned} \vec{P} &= \alpha \vec{E}_i \\ &= \alpha E_i \vec{e} \cos(2\pi \nu_i t) \\ &= E_i \vec{e} [\alpha_0 + \alpha_1 \cos(2\pi \nu_r t)] \cos(2\pi \nu_i t) \\ &= E_i \vec{e} (\alpha_0 \cos(2\pi \nu_i t) + \alpha_1 \cos(2\pi \nu_i t) \cos(2\pi \nu_r t)). \end{aligned} \tag{25}$$

Using the relation:

$$\cos(\alpha)\cos(\beta) = \frac{1}{2}[\cos(\alpha+\beta) + \cos(\alpha-\beta)], \tag{26}$$

Eq. (25) can be converted as follows:

$$\begin{aligned} \vec{P} &= \alpha \vec{E}_i \\ &= \alpha E_i \vec{e} \cos(2\pi \nu_i t) \\ &= E_i \vec{e} [\alpha_0 + \alpha_1 \cos(2\pi \nu_r t)] \cos(2\pi \nu_i t) \\ &= E_i \vec{e} (\alpha_0 \cos(2\pi \nu_i t) + \alpha_1 \cos(2\pi \nu_i t) \cos(2\pi \nu_r t)) \\ &= E_i \vec{e} \left[\alpha_0 \cos(2\pi \nu_i t) + \frac{1}{2} \alpha_1 \cos\{2\pi (\nu_i - \nu_r) t\} + \frac{1}{2} \alpha_1 \cos\{2\pi (\nu_i + \nu_r) t\} \right]. \end{aligned} \tag{27}$$

Because the electric dipole in oscillation emits an electromagnetic wave, a molecule can emit three types of electromagnetic waves when irradiated by an electromagnetic wave. One type has the same frequency as the electromagnetic wave, and corresponds to the first term in Eq. (27). This type of wave is called Rayleigh scattering. The second type has a frequency lower than the electromagnetic wave, and corresponds to the second term in Eq. (27). This type of wave is called Stokes scattering. The third type has a frequency higher than the electromagnetic wave, and corresponds to the third term in Eq. (27). This type of wave is called anti-Stokes scattering. In Fig. 2.8, the red, orange, and blue waves depict Stokes-scattering, Rayleigh scattering, and anti-Stokes scattering, respectively.

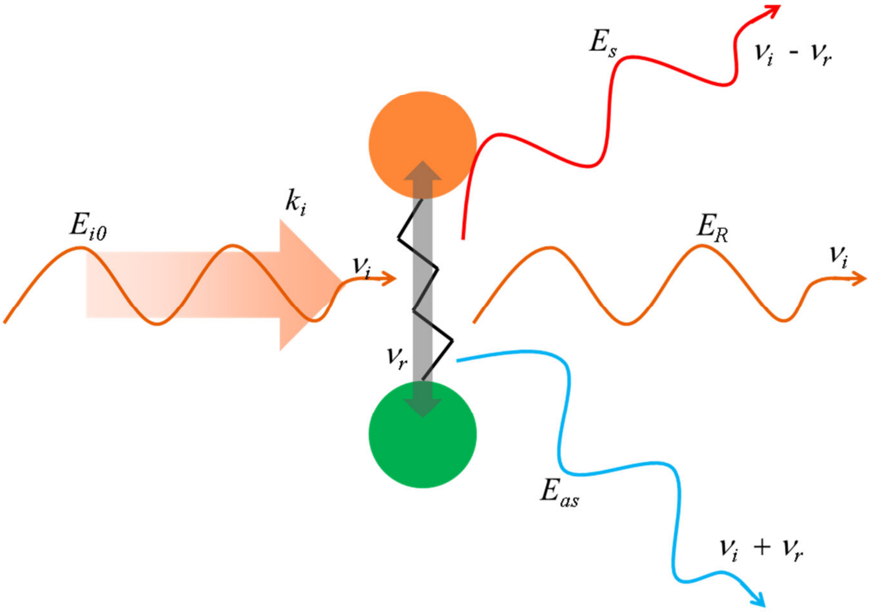

Fig.2.8. Schematic of the principle of Raman scattering

Here, the quantum theory of Raman scattering is explained briefly. The mechanism for Stokes scattering involves a photon from the probe light exciting an electron in the ground state to an intermediate state (Fig. 2.9(a)). The excited electron interacts with the phonon, and the energy of the electron is supplied to phonon, which induces a vibration. As the electron relaxes, the electromagnetic wave is radiated from the electron in the intermediate state. The energy of the electromagnetic wave is lower than the initial energy of the probe light because part of the excited electron’s energy is supplied to the phonon.

On the other hand, for anti-Stokes scattering, an electron in the ground state is excited to a vibrationally excited state by the interaction with a phonon (Fig. 2.9(b)). Then the electron in the vibrationally excited state is excited to the intermediate state by the photon of the probe light before the electron relaxes back to the ground state. The electron’s energy is released as an electromagnetic wave, which has a higher energy than the initial energy of the probe light because the electron begins at a higher energy, owing to a combination of the vibration and probe light energies. Consequently, the Stokes scattering peak is observed at a lower energy, while that of anti-Stokes scattering is observed at a higher energy in the spectrum.

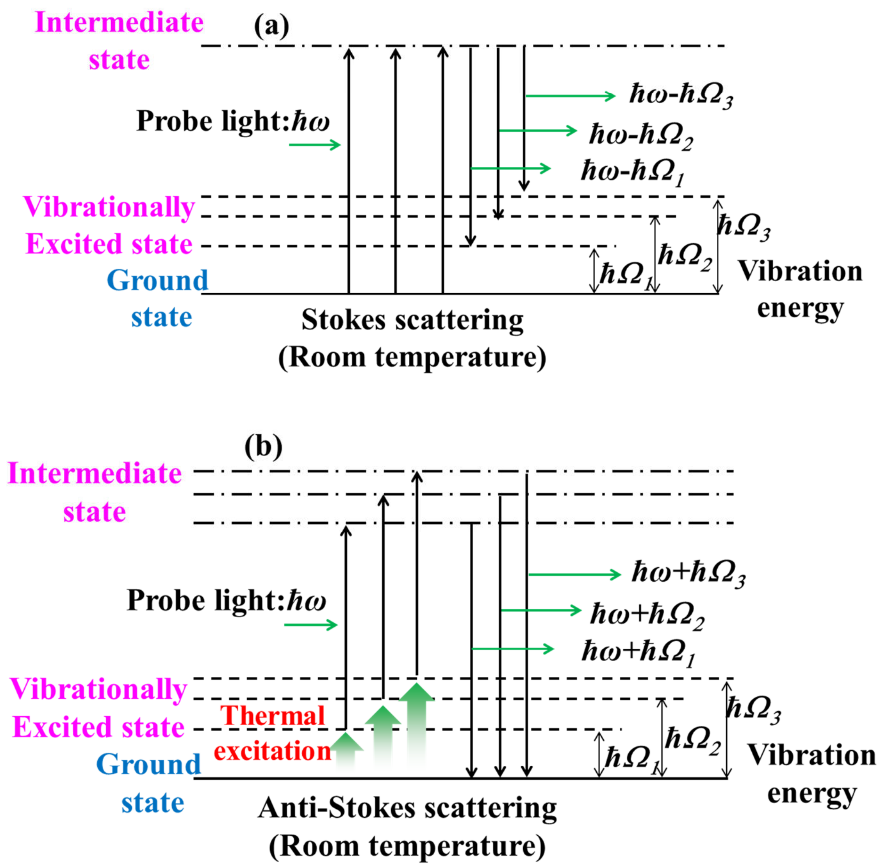

Fig. 2.9. Mechanism of Raman scattering: (a) Stokes scattering and (b) anti-Stokes scattering.

2-3-3-3 **Nonlinear Raman spectroscopy**

There are two types Raman scattering spectroscopies: linear and nonlinear. In linear Raman scattering, the intensity of the Raman scattering light is proportional to the intensity of the incident light. The Raman scattering described in Section 2-3-3-2 is linear Raman scattering (Fig. 2.10(a)). Nonlinear Raman scattering includes resonance Raman scattering, stimulated Raman scattering, etc.

Figure 2.10(b) schematically depicts the mechanism for non-linear resonance Raman scattering. When the energy of the probe light corresponds to the energy of the electron transition in a material, the intensity of the resonance Raman scattering is enhanced over 1000 times. Therefore, non-linear resonance Raman scattering is used to identify very low concentrations of liquids or small samples that cannot be measured using linear Raman scattering spectroscopy.

Figures 2.10 (c) and (d), schematically depict the mechanisms of stimulated Raman scattering. A sample is irradiated by two photons with different frequencies (ω_{i1} and ω_{i2}), where one photon frequency is fixed while the other is swept. When the difference between the two photons ($\omega_{i1} - \omega_{i2}$) is not coincident with the frequency of a molecular vibration or a phonon, the intensity of the two incident photons remains constant. However, if the difference between the two photons ($\omega_{i1} - \omega_{i2}$) is coincident with the frequency of a particular molecular vibration (v_r) or a particular phonon, the intensity of frequency-swept photon (ω_{i2}) is amplified, while that of the fixed frequency is decreased. Additionally, the phonon mode of the vibration frequency (v_r) is excited. Thus, the frequency of a molecular vibration of a phonon can be measured by observing the change in intensity of one of the radiating lasers. This phenomenon occurs without phase matching [41]. The principle of MSPE via coherent phonon generation was explained briefly in the Chapter 1. It is considered as a type of impulsive stimulated Raman scattering caused by the broad spectrum of an ultrafast laser. Details are provided in the next chapter.

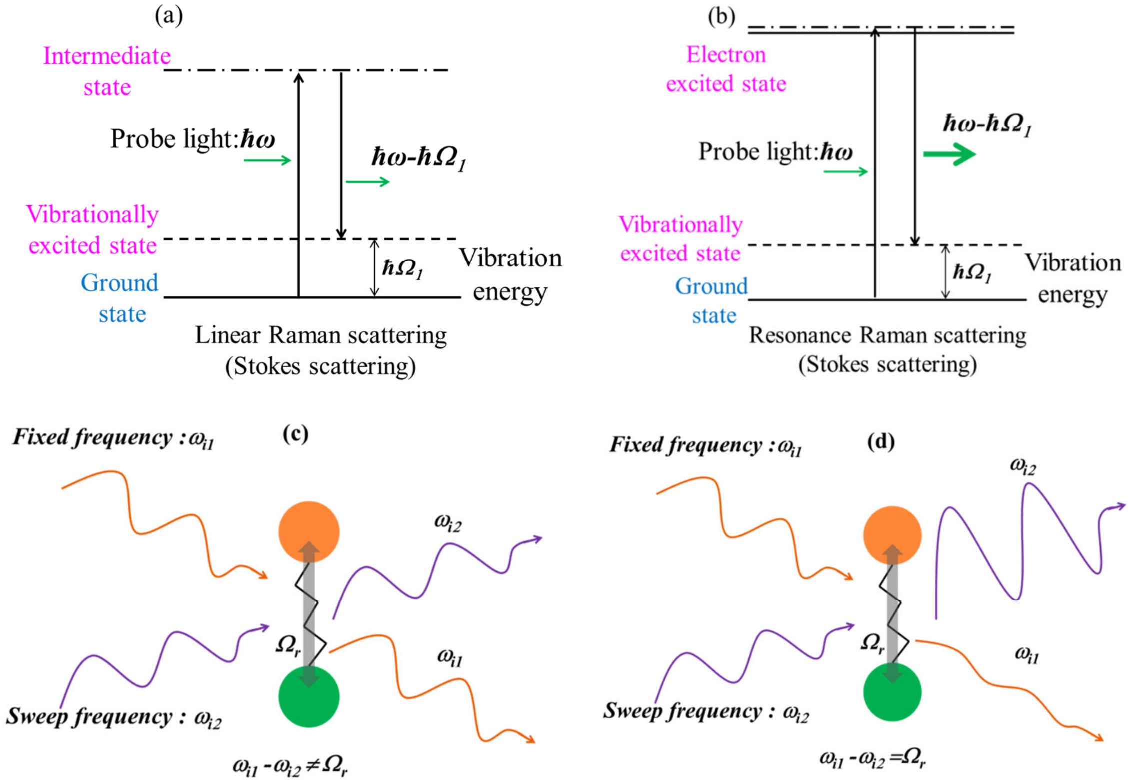

Fig. 2.10. Schematics of the three types of Raman scattering: (a) linear Raman scattering, (b) resonance Raman scattering, and (c) stimulated Raman scattering with $\omega_{i1} - \omega_{i2} \neq \Omega_r$, and (d) stimulated Raman scattering with $\omega_{i1} - \omega_{i2} = \Omega_r$.

2-4 **Method for mode-selective phonon excitation**

Two methods have been considered for MSPE: coherent phonons and irradiation by an MIR pulse laser. Both methods require an ultrafast pulse laser (femtosecond scale) to impulsively excite an electron to a vibrationally excited state and to prevent the effects of thermal excitation of a phonon. In this section, the two methods for MSPE, namely generation of coherent phonons and irradiation by an MIR pulse laser, are introduced.

2-4-1 **Generation of coherent phonons**

One method for MSPE is through a coherent phonon, which is generated by an ultrashort pulse laser with a pulse width less than a vibration period [11, 12]. MSPEs using coherent phonons have been reported in strongly-correlated electron systems, super-lattices, nanomaterials, semiconductors, *etc*.

Although the mechanism to generate coherent phonons has yet to be fully elucidated, several mechanisms have been proposed. Impulsive stimulated Raman scattering has been considered as a candidate to investigate transparent materials [19]. An overview of stimulated Raman scattering was shown in Section 2-3-3-3. A pulse laser with a pulse width shorter than the vibration period has a spectral width ($\Delta\nu$) similar to that shown in Fig. 2.11. If an electromagnetic wave whose spectral width is $\Delta\nu$ is coincident to the vibration frequency of a material ($\Delta\nu = \nu_r$, where ν_r is the vibration frequency of the material), the pulse laser will induce stimulated Raman scattering, and a particular phonon mode is excited. Owing to the uncertainty principle, the spectral width ($\Delta\nu$) depends on the pulse width (Δt) of the ultrafast laser. To excite a phonon mode with high energy, the spectral width must be widened. Therefore, a laser with a shorter pulse width is necessary to excite higher energy phonons. In addition, the optimum pulse width of the ultrafast pulse laser must be tuned to match the phonon energy and the energy of the pulse width of the laser for MSPE. If the spectrum width is too wide, then several phonon modes with energies less than the energy of the spectrum are excited.

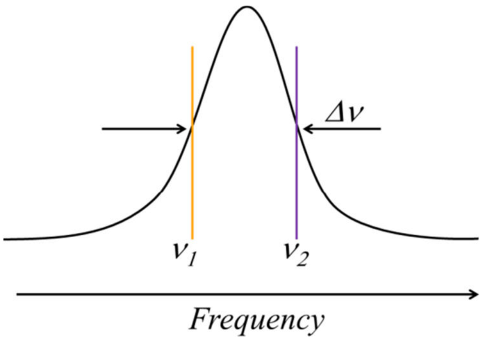

Fig. 2.11. Schematic of the spectrum of an ultrashort pulse laser

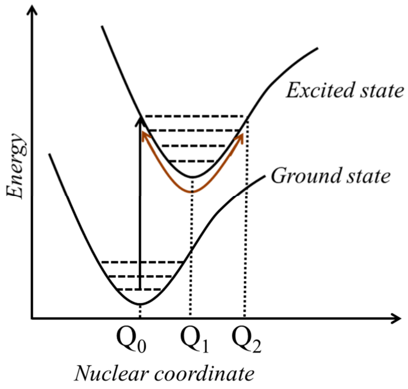

Fig. 2.12. Schematic of the principle of DECP

The other candidate to generate coherent phonons is the displacive excitation of coherent phonon (DECP) model [18] (Fig. 2.12). When an ultrafast pulse laser is radiated on to a material, an electron is excited. If the pulse width of the laser is shorter than the decay time of the phonon, then the change in the state of the atom conforms to the Franck–Condon principle. For example, prior to irradiation, an electron is in the ground state, which is marked as the equilibrium state (Q_0). After irradiation by an ultrashort pulse laser, the electron is excited, and the state changes to a non-equilibrium state. Consequently, the state changes from Q_0 to Q_1 to stabilize the nuclear state. However, owing to the energy conservation law, the state of the atom transits to Q_2. After this transition, the state of the atom transits continuously, as Q_2

→ Q_1 →Q_0 → Q_1→ Q_2 → Q_0 → … with decay. This phenomenon appears in the form of the vibration of the atom, which is phonon excitation.

In addition, MSPE caused by the interference of the coherent phonon has been reported [15] (Fig. 2.13). It is hypothesized that the non-mode-selective phonon excitation occurs and two phonon modes are excited by coherent phonon generation (CPG) (Fig. 2.13 (a)). Additionally, the red and blue arrows denote T_a and T_b, respectively, which are periods of the phonon mode such that $T_a \neq T_b$. When irradiated by an ultrashort pulse laser at a repetition rate with a much longer period than the period of the vibration of a phonon, two phonon modes are excited. If the period of the repetition rate of the ultrashort pulse laser (T) is coincident with the period of the phonon mode ($T = T_a$), then oscillation of the atom is amplified by the interference of the atom oscillations induced by two laser pulses (Fig. 2.13 (b)). This means that the phonon mode indicated by the red arrows is excited. In addition, if the period of the repetition rate of the ultrashort pulse laser (T) is coincident with 1.5-times the period of the phonon mode ($T = 1.5T_a$), then atom oscillation is cancelled as a result of interference (Fig. 2.13 (c)). Moreover, the third pulse of the ultrashort pulse laser excites the phonon mode (large red arrow), but the excited phonon mode will be cancelled by the fourth pulse. In this way, when T is $1.5T_a$, the excitation and cancellation cycle is repeated. Hase *et al.* have controlled MSPE and the relaxation of a particular phonon mode by adjusting the repetition rate of the laser [15].

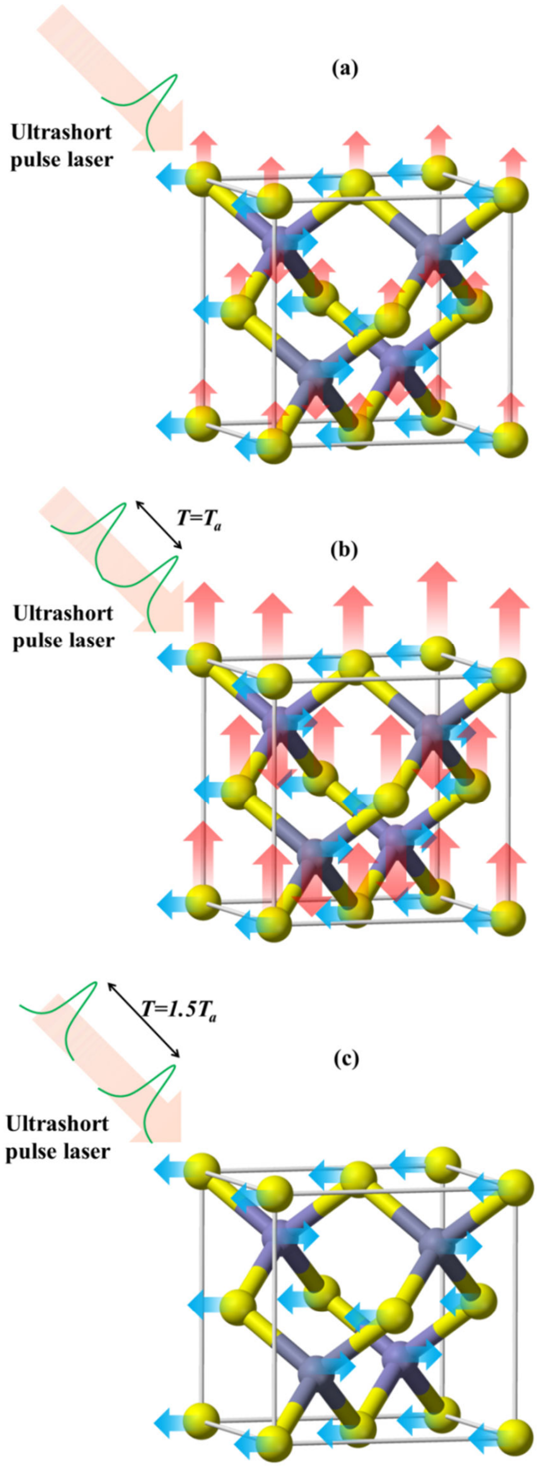

Fig. 2.13. Schematic of the mechanism of MSPE caused by interference of CPG with (a) a single pulse (b) a multi-pulse whose pulse period is T_a, and (c) a multi-pulse whose pulse period is $1.5T_a$.

2-4-2 **Irradiation by a mid-infrared pulse laser**

Another mechanism for MSPE is irradiation by an MIR pulse laser. The principle of this mechanism is direct excitation by the interaction between the electromagnetic wave and the dipole induced by two atoms as shown in Fig. 2.14. In this method, it is important to match the laser wavelength to the absorption wavelength of the phonon. Only the optical phonon mode is excited by the MIR pulse laser because the phonon mode of the acoustic mode does not induce a change in the dipole moment. Moreover, to prevent thermal excitation of the phonons by laser irradiation, the pulse width of the MIR pulse laser must be shorter than the phonon decay time for MSPE. One advantage of this method is that by using a tunable MIR pulse laser, the phonon mode can be selectively excited even if the phonon mode has a high energy.

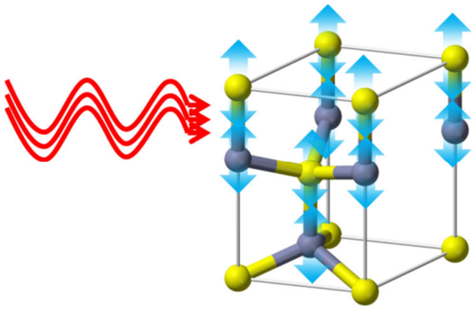

Fig. 2.14. Schematic of the interaction between an electromagnetic wave and a material and the oscillation of two atoms

2-5 **Light source for MSPE by an MIR pulse laser**

There are many potential light sources for the MIR region: a quantum cascade lasers (QCL), difference frequency generation (DFG), an optical parametric oscillator (OPO), a CO_2 laser, an optical parametric amplifier (OPA), *etc.* QCL can generate MIR light from 3 μm to 25 μm [42], and this technology is continuing to advance.

The shortest pulse width generated by pulsed QCL is around 3 ps with 0.5 pJ at 6.2 μm [23]. Because the phonon decay time of the optical mode is around 3 ps in the case of the semiconductor at room temperature [32, 43, 44,], the pulse width of the QCL is insufficient for MSPE. However, as the technology improves, QCL should satisfy the conditions for MSPE.

As candidate light sources for the MSPE, DFG, OPO, and OPA were also considered in a solid-state laser. These light sources can tune the wavelength by exchanging the crystals used as nonlinear optical material (NOM) and adjusting the angle of the NOM. Figure 2.15 summarizes NOMs with reported tunable wavelengths and pulse properties [45-50]. Nonlinear optics technologies such as optical parametric generation, OPO, and DFG can generate an ultrashort pulse, which is shorter than the phonon decay time with MIR light. Therefore, these lasers should be applicable as a light source for MSPE.

An MIR femtosecond laser with a tunable wavelength from 5 to 20 μm (a conventional MIR laser) is available commercially (*e.g.,* OPerA^{TM} Solo, Coherent Inc.). The reported peak power, average power, and repetition rate of the conventional MIR laser (OPerA^{TM}, Coherent Inc.) are 8 MW, 2 mJ, and 1 kHz at 12 μm. The pulse width is around 200 fs. Figure 2.16 shows an example of the pulse structure of the conventional MIR laser. In addition, an MIR-FEL (KU-FEL) is a potential light source for MSPE. Figure 2.16 (b) shows the pulse structure of MIR-FEL (KU-FEL). The KU-FEL has specific pulse structures called macro-pulses and micro-pulses. The macro-pulse width is 2 μs, and the micro-pulse width is 600 fs [51]. A macro-pulse consists of around 5700 pulses, where a micro-pulse is repeated every 350 ps. The peak power and average power are 5 MW and 17 mW, respectively, at 12 μm with a repetition rate of 1 Hz. As mentioned in Section 1-2, the KU-FEL has advantages for MSPE, namely high power, short pulse width and wavelength tunability. Therefore, the KU-FEL was selected as the light source for MSPE.

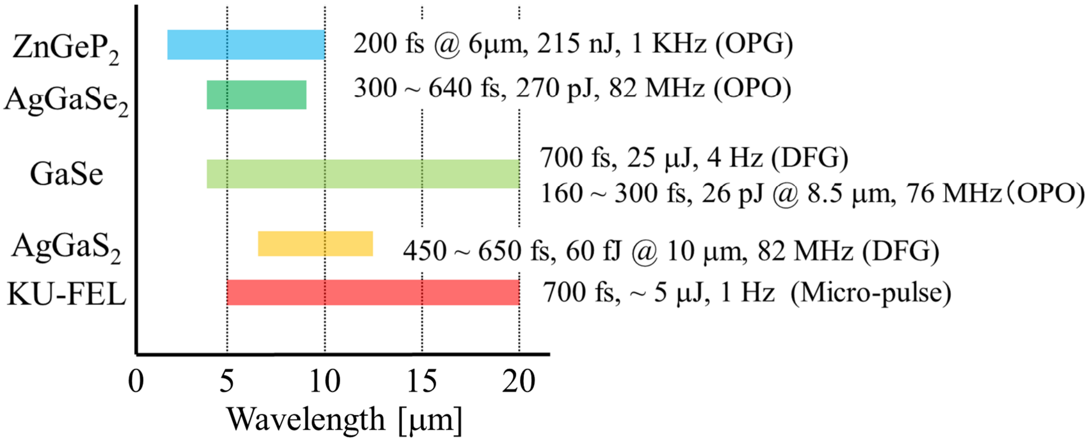

Fig. 2.15. Chart of the NOMs and reported tunable wavelengths of an MIR pulse laser generated by DFG or OPO, and the tunable wavelength of KU-FEL. Labels on the right indicate the properties of the lasers. : $ZnGeP_2$ [45, 46], $AgGaSe_2$ [45, 47], GaSe [45, 48, 49], and $AgGaS_2$ [45, 50]

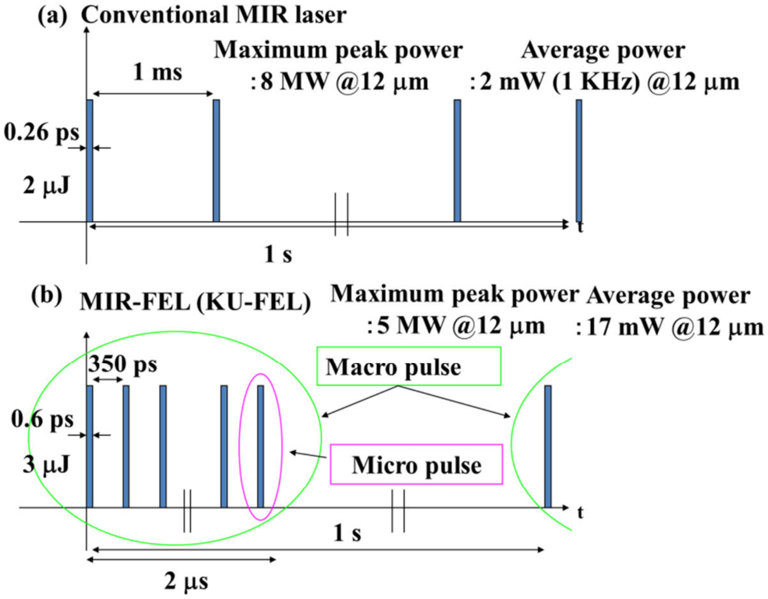

Fig. 2.16. Schematic of the pulse structure of (a) a conventional MIR laser [52] and (b) the KU-FEL

2-6 **Conclusion**

In this chapter, phonon and vibrational spectroscopies were described. In addition, methods for MSPE were introduced. One method that generates coherent phonons by an ultrashort pulse laser, can be used for the MSPE of a phonon in the terahertz region. The other method uses an MIR pulse laser to excite the phonon mode even if the phonon mode has a high energy. However, only the optical phonon mode can be excited because the acoustic mode cannot induce a change in the dipole moment.

OPO, optical parametric generation, and DFG were considered as light sources for MSPE by an MIR laser. However, the MIR free electron laser is the most suitable because it has the advantages of high power, short pulse, and wavelength tunability.

3 FEL facility

Because there are only a few free electron laser (FEL) facilities around the world, many researchers are still unfamiliar with FELs. Hence, this chapter describes FELs. Section 3-1 describes the principle of the FEL. Section 3-2 describes the types of FEL facilities and their applications. Section 3-3 describes the Kyoto University free Electron Laser (KU-FEL). Sections 3-4 and 3-5 discuss the performance and scientific applications of the KU-FEL.

3-1 **Principles of FELs**

There are two types of FEL: The oscillator type and the self-amplified spontaneous emission（SASE）type. Because the KU-FEL is FEL of the oscillator type, the principle of oscillator-type FEL is explained in this section. The FEL beam is generated by the interaction between an electron beam and synchrotron radiation (SR). Figure 3.1 shows the principles of the oscillator-type FEL. The electron beam is generated by an electron gun, in which a cathode (*e.g.*, a thermionic cathode or photocathode) is used. A thermionic cathode generates electrons upon heating, whereas a photocathode generates electrons via a photo-electron effect with a strong laser. Details of the electron gun are described elsewhere [53]. The generated electrons are bunched by electromagnets or radio frequency (RF), accelerated to almost the speed of light, and then injected into an undulator which is installed with two mirrors. One of the mirrors has an out-coupling hole to extract amplified light. The undulator has a pair of magnet arrays, which are periodically arranged with an alternating magnetic field, so that the electrons perform a “wiggling” motion in the undulator. The wiggled electrons generate the SR (Fig. 3.1 (a)), which is stored in the optical cavity. The stored SR interacts with successive electrons. The electrons gain and lose energy upon interaction with the SR. Thus, the interaction with SR introduces energy modulation, which induces a micro-structure in the electron beam called a microbunch (Fig. 3.1 (b)). This microbunching process continues until the electrons are completely microbunched (Fig. 3.1(c)), and the completely microbunched electrons generate SR with the same phase, owing to the wiggling motion during the undulator. SR is amplified by the overlap with SR generated by each microbunch, and the SR produces coherent light with a high power, which is called a free electron laser (FEL).

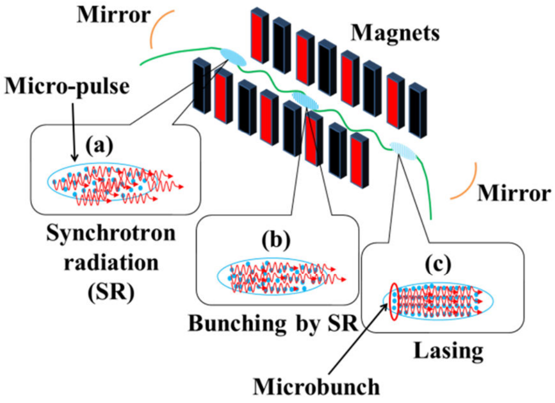

Fig. 3.1. Principle of an oscillator-type FEL.

The central wavelength (λ_R) of the FEL is shown in the following equation [53]:

$$\lambda_R = \frac{\lambda_u\left(1+\frac{K^2}{2}\right)}{2\gamma^2}, \tag{28}$$

where λ_u is the period of the undulator field, $\gamma=(1-v^2/c^2)^{-1/2}$ is called the Lorentz factor, and v and c are the speeds of an electron and of light, respectively.

Meanwhile, K is the dimensionless, undulator parameter, which is defined as:

$$K = \frac{eB_0\lambda_u}{2\pi mc}, \tag{29}$$

where e, m, and B_0 are the elementary charge, electron mass, and peak intensity of the magnetic field in the undulator, respectively. Equation (29) can be converted into [53]:

$$K = 93.4B_0\lambda_u, \tag{30}$$

where the units of B_0 and λ_u are T and m, respectively.

The center wavelength of FEL depends on the undulator parameters (B_0 and λ_u), and electron energy (γ). Because B_0 depends on the gap of the undulator, the wavelength can be quickly changed by adjusting the gap of the undulator.

The pulse structure of the FEL differs from that of conventional lasers. The FEL beam produces two types of pulse structures: micro-pulses and macro-pulses. The relationship between these structures is depicted in Fig. 3.2. A macro-pulse is an aggregate of micro-pulses. The parameters of the pulse widths for both micro- and macro-pulses depend on the parameters of the electron beam.

Figure 3.3 details the electron beam in the optical cavity. The electron beam has electron bunches when viewed microscopically. The pulse width of a micro-pulse in the FEL beam depends on the width of the electron bunch; a short electron bunch in the optical cavity introduces a micro-pulse with a short width in the FEL beam.

A macro-pulse in the FEL beam depends on the condition of the electron beam in the optical cavity and the FEL gain. As shown in Fig. 3.3, the micro-pulse duration depends on the frequency of the microwave used for the electron acceleration. In the case of the KU-FEL, the RF for electron acceleration is 2856 MHz, which consequently produces micro-pulses with durations of 350 ps.

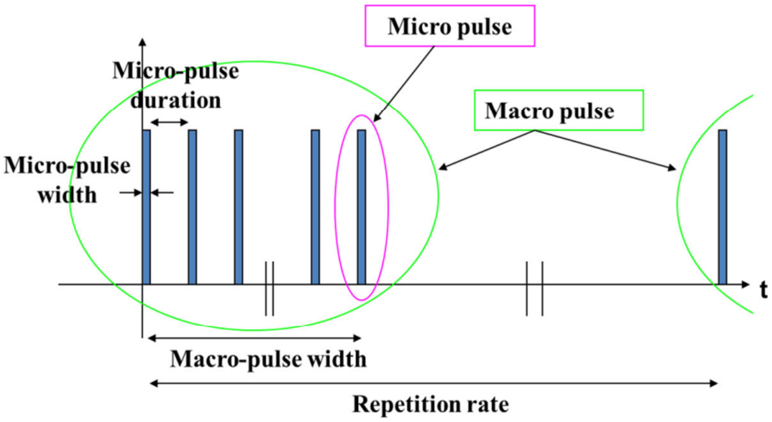

Fig. 3.2. Relationship between micro- and macro-pulses in the FEL beam.

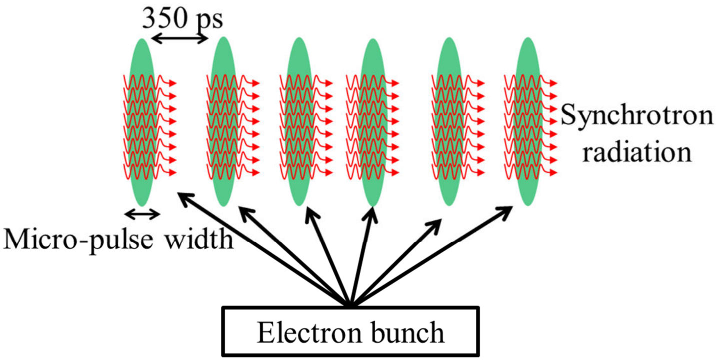

Fig. 3.3. Schematic of the electron beam in the optical cavity.

3-2 **Facilities and applications**

3-2-1 **Facilities around the world**

FEL facilities are classified according to their accelerator type, as RF-linac-based FEL facilities, storage-ring-based FEL facilities, energy recovery linac (ERL)-based FEL facilities, and electrostatic accelerated FEL facilities. In this section, each type of facility is briefly discussed from the viewpoint of FEL applications.

(1) RF-linac-based FEL facility

RF-linac-based FEL facilities, which are the most common type, can cover FEL wavelengths from the THz region to the X-ray region [54]. There are two types of RF-linac-based FEL: the oscillator type (Fig. 3.4) and the SASE type. The details of the mechanism of the SASE type FEL are shown elsewhere [55]. The generated light in these facilities have the characteristics of short pulses and high power [53], generating a FEL with a peak power on the order of megawatts. The oscillator type can be used for light emissions from the infrared to the ultraviolet regions. Two mirrors are used to store SR. Because high-reflectivity mirrors are not available for the extreme ultraviolet (EUV) to X-ray regions, the SASE type is used for FELs in these regions. The KU-FEL is an oscillator-type RF-linac-based FEL facility as explained in Section 3-1. In 2011, the SACLA at SPring-8 achieved lasing with an X-ray FEL (XFEL) [56].

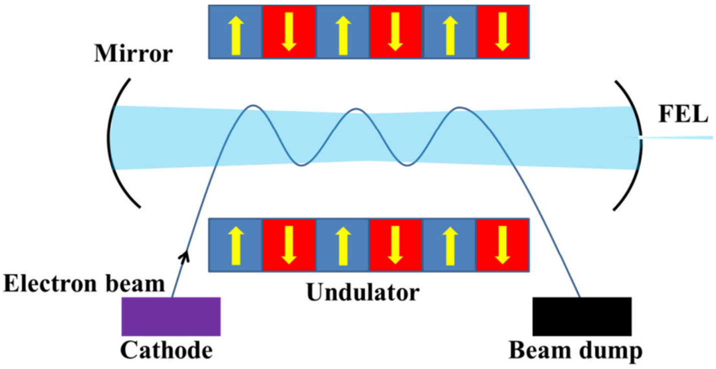

Fig.3.4. Principle of the oscillator-type FEL.

(2) Storage-ring-based FEL facility

Storage-ring-based FEL facilities are used to generate light in the UV to visible regions. Figure 3.5 shows the principle of the storage-ring type FEL. An electron injector injects electrons into the storage ring, where they are stored. In this type, an electron bunch from the storage ring arrives continuously at the undulator. Therefore, the pulse structure of the emitted FEL is a continuous wave of micro-pulses. The peak power is rather low [53]. However, the spectrum width of the FEL is narrow, and the wavelength stability is high [53, 57]. Additionally, because synchronization between SR and the FEL beam is easy, pump–probe experiments can be conducted using the storage ring type FEL. Examples of a storage-ring-based FEL facility are UVSOR-II at the Institute for Molecular Science [58] and DFELL at Duke University [58, 59].

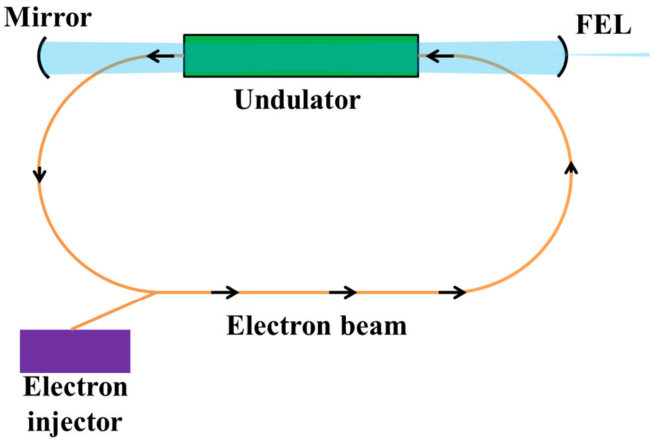

Fig. 3.5. Principle of the storage-ring-based FEL.

(3) ERL-based FEL facility

The ERL-based FEL has been developed as a next-generation FEL technology (Fig. 3.6). The electron beam is injected into a ring with an accelerator tube. The electron is then dumped after circulating once in the ERL. Before dumping the electron, the electron is decelerated and the energy of the electron is collected. The collected energy is then used to accelerate an injected electron. Therefore, the ERL can operate continuously and this system is called the "energy recovery linac". The characteristics of the ERL-based FEL are high peak power on the order of gigawatts, short pulses and a continuous wave [60, 61], which are advantages of both RF-linac-based FEL and the storage-ring-based FEL.

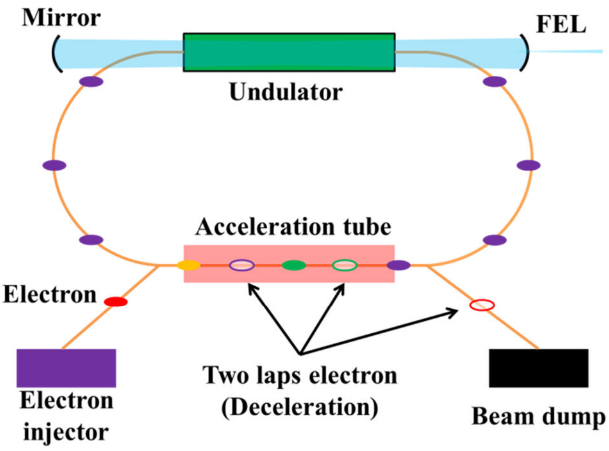

Fig. 3.6. The principle of the ERL based FEL

(4) Electrostatic FEL facility

The electrostatic FEL facility is the simplest type of FEL facility. Examples of this type of facility are located at the Center for Terahertz Science and Technology at University of California in Santa Barbara (UCSB), Tel Aviv University in Israel, *etc*. [53, 62]. Figure 3.7 shows the principle of the electrostatic FEL facility. The generated electron is accelerated continuously by the electric field in an acceleration tube. Thus, the generated FEL beam has the characteristics of a continuous wave or a quasi-continuous wave (long pulse) with high spectral purity [62, 63]. In addition, it has a wide tunable wavelength, from 63 µm to 2500 µm [63]. The efficiency of the energy conversion is high because the energy of the used electron beam is collected and re-used for electron acceleration [64]. However, it is difficult to generate an FEL beam with a wavelength less than 10 µm because the maximum energy of the accelerated electron is less than 10 MeV [64].

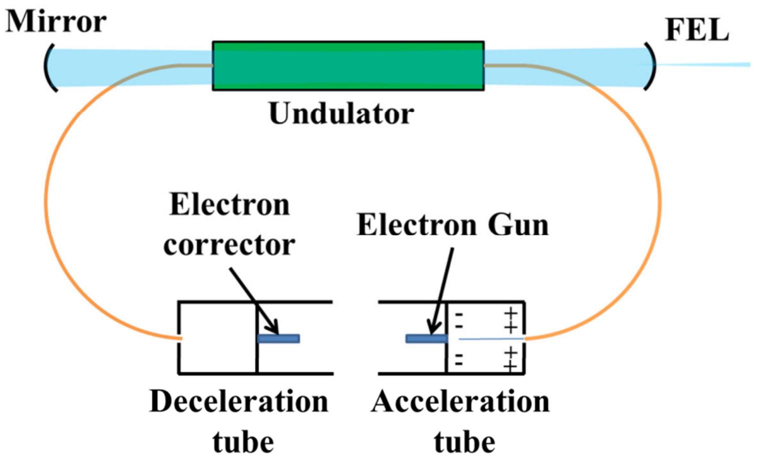

Fig. 3.7. Principle of the electrostatic FEL facility.

3-2-2 **FEL applications**

Many applications have been realized thanks to the tunability of the wavelength and the generation of high-power light by an FEL. An FEL beam generated in the MIR region or in the terahertz region is used for solid-state physics (e.g. condensed-matter and quantum dots) [65] because the light of the terahertz to MIR regions corresponds to the absorption wavelength of phonons, plasmons, *etc*. Additionally, the pulse width of the laser is sufficiently short to observe ultrafast dynamics. Therefore, terahertz to MIR FELs are useful for investigating the dynamics of energy redistribution of phonons, *etc.* [65]. Similarly, because the excitation energy of quantum dots is also in the terahertz to MIR regions, this type of FEL can excite electrons in quantum dots; the dynamics of electron relaxation in quantum dots have been investigated using a pump–probe experiment using an FEL [65]. Moreover, terahertz to MIR region FELs have been applied to non-linear optics, spin dynamics, impurity studies in semiconductors, *etc*. [65].

The MIR-FEL has been used in the fields of chemistry and biology. Because the

MIR region corresponds to the absorption wavelength of phonons as well as the absorption wavelength of molecular vibration, it can be used to selectively dissociate or excite chemical bonds [66, 67]. As an example of mode-selective dissociation, the mass spectra of chemicals such as amino-acids have been acquired using infrared multiphoton dissociation by the MIR-FEL at FOM FELIX in the Netherlands [68, 69].

The XFEL is superior for structural analysis. Conventional X-ray sources cannot observe the signal from a small crystal (*e.g.*, a nano-crystal). Therefore, bulk-size crystallization is essential to measure the X-ray diffraction pattern, which makes it extremely hard to analyze the structure of massive molecules (*e.g.*, proteins) owing to difficulties with crystallization. Unlike conventional X-rays, an XFEL can analyze the crystal structure of nanosized proteins [55, 70]. Therefore, special techniques are not required to prepare bulk single crystals. Additionally, it is expected that an XFEL will observe atomic motions in real time [55].

Some lasers can produce high-power visible light, (*e.g.*, the Ti-sapphire laser, the Nd-YAG laser, *etc.*) using nonlinear optical materials. Therefore, visible-light FELs are inferior to MIR-FELs, THz-FELs, and XFELs as high-power light sources. However, the visible-light FEL beam is generated by a storage ring and therefore the FEL and synchrotron emissions can be synchronized easily, which is advantageous in pump-probe experiments [71].

A summary of the typical application fields of FELs of each wavelength region is shown in Table 3.1.

Table 3.1. Summary of typical application fields of FELs of each wavelength region.

Wavelength region	Application fields	Examples
THz-FEL	Solid-state-physics	Interband dynamics in semiconductors and quantum dots [65] Non-linear optics [65] Spin dynamics [65] Vibration spectroscopy [65]
MIR-FEL	Solid-state-physics	Dynamics of phonons in solid materials [65]
	Chemistry	Dissociation of Freon [72]
		Chemical analysis [68]
		Thin-film fabrication [73]
	Dentistry	Surface modification of a tooth [74]
	Medicine	Selective removal of harmful substances in a human body [75]
Near infrared-visible-FEL	Chemistry	Time-resolved polarized fluorescence spectroscopy with SR [65]
X-FEL	Biochemistry	Construction analysis of proteins [70]
	Physics	Investigation of hollow atoms [55]
		X-ray photoelectron spectroscopy [55]
	Chemistry	Real-time observation of atomic motion [55]

3-3 **Overview of the KU-FEL**

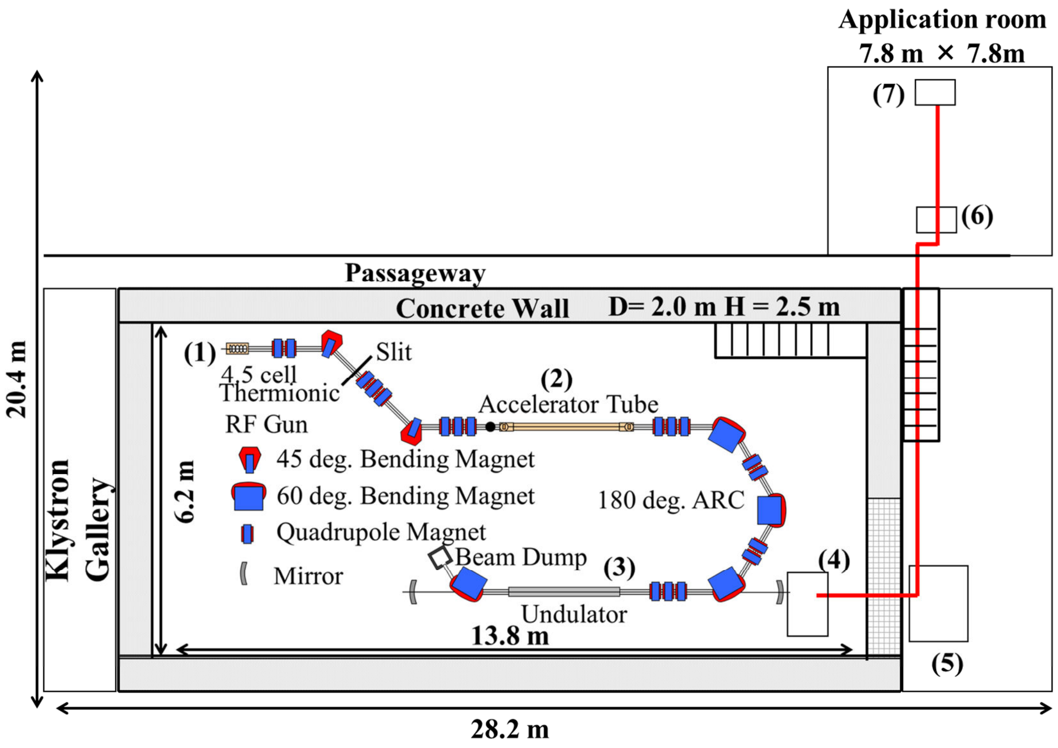

Fig. 3.8. Schematic of the KU-FEL facility.

The KU-FEL facility consists of seven components (Fig. 3.8): (1) the electron gun, (2) the accelerator tube, (3) the optical cavity, (4) the FEL quasi-parallel beam system, and (5) - (7) the three user stations. Each component is briefly described below.

(1) Electron gun

The electron gun is an essential component for generating the FEL beam. The KU-FEL uses a thermionic RF gun. The electron beam is generated by heating a cathode; in the KU-FEL, a LaB_6 cathode is heated to 1600 ˚C. After the electron beam is generated, it is accelerated at a frequency of 2856 MHz by a microwave in the electron gun, achieving an electron energy of around 8 MeV. This configuration can generate a high-energy electron beam using simple equipment, which helps realize a compact FEL facility. However, the thermionic RF gun has a serious problem in FEL operation: some components of the electron beam in the thermionic RF electron gun are accelerated backward by the effect of the RF phase. This introduces instability because electron generation at the cathode becomes unstable owing to heating of the cathode surface by the backward electrons. We solved this issue at the KU-FEL facility by precisely controlling the RF power feed into the electron gun and the RF phase [76]. Figure 3.9 shows a photograph of the thermionic RF gun used in the KU-FEL.

Fig. 3.9. Photograph of the thermionic RF gun used in the KU-FEL.

(2) Accelerator tube

The wavelength of the FEL depends on the electron beam energy and the undulator parameters. Using the thermionic RF gun, the electron beam is accelerated up to 8 MeV. However, 8 MeV is not sufficient for FEL oscillation in the MIR region in the KU-FEL. Therefore, an accelerator tube is used in the KU-FEL to increase the electron beam energy. The KU-FEL uses a 3-m-long accelerator tube. There are two types of accelerator tubes: a constant impedance (CI) type and constant gradient (CG) type [77]. The accelerator tube contains a large number of acceleration cells to accelerate the electron. In the CI type, the structure of acceleration cells is the same in all cells. However, in the CG types, the structure of the acceleration cells differs in each cell to ensure a constant acceleration electric field in all cells. The CG type has higher energy conversion efficiency than the CI type. The KU-FEL uses the CG-type accelerator tube. The RF used for acceleration in the KU-FEL is in the S-band, with 2856 MHz. The electron beam can be accelerated up to around 40 MeV. Figure 3.10 shows a photograph of the accelerator tube.

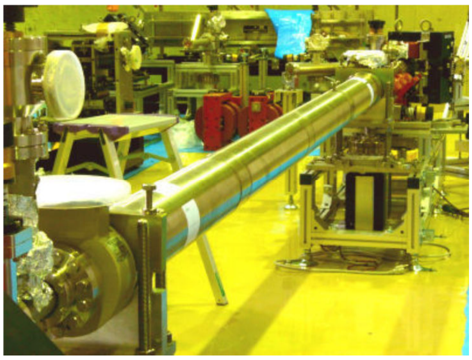

Fig. 3.10. The photograph of the accelerator tube used in the KU-FEL.

(3) Optical cavity

Figure 3.11 shows the optical cavity in the KU-FEL. A confocal Fabry–Perot (FP) resonator is used. The curvatures of the two mirrors, located the downstream and upstream, are 2.456 m and 2.946 m, respectively. These values were determined to yield the maximum saturated power in the optical cavity [78].

The cavity length is to be designed 5.0385 m as using an optical cavity of this length enables 96 micro-pulses to be stored, because the frequency of the micro-pulse train is 2856 MHz. The installation of a photocathode system for electron beam generation is planned for future work, in order to enhance the peak power. Because a Nd-YVO_4 laser with a repetition rate of 89.25 MHz is radiated onto Cs_2Te for photoelectron generation, the frequency of the generated micro-pulse train is 89.25 MHz. This is the 32nd sub-harmonic frequency of the accelerator's RF (2856 MHz). Therefore, three micro-pulses can be stored in an optical cavity 5.0385 m long when the photocathode is used. Consequently, an optical cavity 5.0385 m long can store FEL micro-pulse trains whose frequencies are both 2856 MHz and 89.25 MHz. The upstream mirror has an out-coupling hole with 1 mm hole to extract part of the FEL beam stored in the optical cavity.

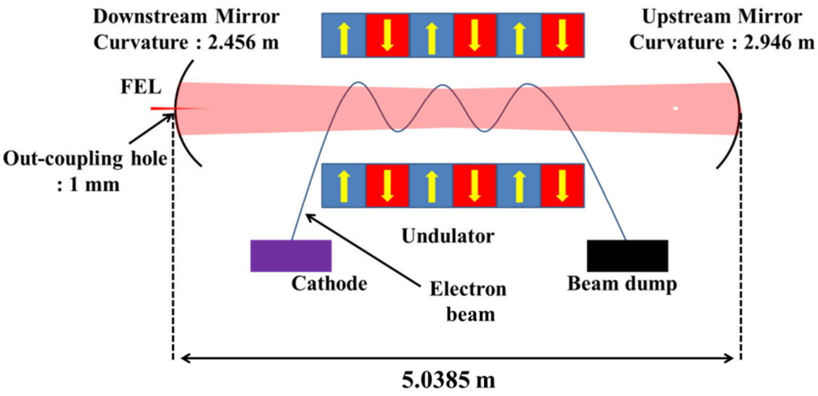

Fig. 3.11. Schematic of the optical cavity used in the KU-FEL

The parameters of the undulator are an important factor in generating the FEL beam and controlling its wavelength. Table 3.2 lists the parameters of the undulator used in the KU-FEL. The K-value is changed by adjusting the gap of the undulator to vary the wavelength. Figure 3.12 shows a photograph of the undulator used in the KU-FEL.

Table 3.2. Parameters of the undulator used in the KU-FEL.

Period length (λ_u)	33 mm
Maximum K-value	1.56 @ 15-mm gap
Minimum gap	15 mm

Fig. 3.12. Photograph of the undulator used in the KU-FEL.

(4) FEL quasi-parallel beam system

In this section of the KU-FEL, the FEL beam is composed of a quasi-parallel beam for efficient beam transportation to user stations. In addition, a mercury cadmium zinc telleride (MCZT) detector (Vigo System, PDI-2TE-10.6) is used to detect the power evolution of the FEL. Details of the FEL quasi-parallel beam system are presented in Chapter 4.

(5)–(7) User stations

Three user stations are installed in the KU-FEL. User station 5 is for simple irradiation experiments (*e.g.*, ablation and thin film fabrication). User station 6 contains a photoluminescence spectrometer and a Raman scattering spectrometer, which can be used to investigate the physical properties of materials (e.g., electronic or vibrational states). In addition, user station 6 has a closed-cycle helium refrigerator. The refrigerator can cool materials down to 14 K. Figure 3.13 is a photograph of user station 6. User station 7 is used to investigate the optical properties of the FEL beam.

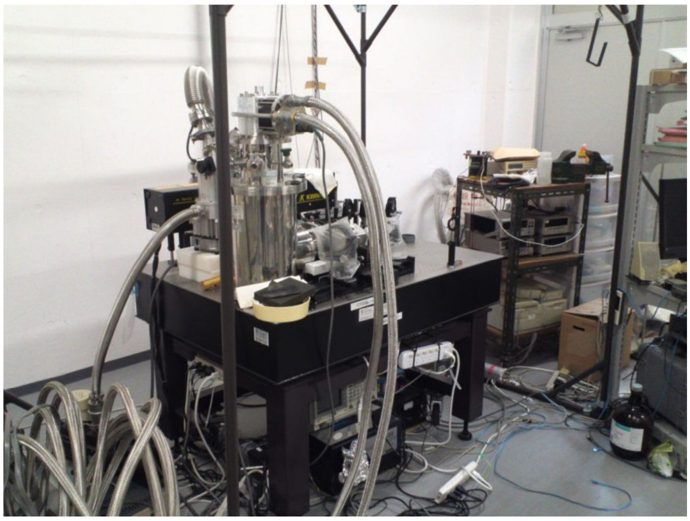

Fig. 3.13. Photograph of user station 6

3-4 **KU-FEL performance**

The parameters of the KU-FEL are described briefly. Table 3.3 lists the specifications of the KU-FEL[79]. The maximum peak power is around 8 MW at 8 μm. The polarization of the FEL is vertical at user stations 6 and 7 (Fig. 3.14). In practice, however, the polarization at user station 6 has a tilt angle of 4° off vertical. Figure 3.15 shows the tunable wavelength and pulse energy for each wavelength.

Table 3.3.Specifications of the KU-FEL.

Wavelength tunable range (> 1mJ)	5 – 22 μm
Maximum pulse energy	30 mJ @ 8μm
Maximum peak power	8 MW @ 8 μm
Spectrum width	~ 3 %
Macro-pulse duration (FWHM)	~ 2 μs
Micro-pulse width (FWHM) [51]	< 0.6 ps @ 12 μm
Wavelength stability (FWHM) [51]	< 1.3% @ 12 μm
Repetition rate of micro-pulse	2856 MHz

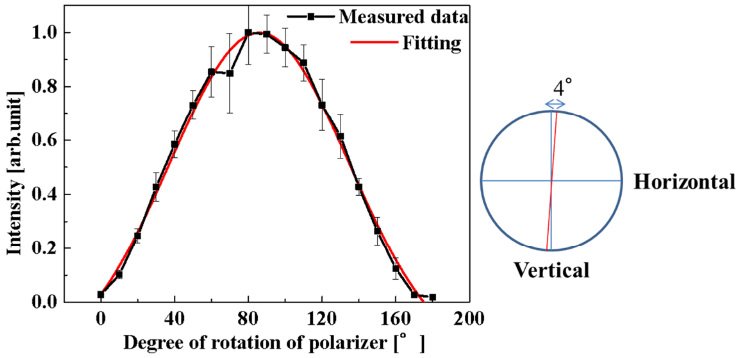

Fig. 3.14. Polarization of the FEL beam at user station 6.

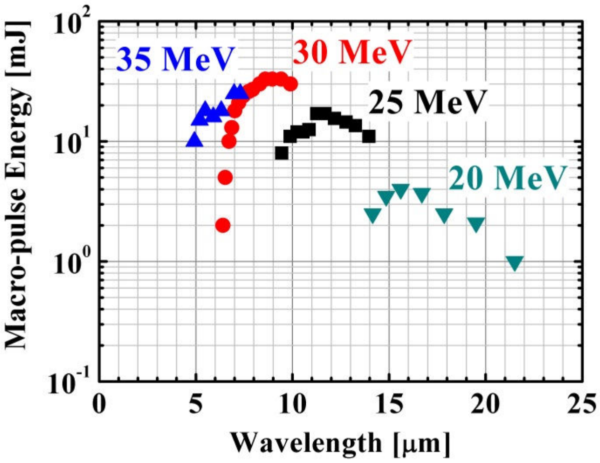

Fig. 3.15. Tunable wavelength and pulse energy of each wavelength.

The energy is the electron beam energy [80].

3-5 **Practical research with the KU-FEL**

A photoluminescence spectrometer was installed in the KU-FEL for development of energy science. The photoluminescence spectrometer is connected to the FEL beam transportation line. Therefore, the following applications can be employed to investigate electronic structures in solid materials via a photoluminescence spectrometer with an MIR-FEL.

Light from the MIR region resonates with phonons in solid materials [81, 82]. Due to the features of the FEL (*i.e.*, high power and short pulse), the radiation of the MIR-FEL will cause changes in the physical and electronic properties by exciting a specific phonon mode. In addition, a photoluminescence (PL) spectrometer can be used to analyze the electronic structure of the solid. Consequently, combining the MIR-FEL and the photoluminescence spectrometer allows the relationship between a particular phonon and the electronic structure of a solid material to be investigated.

Figure 3.16 schematically depicts the PL system with an MIR-FEL. The PL system consists of a He-Cd laser (wavelength: 325 nm, power: 10 mW, beam diameter: 1.0 mm; Kimmon, IK5451R-E), a monochromator (Zolix, Omni-λ300), and a charge-coupled device (CCD) detector (Intevac, Mosir 350). The closed-cycle helium refrigerator allows the temperature dependence of the PL spectrum to be evaluated down to 10 K. For synchronized radiation of the MIR-FEL and the He-Cd laser, an accelerator trigger is used as the trigger of the PL measurement system. In the PL analysis section, a CCD detector is used to receive the material response, and a PC collects data from the CCD detector.

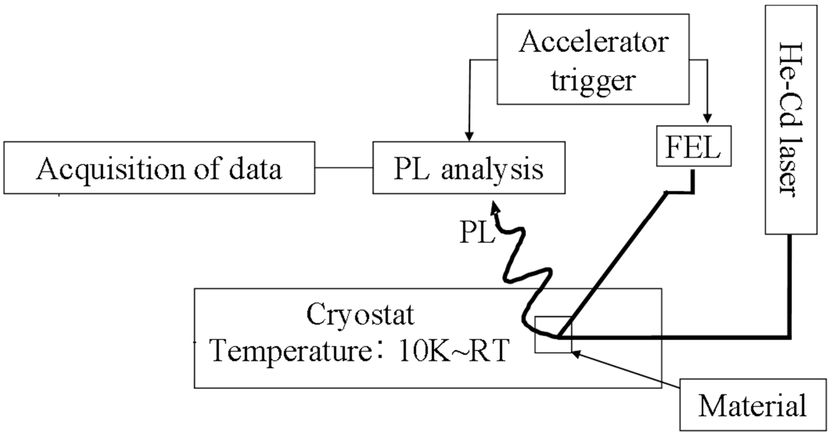

Fig. 3.16 Schematic of PL system with MIR-FEL

4 Construction and evaluation of the FEL beam transport system in the KU-FEL

To investigate mode-selective phonon excitations (MSPE) using the mid-infrared (MIR)- free electron laser (FEL), the FEL beam had to be transported to the user station. The design concept of the transport system is shown in Section 4-1. Section 4-2 describes the design calculations of the transport system. Section 4-3 evaluates the beam size at the user stations. Section 4-4 describes the transportation ratio of the FEL beam to the user stations. Section 4-5 discusses the effectiveness of nitrogen filling to prevent air absorption of the MIR-FEL beams, while Section 4-6 determines the existence of high harmonics in the FEL beam by measuring the spectrum in the visible light region.

4-1 **Objective**

The FEL is a laser amplified by a high-energy electron beam. However, the high-energy electron beam also generates undesired form of radiation (*e.g.*, X-rays, γ-rays, and neutrons) when a high-energy electron collides with components in the FEL facility (*e.g.*, a vacuum duct). Therefore, the FEL emission point cannot be freely accessed during FEL lasing. In general, the FEL beam must be transported from the out-coupling hole to a user station for practical use. The beam transport system developed for an MIR-FEL at the Science University of Tokyo uses elliptical and parabolic mirrors [83]. This beam transport system can transport an FEL beam at any wavelength without aberrations in the parallel direction, but the system is very expensive and is difficult to align. In other facilities such as FOM-FELIX in the

Netherlands and FELI in Japan, a spherical mirror is used to form the beam into a quasi-parallel beam system; the mirror is low cost and easier to align but can cause aberrations in the transported FEL beam [84 85].

The KU-FEL facility had adopted a spherical mirror for the FEL beam transport line [86, 87]. The FEL beam was extracted from the optical cavity through an out-coupling hole, which had a 2-mm diameter until 2011. In 2011, the FEL facility was upgraded, and the diameter of the out-coupling hole was reduced from 2 mm to 1 mm to extend the tunable wavelength of the FEL by reducing loss in the optical cavity. This change almost doubled the divergence of the extracted FEL beam, causing high transportation loss of the FEL from the out-coupling hole to the user stations because the beam size was too large for the beam transportation line. A part of the FEL beam was blocked by a duct covering the trajectory of the FEL beam. Therefore, we designed and constructed a new FEL beam transport system by changing the position and radius of curvature of the spherical mirror.

The aim of the new FEL beam transport line is to make the FEL beam quasi-parallel while maintaining the beam radius (in a quasi-parallel FEL beam system), which defined as twice the standard deviation (σ) of the Gaussian beam. The target beam radius should be less than 17.7 mm at an FEL wavelength of 5–20 μm because mirrors with a diameter of 50 mm are used for the FEL beam transportation and installed at an oblique angle of 45˚, which makes the effective mirror radius 17.7 mm.

4-2 Construction of the FEL beam transportation line

4-2-1 Design of the FEL quasi-parallel beam system

Figure 4.1 depicts the FEL quasi-parallel beam system in the FEL beam transportation line. The FEL beam is extracted from the out-coupling hole in the mirror chamber. A quasi-parallel FEL beam is realized using the spherical mirror. A red diode laser overlaps with the trajectory of the FEL beam for visualization. Part of the FEL beam is reflected onto the ZnSe window, which is used by the mercury cadmium zinc telluride (MCZT) detector to confirm the time evolution of the FEL. The quasi-parallel FEL beam is transported to the user stations via gold flat mirrors.

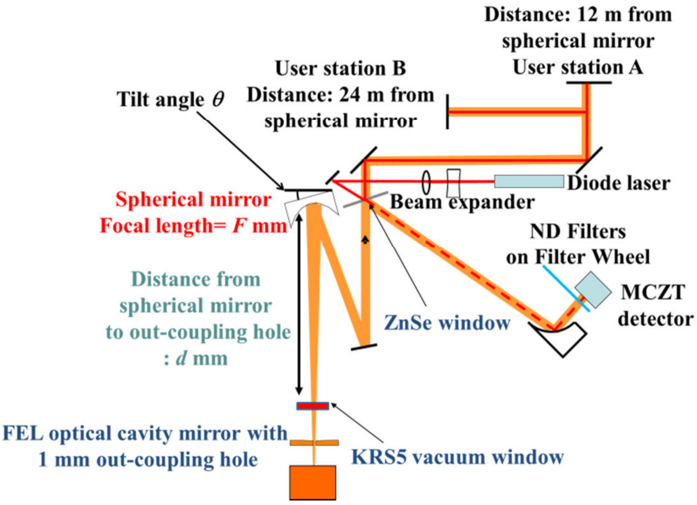

Fig. 4.1. Overview of the FEL quasi-parallel beam system.

The beam size of the quasi-parallel FEL beam in the FEL beam transport line depends on the distance (d) between the spherical mirror and the out-coupling hole, as well as the focal length of the spherical mirror (F). The distances between the user stations A and B and the out-coupling hole are assumed to be 12 m and 24 m, respectively. The tilted angle of the spherical mirror is defined to be θ.

4-2-2 **Calculation of the beam size at the user stations**

4-2-2-1 **Calculation conditions**

The FEL beam profile at the out-coupling hole is considered to have an the Airy disk pattern, owing to the circular aperture. The central part of the Airy disk can be approximated by a Gaussian beam, and then the beam waist at the out-coupling hole is calculated. The intensity of the Airy disk at a distance R is expressed as:

$$\begin{aligned} I(\theta) &= I_0\left(\frac{2J_1(x)}{x}\right)^2 \\ x &= ka\sin\theta = \frac{2\pi aq}{\lambda R}, \end{aligned} \tag{31}$$

where I_0 and $J_1(x)$ are the intensity of the center of the diffraction pattern and the Bessel function of the first kind, respectively; k and λ are the wavenumber and the wavelength of the light, respectively; a is the radius of the circular aperture; and q is the beam radius at the point of observation. Table 4.1 shows the parameters of the FEL. Using these parameters, Figure 4.2 shows the profile of the Airy disk (black) and the fitted Gaussian curve (red).

Table 4.1. Calculation parameters.

λ (μm)	7.5
R (mm)	1000
a (mm)	0.5

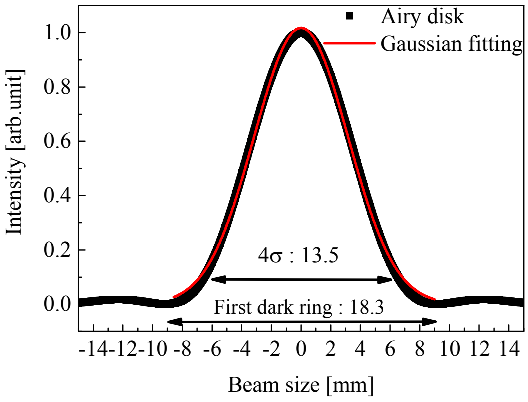

Fig. 4.2. Beam profile of the Airy disk and the fitting curve with a Gaussian beam.

The calculated diameter of the first dark ring in the Airy disk at R = 1000 mm is 9.14 mm. In general, the beam diameter of the Airy disk is defined as 4σ, which is 13.5 % (1/e^2) of the maximum intensity. We fitted the profile of the Airy disk with a Gaussian curve. The standard deviation (σ) is 3.36 mm. Therefore, the beam radius of the Airy disk (2σ:W) is 6.72 mm. Figure 4.3 depicts the relationship between the aperture and beam size at R = 1000 mm. Then, using the values of R and W, the divergence of the FEL beam from the aperture is calculated as 6.7 × 10^{-3} rad.

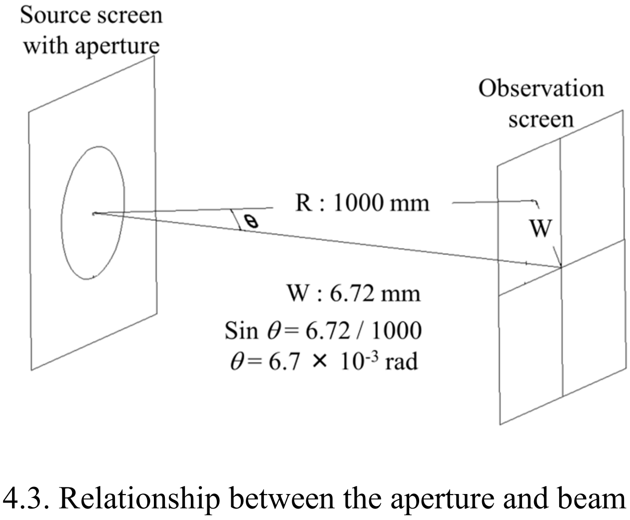

Fig. 4.3. Relationship between the aperture and beam shape.

In the far-field case, the beam waist is given as:

$$\omega_0 = \frac{\lambda}{\pi\theta}. \tag{32}$$

From Eq. (32), the beam waist at the circular aperture (ω_0) is 0.36 mm. Additionally, the diameter of the first dark ring in the Airy disk is expressed as:

$$\sin\theta = 1.22\frac{\lambda}{2a}. \tag{33}$$

The beam radius of the Airy disk (4σ) is 0.737 times the diameter of the first dark ring in the Airy disk, as shown in Fig. 4.2. Therefore, Eq. (33) is converted as:

$$\begin{aligned} \mathbf{sin}\,\theta &= \mathbf{1.22}\frac{\lambda}{2\boldsymbol{a}} \times 0.737 \\ \lambda &= 2.22\boldsymbol{a}\,\mathbf{sin}\,\theta. \end{aligned} \tag{34}$$

Using Eq. (34), Eq. (32) is converted as:

$$\begin{aligned} \omega_0 &= \frac{\lambda}{\pi\theta} \\ \omega_0 &= \frac{2.22a\sin\theta}{\pi\theta}. \end{aligned} \tag{35}$$

When θ is very small, sin θ can be approximated as θ.

Therefore, Eq. (35) is converted to:

$$\omega_0 = \frac{2.22a\sin\theta}{\pi\theta} = \frac{2.22a}{\pi}, \tag{36}$$

where a is the radius of the circular aperture, which is constant. Therefore, it can be considered that ω_0 is constant for any wavelength. Consequently, it is assumed that the beam waist at the circular aperture (ω_0) is 0.36 mm in the wavelength range of 5 μm to 20 μm, which is the tunable wavelength range of the KU-FEL.

4-2-2-2 **Calculation of the beam size at the user stations**

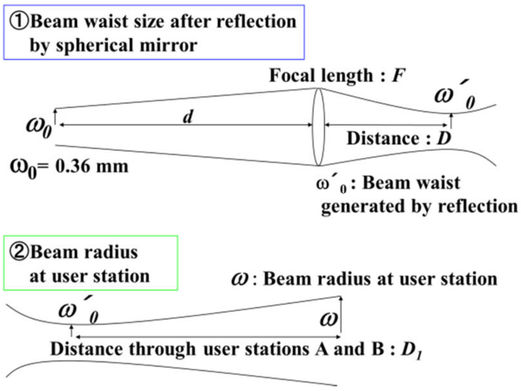

Fig. 4.4. Schematic of the beam size calculation.

Figure 4.4 schematically depicts the beam size calculation for a user station. A spherical mirror that serves as a convex lens is used to create the quasi-parallel beam. When we assume that ω'_0 is the new beam waist introduced by a spherical mirror, *D* is the distance between the spherical mirror and ω'_0. The following equations provide the formula of a lens for a Gaussian beam:

$$\omega_0'^2 = \omega_0^2 \frac{f^2}{(f-d)^2 + \left(\frac{\pi \omega_0^2}{\lambda}\right)^2}$$

F : Focal length of lens, (37)
d : Distance between lens and target,
ω_0: Initial beam waist,
ω'_0:New beam waist,
D: Distance between a lens and position of the new beam waist,

$$D = f + \left(\frac{\omega_0'}{\omega_0}\right)^2 (d_1 - f). \qquad (38)$$

After focusing by the spherical mirror, the FEL beam propagates as a Gaussian beam, which can be expressed as:

$$\omega = \omega_0' \left[1 + \left(\frac{\lambda \boldsymbol{D}_1}{\pi \omega_0'^2} \right)^2 \right]^{\frac{1}{2}} \tag{39}$$

where D_1 = Distance between the position of ω'_0 and ω

Using Eqs. (37), (38), and (39), the beam radii of the transported FEL beam at user stations A and B can be calculated. The calculated wavelengths of the FEL beam are 5, 12, and 20 μm at both user stations A and B. To simplify the calculation, the aberration by the spherical mirror is ignored.

4-2-2-3 **Result**

We calculated the beam sizes at the user stations. The distance between the out-coupling hole and a spherical mirror changes from (F – 100) mm to (F + 100) mm, where F is the focal length of the spherical mirror. Commercially available values spherical mirrors have focal lengths values of 750, 1000, 1500, and 2000 mm. Figure 4.5 shows the results of these calculations.

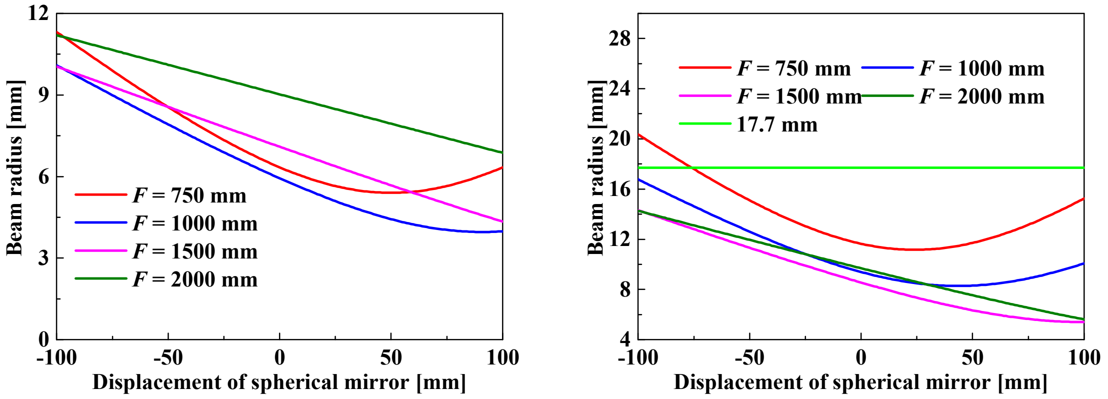

(a) User station A (λ = 5 μm)

(b) User station A (λ = 5 μm)

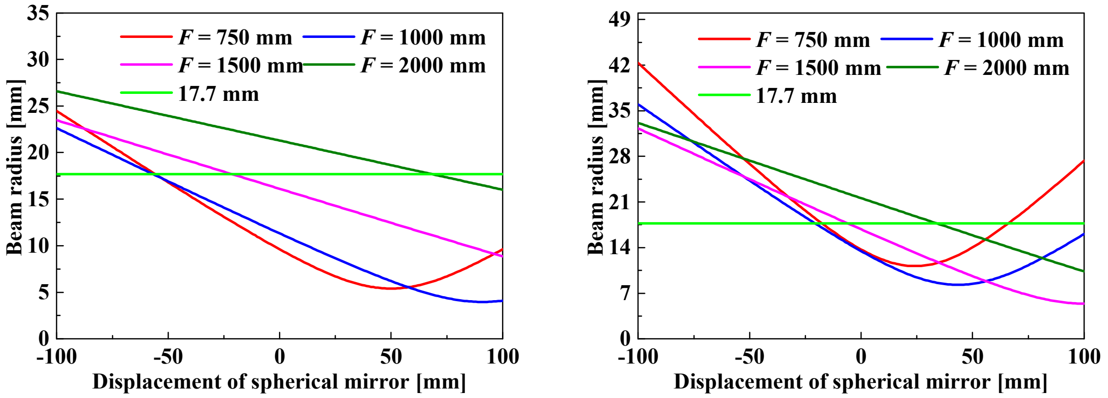

(c) User station A (λ = 12 μm)

User station B (λ = 12 μm)

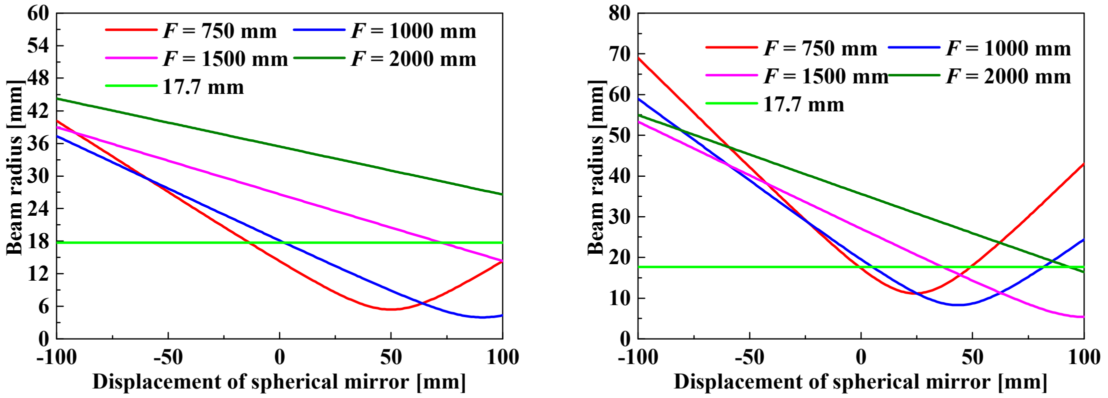

(e) User station A (λ = 20 μm).

(f) User station B (λ = 20 μm)

Fig. 4.5. Effect of the spherical mirror position and focal length on the beam radii for each user station.

From these results, it is obvious that a focal length of 2000 mm cannot be used. Next, we investigated the optimum position (*d*) of each spherical mirror (750 mm, 1000 mm, and 1500 mm) by using optics calculation software, Zemax. Because of the geometrical limitations of the optics, the tilted angles of the spherical mirrors (750 mm, 1000 mm, and 1500 mm) were defined as 8˚, 6˚, and 3˚, respectively. Figure 4.6 shows the optics configuration for the calculation. The thickness of the vacuum window made by KRS-5 in the mirror chamber is 12.7 mm, the wavelength for calculation is 20 μm, and the beam waist is 0.36 mm.

The results are shown in Fig. 4.7. The beam radius is over 17.7 mm when the 1500 mm-spherical mirror is used. On the other hand, when the 750-mm spherical mirror is used with positions of d = 770 mm, 780 mm, and 790 mm, the beam radii are less than 17.7 mm. Additionally, when the 1000 mm-spherical mirror is used, the beam radii are less than 17.7 mm for positions of d = 1030 mm, 1040 mm, and 1050 mm. To transport the FEL beam over such a long distance, a small divergence with a small beam radius is desirable. From Fig. 4.7, obviously, d = 770 mm is the optimum position for smallest divergence with a small beam radius in both horizontal and vertical directions. Hence, a spherical mirror with a focal length of 750 mm can create a quasi-parallel beam when d = 770 mm.

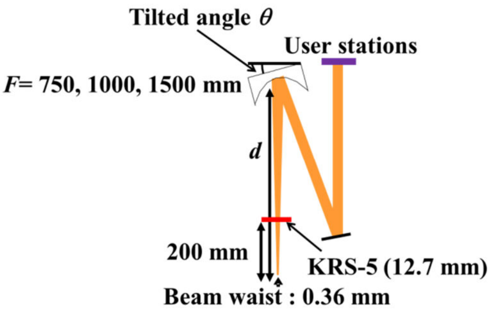

Fig. 4.6. Calculation model for Zemax.

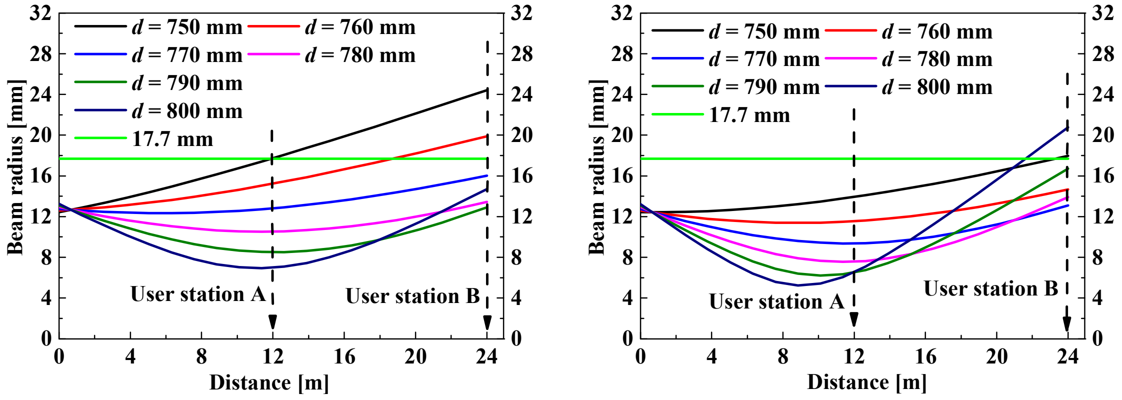

(a) Horizontal direction

(b) Vertical direction

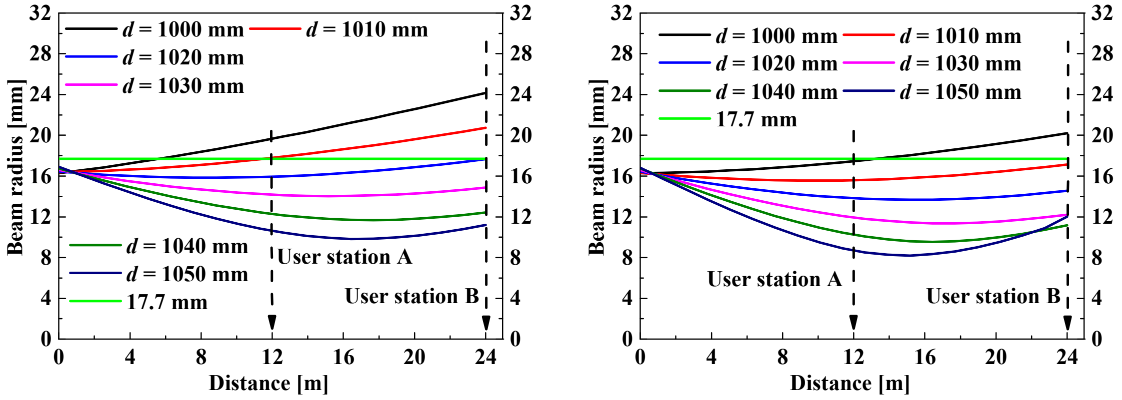

(c) Horizontal direction

(d) Vertical direction

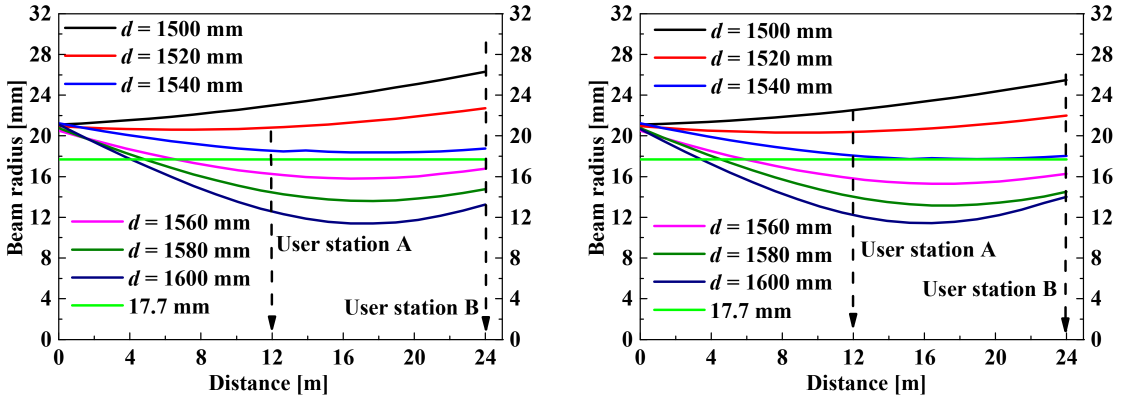

(e) Horizontal direction

(f) Vertical direction

Fig. 4.7. Dependences of the beam radii on the distance from the spherical mirrors with 750, 1000, 1500 mm focal lengths and a FEL wavelength of 20 μm.

4-3 **Measurement of the beam size and beam profile**

A spherical mirror with a focal length of 750 mm was placed at d = 770 mm and an angle of $\theta = 8^{\circ}$ with placement accuracies of $d \pm 10$ mm and $\theta \pm 1^{\circ}$. To evaluate the results calculated in Section 4-2-2-3, the beam profiles were measured using the method described below.

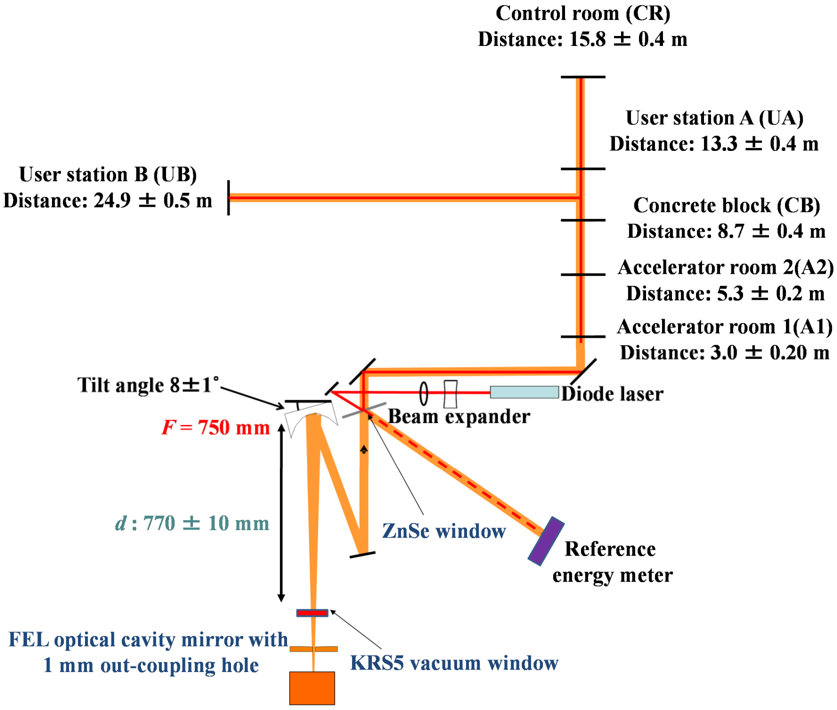

Fig. 4.8. Measurement points and distances from the spherical mirror in the beam profile.

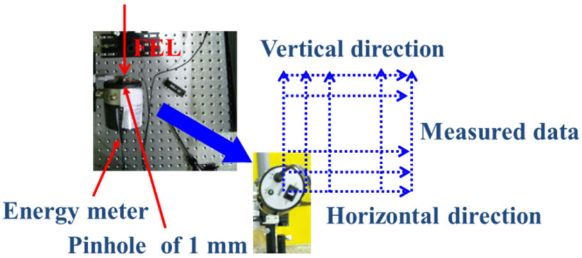

Fig. 4.9. Experimental setup for the beam profile measurement.

The beam profile was measured at six points (Fig. 4.8): accelerator room 1 (A1:distance 3.0 ± 0.2 m), accelerator room 2 (A2: distance 5.3± 0.2 m), the concrete block (CB: distance 8.7 ± 0.4 m), user station A (UA: distance 13.3 ± 0.4 m), the control room (CR: distance 15.8 ± 0.4 m), and user station B (UB: distance 24.9 ± 0.4 m). An energy meter (QE8SP-I-BL-BNC, Gentec-EO) was used as a reference to normalize the observed signal.

Figure 4.9 shows the experimental setup. We set a 1 mm pinhole in front of the detector (Gentec-EO, QE8SP-I-BL-BNC) and measured the intensity of each point by scanning the detector in 2.0 mm (at A1, A2, CB, UA, and CR) or 3.0 mm (at UB) steps in the horizontal and vertical directions. Although an FEL with a long wavelength is suitable to evaluate the calculation results, water vapor and CO_2 in the air absorb photons from 13 μm to 20 μm and the intensity of the generated FEL beam at 20 μm is too low to measure the beam profile using the pinhole. Therefore, a 12-μm-FEL beam, which can generate a high intensity FEL in the KU-FEL and is not absorbed by air, was selected for the beam profile measurements [88].

Figure 4.10 shows the beam profile of the FEL at 12 μm for the CR. The beam profile is not a Gaussian beam; the center of the FEL beam in the horizontal direction has two peaks (Fig. 4.10(b)). The beam profile of the transported FEL should be similar to the Gaussian beam because the FEL beam extracted from the out-coupling hole becomes an Airy disk. This observation indicates that the transported light contains another component.

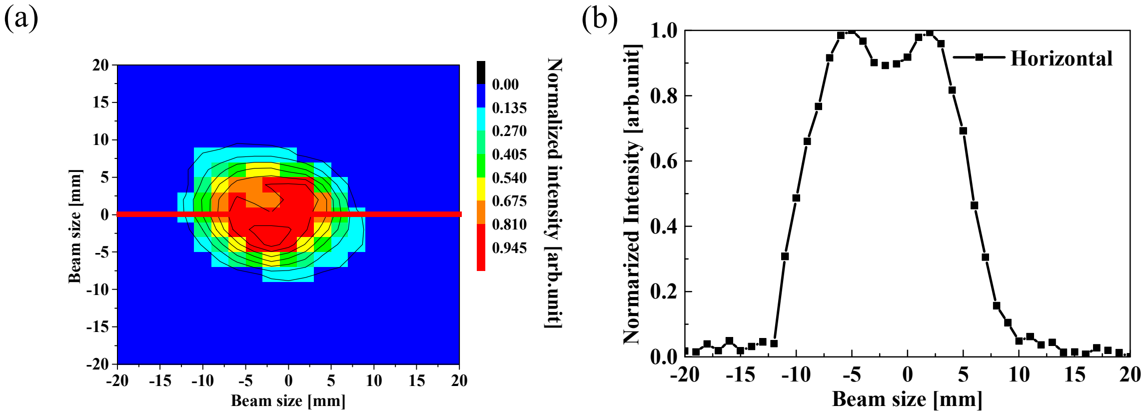

Fig. 4.10. Beam profile of the FEL at 12 μm for the control room (CR) (a) two-dimensional profile and (b) cross-section of the two-dimensional profile in the horizontal direction.

Because the KRS-5 window has a high reflection ratio (30 %) in the MIR region of light [89] and the cavity mirror is made of copper, which has a high reflectivity (over 90%) in the MIR region [90], we hypothesized that the other component is due to multiple reflections of light. Figure 4.11 shows that multiple reflections of light are produced between the KRS-5 window and the cavity mirror.

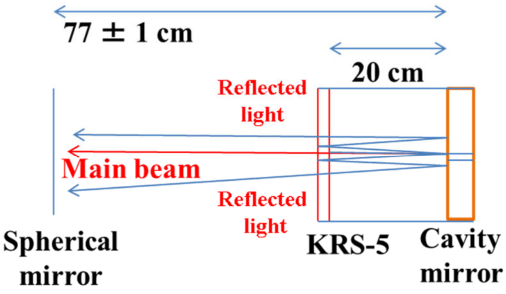

Fig. 4.11. Multiple reflections of light produced between the KRS-5 window and the cavity mirror.

To remove the multiple reflections of light, an aperture with a 10 mm diameter, which is almost the same diameter as the FEL beam, was inserted between the KRS-5 window and the spherical mirror (Fig. 4.12), and then the beam profile was measured at the CR to verify the effect of the aperture. We found that the beam profile at the CR became a Gaussian beam as a result of inserting the aperture (Fig. 4.13). Hence, the non-Gaussian peak is attributed to multiple reflections of light, and all subsequent measurements thus included an inserted aperture.

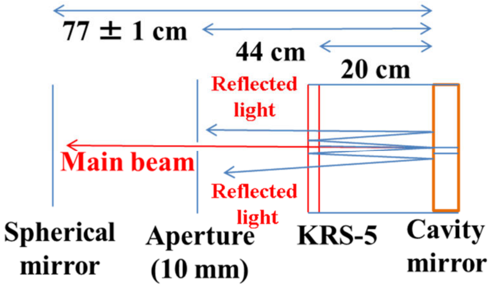

Fig. 4.12. Configuration of the optics between the cavity mirror and the spherical mirror.

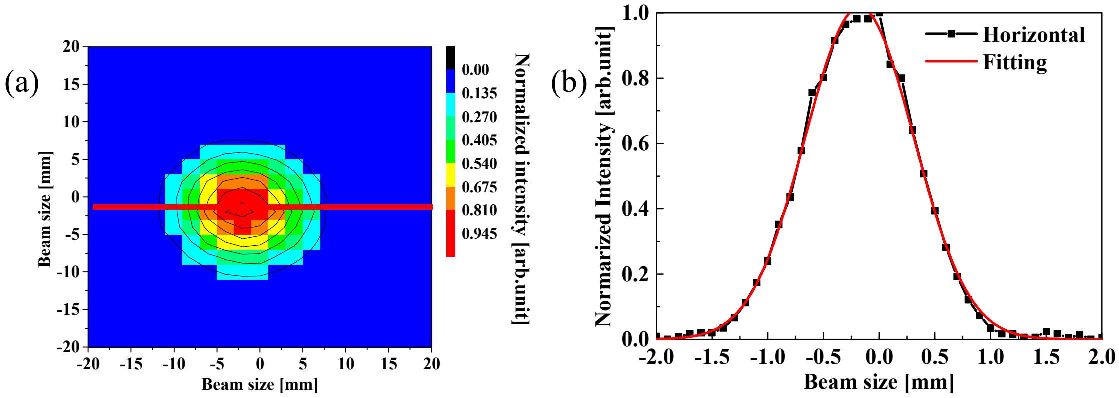

Fig. 4.13 Beam profile of the FEL at 12 μm in the control room (CR) when an aperture is inserted between the spherical mirror and the KRS-5 window (a) two-dimensional profile and (b) cross section of the two-dimensional profile in the horizontal direction.

4-3-1 **Results**

Although some of the measurements indicate contamination from multiple reflections of light, the beam profiles display almost Gaussian beams for each measured point (Fig. 4.14). Figure 4.15 shows the beam radii in the horizontal and vertical directions at each point. The beam radii were calculated from the two-dimensional profile by projection of the horizontal and vertical directions. The horizontal beam radii are larger than the vertical beam radii owing to astigmatism.

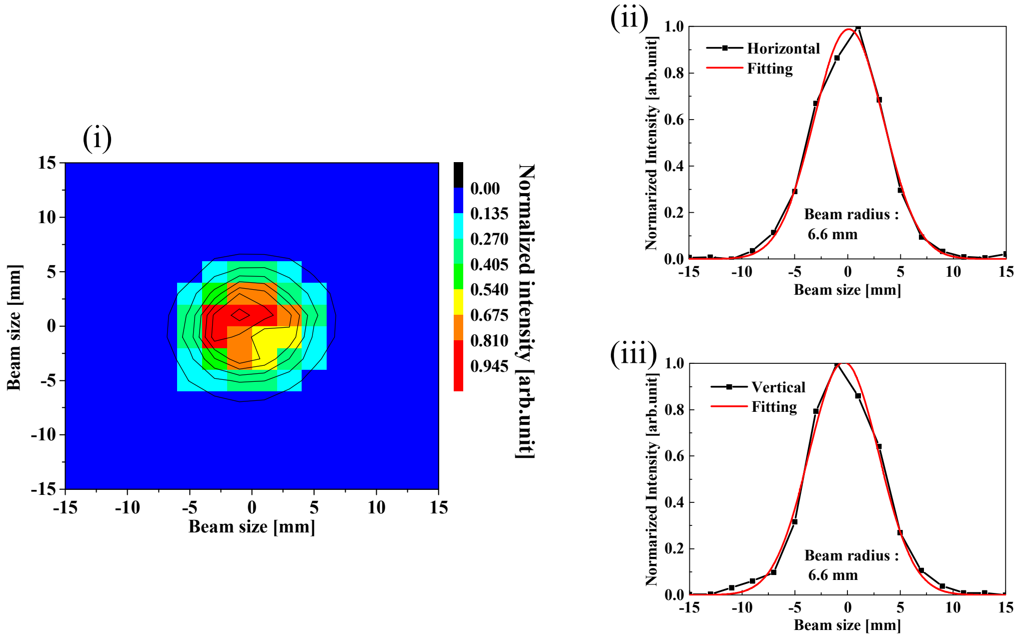

(a) Beam profile at accelerator room 1 (A1): (i) two-dimensional profile, (ii) horizontal direction, and (iii) vertical direction.

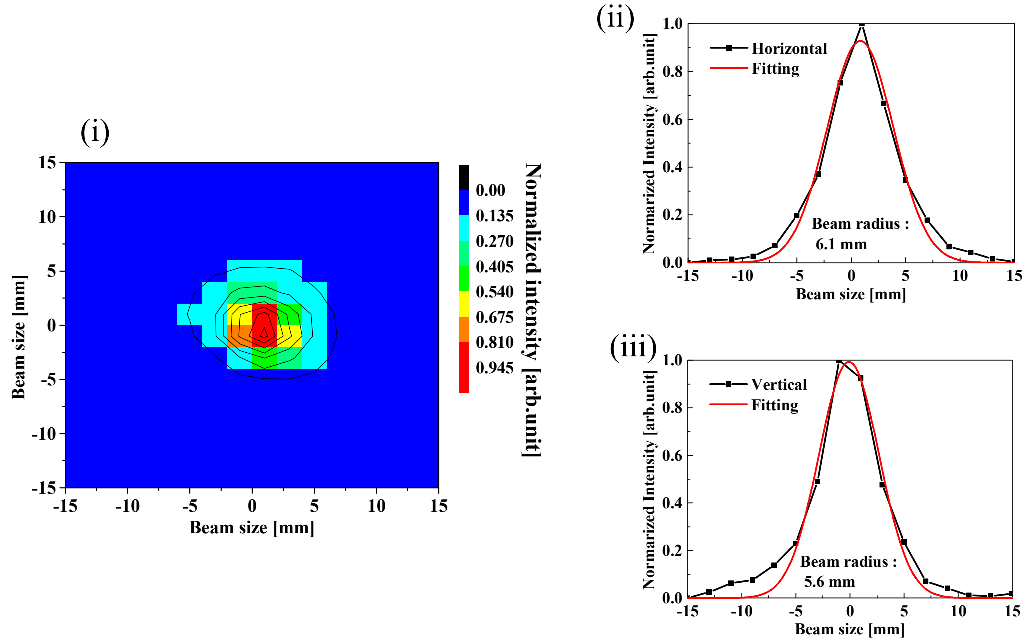

(b) Beam profile at accelerator room 2 (A2): (i) two-dimensional profile, (ii) horizontal direction, and (iii) vertical direction.

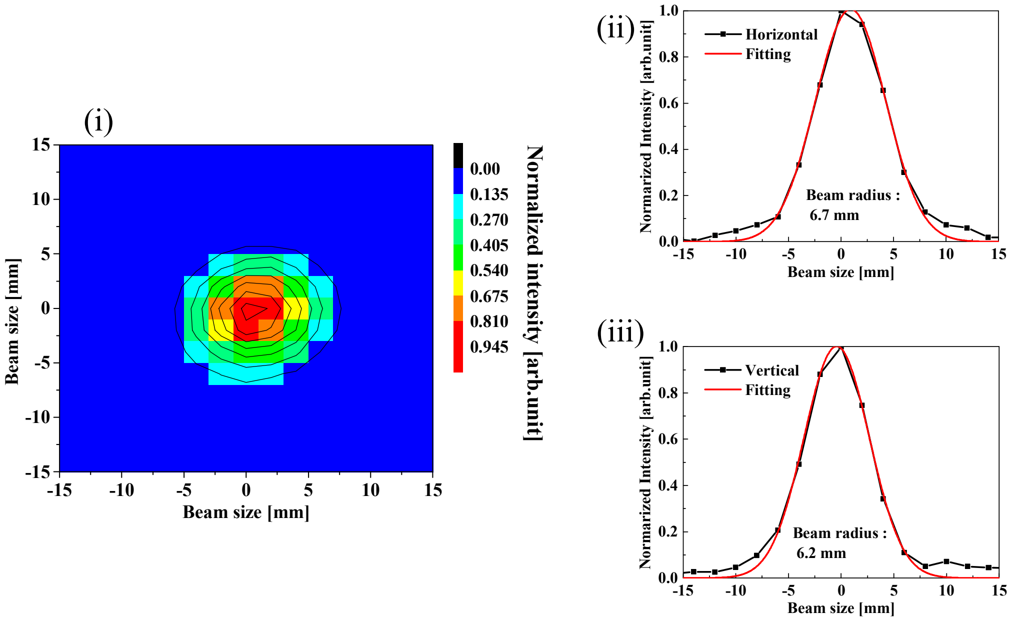

(c) Beam profile at the concrete block (CB): (i) two-dimensional profile, (ii) horizontal direction, and (iii) vertical direction.

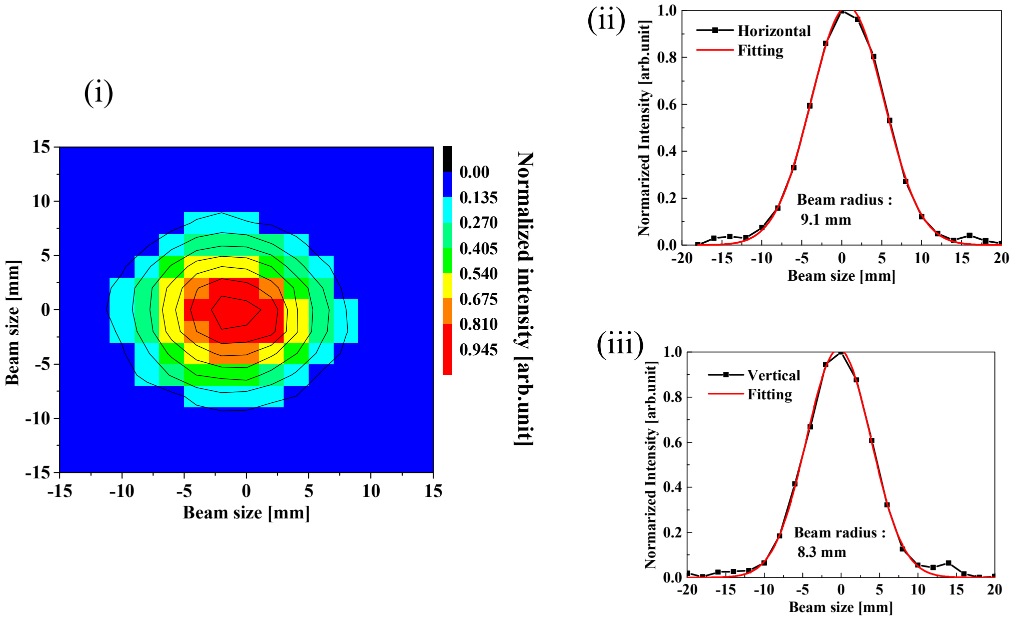

(d) Beam profile at user station A (UA): (i) two-dimensional profile, (ii) horizontal direction, and (iii) vertical direction.

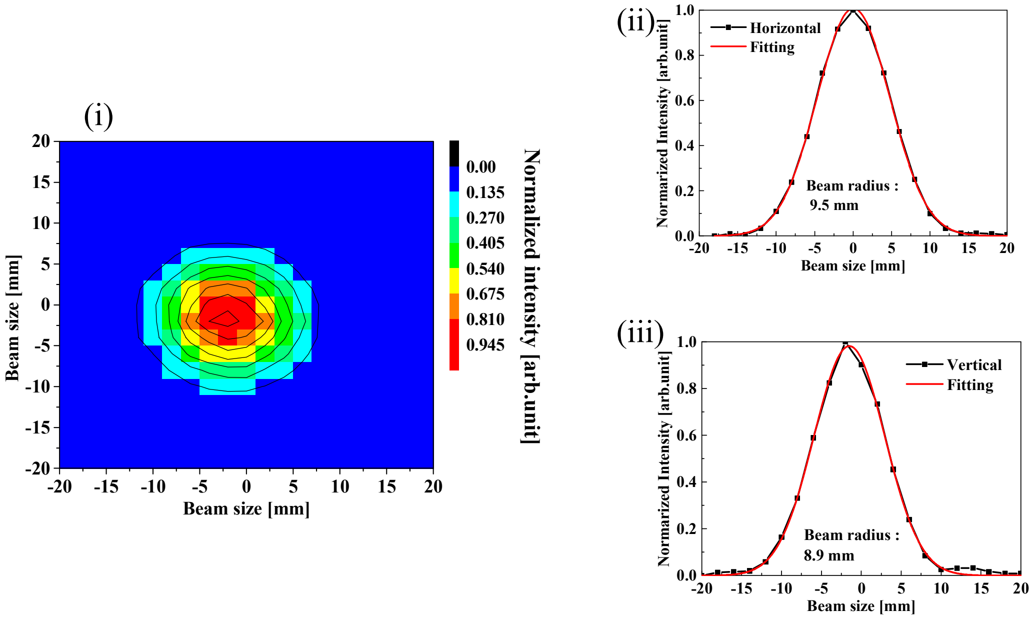

(e) Beam profile at the control room (CR): (i) two-dimensional profile, (ii) horizontal direction, and (iii) vertical direction.

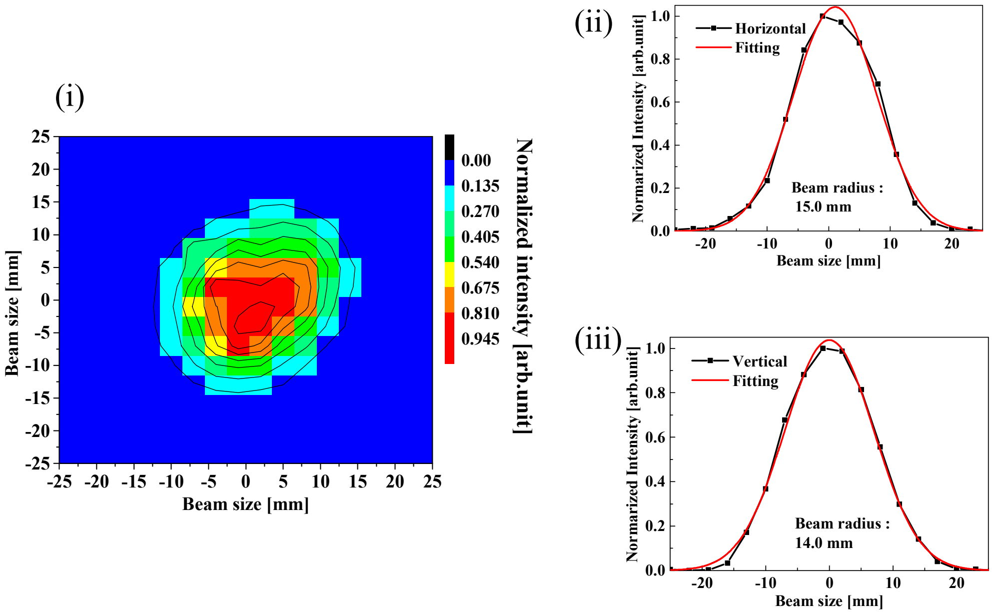

(f) Beam profile at user station B (UB): (i) two-dimensional profile (ii) horizontal direction, and (iii) vertical direction.

Fig. 4.14. FEL beam profiles at the measurement locations when the wavelength is 12 μm.

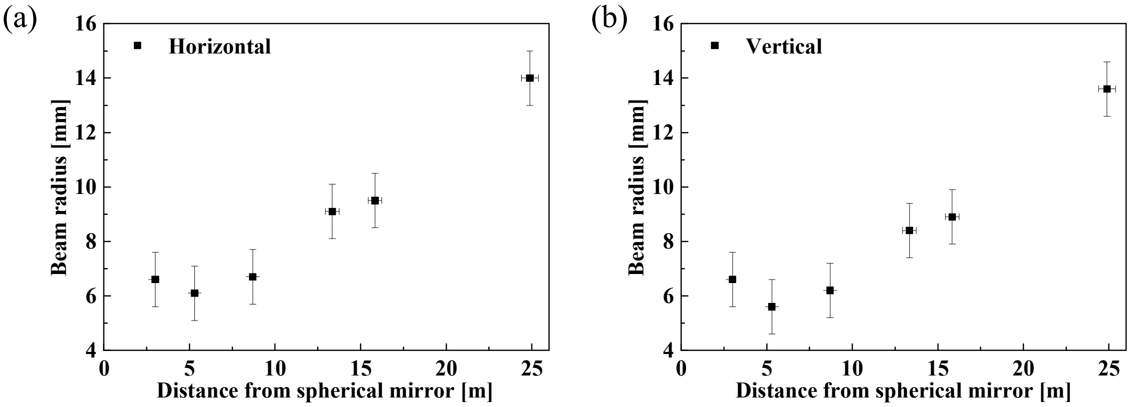

Fig. 4.15. Beam radii for each measurement point in the (a) horizontal and (b) vertical directions.

4-3-2 **Discussion**

Figure 4.16 compares the measured and calculated results. In the calculation model (Fig. 4.6), the wavelength and beam waist were defined as 12 μm and 0.36 mm, respectively. Because the placement accuracies of d and θ were ±10 mm and ± 1˚, the beam radii were calculated in the ranges of d = 760 ~ 780 mm and θ = 7 ~ 9˚. Consequently, the calculation used three different distances (760, 770, and 780 mm) and three different angles (7˚, 8˚, and 9˚).

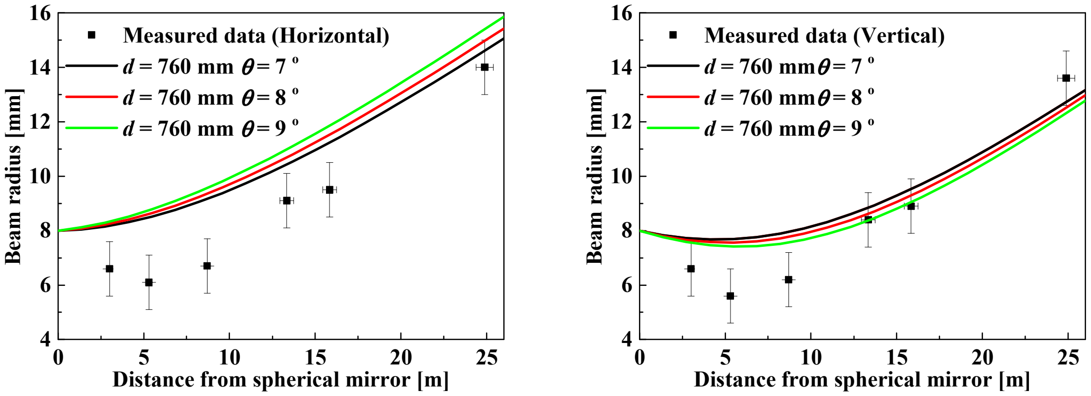

(a) d = 760 mm (Horizontal)   (b) d = 760 mm (Vertical)

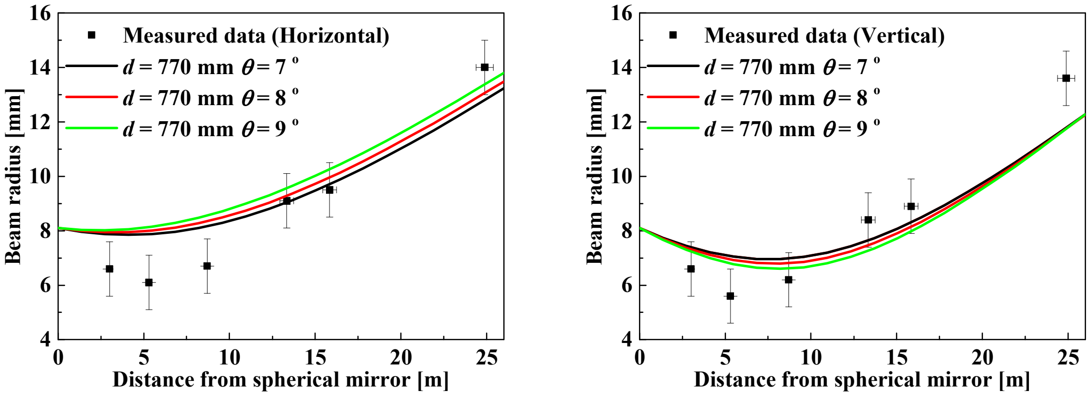

(c) d = 770 mm (Horizontal)   (d) d = 770 mm (Vertical)

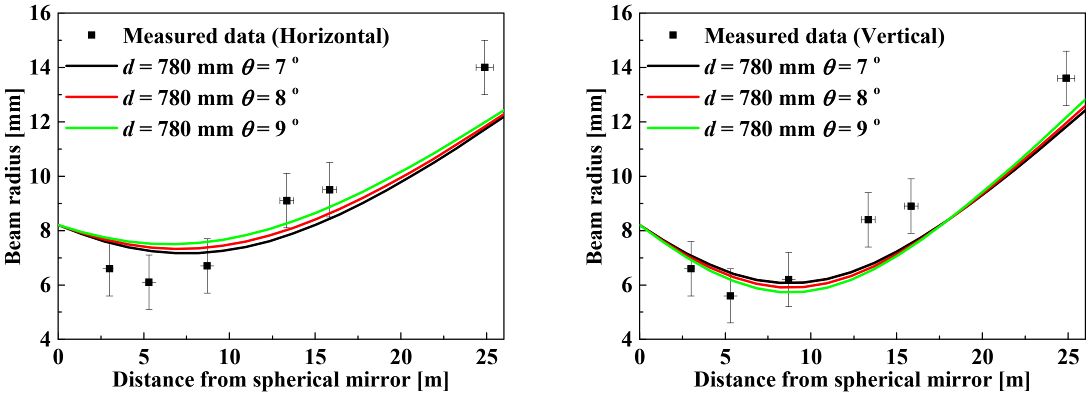

(e) d = 780 mm (Horizontal)   (f) d = 780 mm (Vertical)

Fig. 4.16. Comparisons between the measured and calculated results.

However, the measured results did not match the calculation results. It is believed that the beam waist used in the calculation differs from the real value because propagation of the Gaussian beam depends only on the beam waist when the wavelength is constant. Therefore, we calculated the real value of the beam waist (ω_0) from the measured beam radius.

To calculate the beam waist at the out-coupling hole (ω_0), Eq. (39), which expresses Gaussian beam propagation, was used for a fitting as shown in Fig. 4.17 to determine the size and the position of the beam waist produced by the spherical mirror (ω_0' and *D* in Fig. 4.4). The values of ω_0' and *D* were determined as Table 4.2 by the fitting in Fig. 4.17.

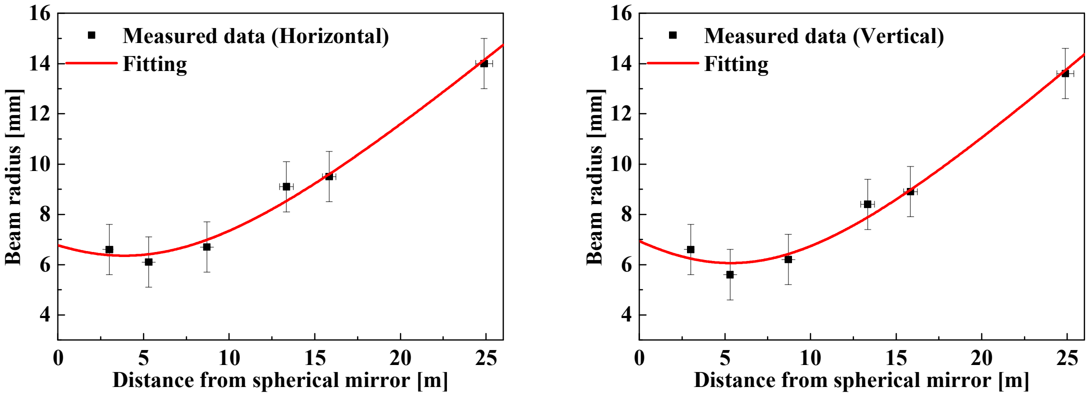

Fig. 4.17. Results of the fitting with the equation for Gaussian beam propagation.

Table 4.2. Results of the fitting parameters.

	ω_0' (mm)	D (m)
Horizontal	6.4 ± 0.2	3.9 ± 0.5
Vertical	6.1 ± 0.2	5.3 ± 0.5

Next, the size of the beam waist at the out-coupling hole was calculated using the parameters shown in Table 4.2 (ω_0' and D) and by simultaneously solving Eqs. (37) and (38). However, the focal length of the spherical mirror changes when the light has an oblique incidence. Figure 4.18 shows the change in the focal length of a spherical mirror resulting from an oblique incidence. The focal length at normal incidence is F mm, but that at oblique incidence changes to $F/\cos\theta$ mm, as shown in Fig. 4.18. Therefore, the focal length of the spherical mirror changes from 750 mm to 757 mm (750 / cos 8°) when the size and position of the beam waist in the horizontal direction are calculated.

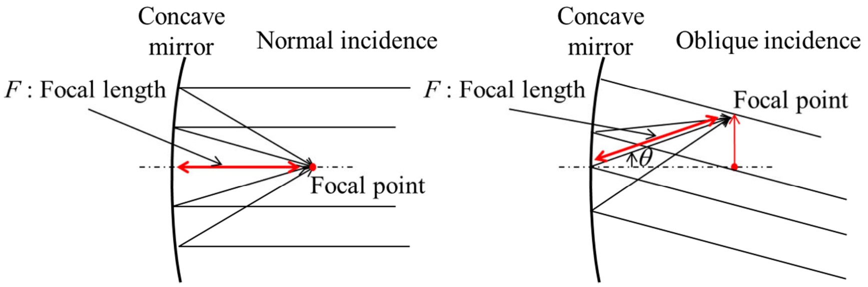

Fig. 4.18. Change in the focal length of a spherical mirror.

Table 4.3. Calculation results.

	ω_0' (mm)	D (m)	ω_0 (mm)	d (m)
Horizontal	6.4 ± 0.2	3.9 ± 0.5	0.43 ± 0.02	0.77 ± 0.01
Vertical	6.1 ± 0.2	5.3 ± 0.5	0.43 ± 0.02	0.77 ± 0.01

Table 4.3 shows the calculation results. The horizontal and vertical parameters (ω_0 and d) match. Next, we verified the beam radii by using a Zemax simulation and the determined fitting parameters (ω_0 = 0.43 mm and d = 0.77 m). Figure 4.19 shows the calculation model of the beam radii. The KRS-5 window was ignored because ω_0 and d were calculated from the model without the KRS-5 window. Figure 4.20 compares the recalculated and measured beam radii. The recalculated beam radii agreed with the measured beam radii. Consequently, the size and position of the beam waist at the out-coupling hole are 0.43 mm and 0.77 m, respectively.

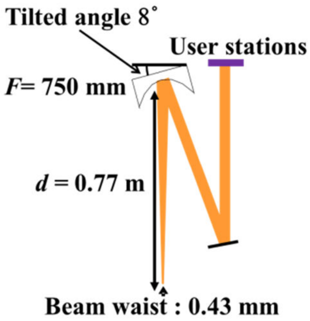

Fig. 4.19. Calculation model of the beam radius calculated from ω_0 = 0.43 mm and d = 0.77 m .

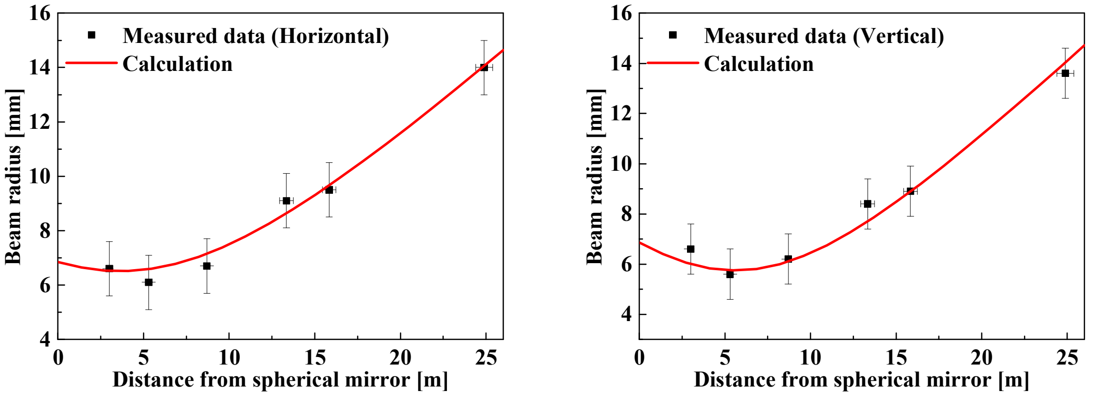

Fig. 4.20. Comparison of the recalculated and measured beam radii. The calculation uses the parameters determined from the measured data (ω_0 = 0.43 mm and d = 0.77 m).

4-3-3 **Confirmation of matching with the design concept**

In Section 4-3-2, the beam waist at the out-coupling hole in the real condition was determined. To verify that the present parameters of the spherical mirror, where F = 750 mm and d = 770 mm, satisfy the design concept of the FEL quasi-parallel beam system, the beam size using the 750 mm spherical mirror was calculated using the conditions of Fig. 4.19 and a wavelength of 20 μm. Figure 4.21 shows the dependences of the beam radii on the distance from the spherical mirror at 20 μm. When d is between 750 mm and 780 mm, the beam radius is less than 17.7 mm at any location in the transport system, which satisfies the design concept of the FEL transport line. Therefore, the FEL quasi-parallel beam system adopts the present parameters of the spherical mirror (F = 750 mm and d = 770 mm).

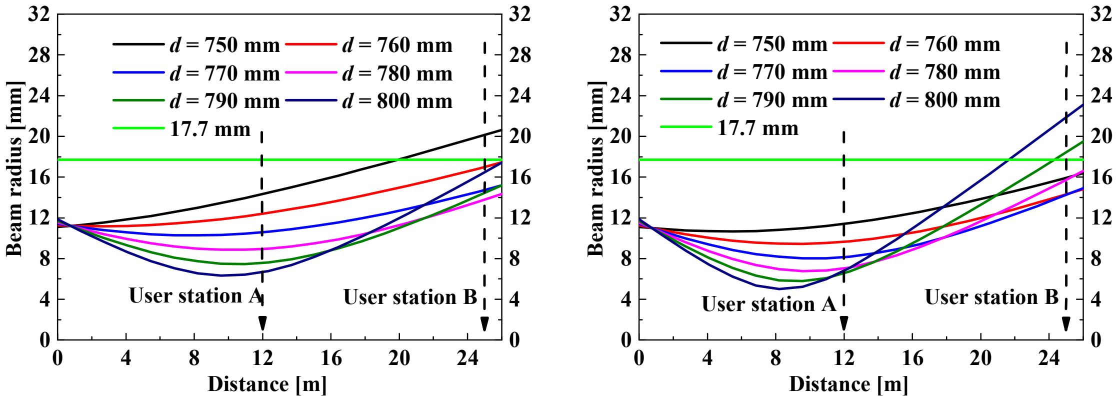

Fig. 4.21. Dependences of the beam radii on the distance from the spherical mirror (F = 750 mm and d = 770 mm) at a wavelength of 20 μm.

4-4 **FEL transportation ratio**

4-4-1 **Experimental setup and conditions**

To verify that the constructed FEL quasi-parallel beam system can transport the FEL beam effectively, the FEL transportation ratios between the accelerator room to each user station was measured. Figure 4.22 shows the experimental setup for the transportation ratio measurement. An energy meter (Gentec-EO, QE8SP-I-BL-BNC) was placed in the accelerator room as a reference energy meter. The transportation ratio was measured at three points: the accelerator room (AR), user station A (UA), and user station B (UB). The distances from AR to UA and to UB were 12 m, and 24 m, respectively. The FEL intensity at each measured point was measured using an energy meter (Newport, 818E-20-50S), and the FEL wavelength was 12 μm.

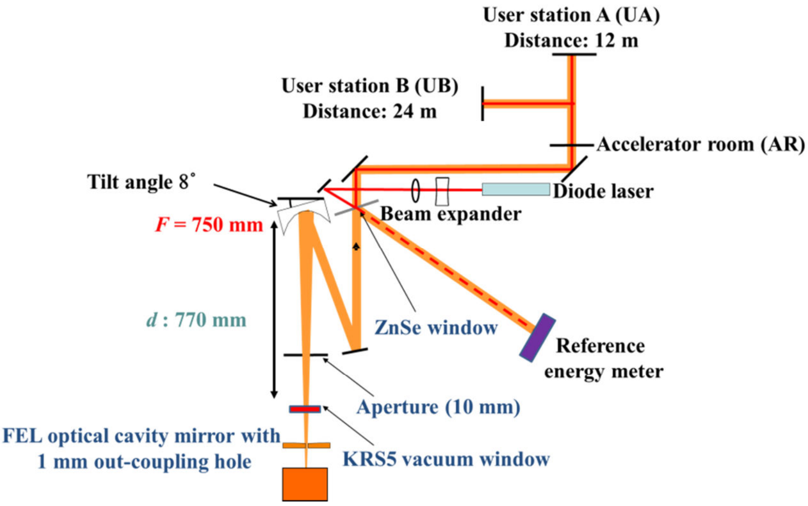

Fig. 4.22. Experimental setup for measurement of transportation ratio.

4-4-2 **Results and discussion**

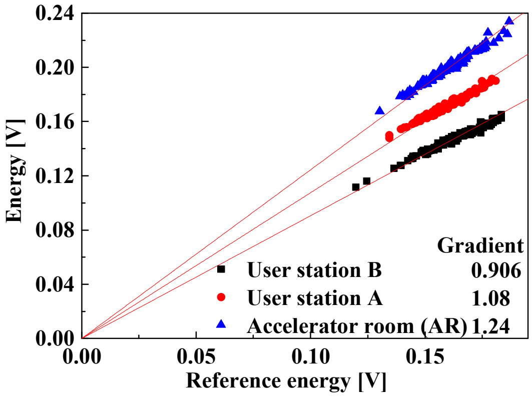

Fig. 4.23. Results of the transportation ratio measurements.

The transportation ratios between AR and UA and UB are 87% and 73%, respectively (Fig. 4.23). The ratios were calculated by dividing the gradient of the fitting lines of UA and UB by that of AR.

To transport the FEL beam, three and six gold flat mirrors are used in user stations A and B, respectively. The reflection ratio of a gold flat mirror placed at an oblique angle of 45° is 96% for both s polarization and p polarization [91]. The ideal transportation ratios from AR to UA and to UB are 88% and 78%, respectively. The measured transportation ratios are lower than the ideal values.

The FEL intensity at AR is stronger than at the other measured points because the FEL beam in the accelerator room may contain multiple reflections of light, as explained in Section 4-3-1. Therefore, the enhanced FEL intensity at AR due to contamination from multiple reflections of light decreases the transportation ratio.

In conclusion, the FEL beam can be transported through user station A and B. with transportation ratios of 87% and 73%, respectively. However, multiple reflections of light may affect the transportation ratios between the accelerator room and the user stations. Hence, the insertion of an aperture between the KRS-5 window and the copper cavity mirror, *etc.* are recommended to prevent contamination.

4-5 **Confirmation of the effectiveness of the N_2 gas filling**

4-5-1 **Objective**

Light in the MIR region is absorbed by water vapor or CO_2, especially in the region from 5 μm to 8 μm [92]. For example, the absorption coefficient of water vapor at 6.6 μm is 2.0 $\mathrm{cm^{-1}atm^{-1}}$ [92]. The transmittance (T) of the light in a gas is expressed as:

$$\frac{100I}{I_0} = T = 100e^{-kLp} \quad (\%) \tag{40}$$

I : Intensity of the light,
I_0 : Initial intensity of the light,
T : Transmittance,
k : Absorption coeffecient $(cm^{-1}atm^{-1})$,
L : Distance (cm),
p : Partial pressure (atm).

To calculate the transmittance on a rainy day, which is the condition of high humidity, we assumed that the humidity was 80%. The normal temperature and pressure were defined as 300 K and 1 atm, respectively. Therefore, the partial pressure of the water vapor at 300 K, 1 atm in air, can be calculated by the equation of state:

Amounts of saturated vapor at 300 K is 23.1 (g/m^3)

$$\therefore 23.1 \times 0.8 = 18.5 (\boldsymbol{g/m^3}) = 1.03 \times 10^{-3} \boldsymbol{mol/\ell}$$

Therefore, the water vapor contains 1.03 mol in air of 1 ℓ.
By using equation of state ($PV = nRT$)

$$\boldsymbol{p} = 1.03 \times 10^{-3} \times 0.082 \times 300$$

(p : Partial pressure of water vapor in air)

$$\boldsymbol{p} = 2.5 \times 10^{-2} \,(\boldsymbol{atm})$$

Using Eq. (40), the transmittances at user stations A and B are calculated as

$$T = 100 \times e^{-2.0 \times 2.5 \times 10^{-2} \times 1200} = 8.7 \times 10^{-25} \approx 0$$
(@ user station A)
$$T = 100 \times e^{-2.0 \times 2.5 \times 10^{-2} \times 2400} = 7.7 \times 10^{-51} \approx 0$$
(@ user station B).

The transportation ratio from the out-coupling hole to a user station dramatically decreases as a result of absorption by water vapor. Water vapor decays the intensity of MIR light at around 6 μm. Additionally, another absorption phenomenon occurs in the FEL spectrum (Fig. 4.24), as the MIR-FEL at 10.6 μm is absorbed by the atmosphere. A potential candidate for a substance that absorbs the photon at 10.6 μm is SF_6 gas leaking from the waveguide used in the accelerator tube and water vapor excited by a high intensity laser [93, 94]. For efficient FEL beam transportation, substances that absorb the FEL beam must be removed. Hence, the FEL beam transportation line is covered by a polyethylene pipe, which is filled with nitrogen gas to remove FEL-absorbing substances.

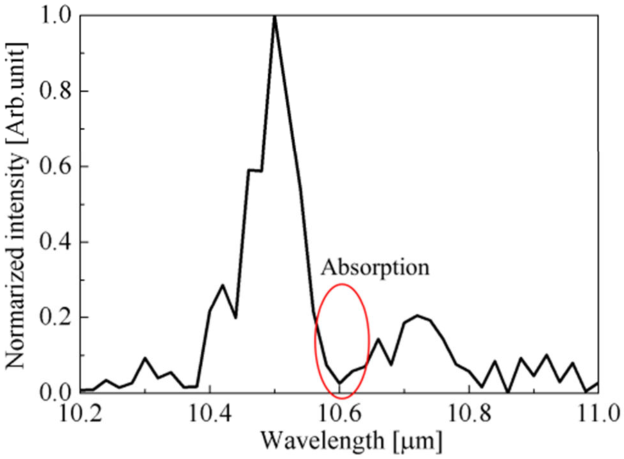

Fig. 4.24. The MIR-FEL spectrum around 10.6 μm.

4-5-2 N_2 flow system and the result of N_2 gas filling.

We constructed an N_2 gas filling system in the FEL beam transport line to prevent MIR-FEL absorption. Our system uses vinyl chloride pipes to cover the FEL beam transport line, and an acrylic board to cover the FEL quasi-parallel beam system in an accelerator room. N_2 gas is injected from the application room and the FEL control room at a rate of 5 ℓ/min. The N_2 gas filling is confirmed by an analog humidity meter in the FEL beam transport line. After three hours, the humidity meter showed 0%. To verify the effectiveness of the N_2 gas filling at user station A, we measured the FEL spectrum at 10.5 μm. The spectrum was measured by a monochromator (Digitron, DK240) and a single-channel detector (Gentec-EO, QE8SP-I-BL-BNC). The observed signal was normalized by an reference energy meter (Newport, 818E-20-50S). Each measurement of the spectrum was averaged over 5 shots. The spectrum was then averaged twice. Figure 4.25 shows the results. Because the wavelength stability at one shot was quite low, the error bar is large in the case with N_2 gas filling. However, it is obvious that the intensity at 10.6 μm is enhanced by the N_2 gas filling. Therefore, it is confirmed that the N_2 gas filling effectively inhibits absorption of the MIR-FEL beam by the absorbing substances (Fig. 4.25).

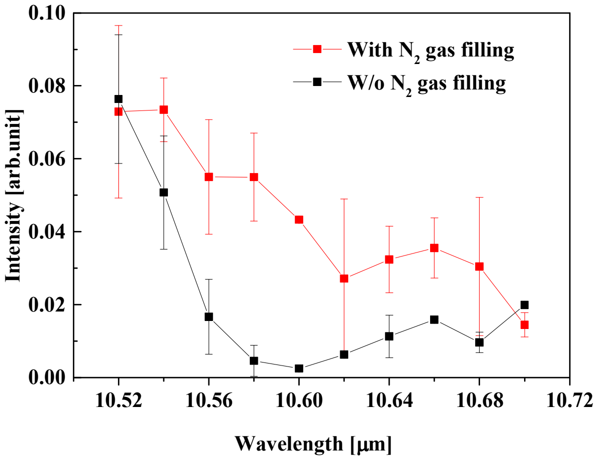

Fig. 4.25. Difference between the spectra with and without N_2 gas filling.

Additionally, the change in the transportation ratio due to N_2 gas filling was measured at user station A with an FEL wavelength of 6.6 μm, because this is wavelength with the strongest absorption between 5 μm to 20 μm. Figure 4.26 shows the experimental setup to measure the transportation ratios with and without N_2 gas fillings. A KBr window with a diameter of 30 mm and a thickness of 4 mm was used. Figure 4.27 depicts the change in the transportation ratio. The transportation ratio with N_2 gas filling is almost three times that without N_2 gas filling. Moreover, the linearity of the observed signal without N_2 gas filling is worse than that without N_2 gas filling. The difference in the linearity may be induced by the fluctuation of the FEL wavelength in one shot, because the absorption coefficient of air in the MIR region is not constant. For example, the absorption coefficient at 6.6 μm is four times that at 6.8 μm [88]. Therefore, the amount of absorption of the MIR-FEL beam by air strongly depends on the center wavelength. It is confirmed that the KU-FEL exhibits wavelength instability [51], and it may induce a change in the transportation ratio.

Consequently, by observation of the change of the FEL spectra and the transportation ratio with and without N_2 gas filling, it was confirmed that the N_2 gas filling system is effective for FEL transportation.

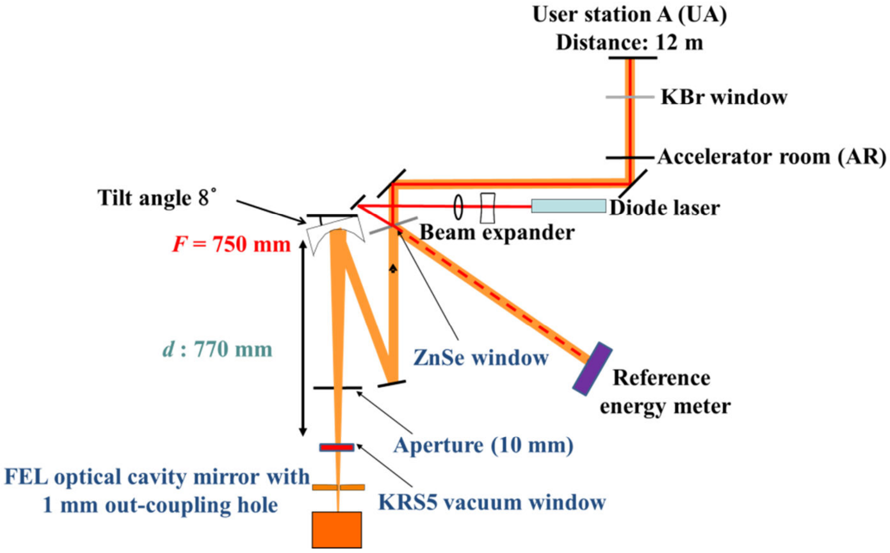

Fig. 4.26. Experimental setup for the transportation ratios with and without N_2 gas fillings.

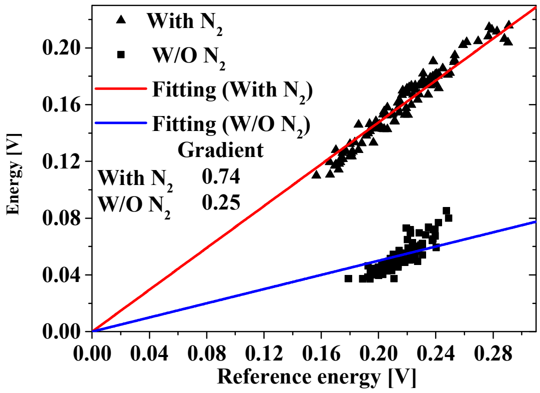

Fig. 4.27. Results of the transportation ratio measurement

with and without N_2 gas filling.

4-6 **Observation of the high harmonics in the MIR-FEL beam in the KU-FEL**

4-6-1 **Objective**

High-harmonic radiation from an FEL oscillator was initially observed at the ACO storage ring in France by Girard *et al.* [95]; they observed coherent light at 355 nm, which corresponds to the 3rd harmonic of 1064-nm light using optical klystron. Moreover, the 6th and 7th harmonics (533 nm, 457 nm) of the light with a fundamental wavelength of 3.2 μm were observed at Mark III at Stanford University. Additionally, the 3rd harmonic (500 nm) of light with a fundamental of 1.5 μm was observed in LEBRA at Nihon University [26-].

Harmonics are generated in an FEL oscillator without nonlinear optical material. Figure 4.28 shows the mechanism for harmonic generation by an FEL. When the width of the microbunch is broad as shown in Fig. 4.28 (a), an electromagnetic wave whose wavelength is a microbunch interval (λ) is generated as a fundamental. However, if the energy of the microbunches is modulated strongly, then each microbunch width becomes narrow. The microbunch is considered to be a wave composed of overlapping sine waves by the uncertainty principle. Therefore, the harmonics of fundamental are also generated when the width of the microbunch is narrow.

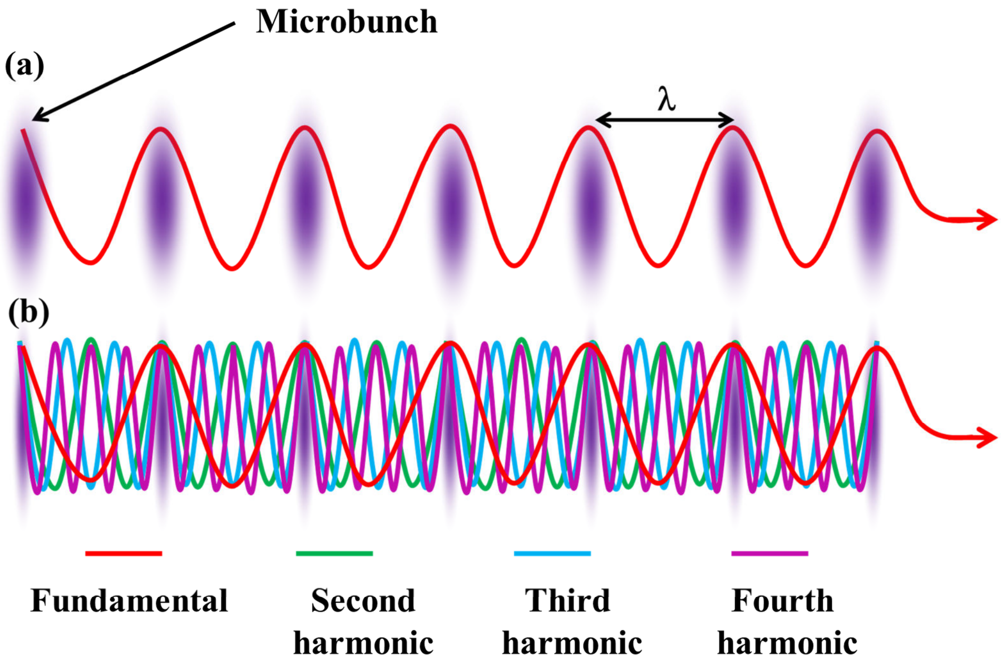

Fig. 4.28. Schematic of the principles of harmonic generation in an FEL.

Although the generation of harmonics in an FEL oscillator has a harmful effect on optics (*e.g.*, damage of dielectric multilayer mirrors used in an optical cavity [27]), the harmonics should be useful for FEL applications and operations. One example is the use of short-wavelength coherent radiation by generating harmonics, which is very beneficial to FEL users. Because harmonics are sensitive to electron phase motion in FELs, they can be used to study the basic physics of interactions (*e.g.*, electron beam emittance, electron beam energy spread, *etc.*) [27]. Additionally, wavelength scanning with a single-channel detector can verify the wavelength of an

MIR-FEL instead of employing a very expensive multi-channel detector in the MIR region. It is difficult for wavelength scanning by a single-channel detector to measure the single-shot spectrum of an MIR-FEL. However, converting the wavelength from MIR to visible light with high-harmonic generation can measure the single-shot spectrum [28].

For the MSPE experiment, the harmonics in the FEL beam may induce unexpected phenomena (*e.g.*, contamination by strange peaks in the spectrum and unexpected chemical reactions). For example, 6H silicon carbide (SiC), which is one of semiconductors, absorbs light at 20 μm and 10 μm [38]. If an FEL with a wavelength of 20 μm is radiated onto 6H-SiC for MSPEs, with a wavelength an FEL of 10 μm is also radiated by the harmonics. It may induce the excitation of two phonon modes, which is non-mode-selective phonon excitation. Therefore, it is essential to verify whether the FEL beam contains harmonics. We verified the harmonics in the FEL beam at the KU-FEL by determining the harmonics from near-infrared to visible light, because the photoluminescence system and the Raman scattering system in the KU-FEL can detect the light in this range.

4-6-2 **Experimental setup**

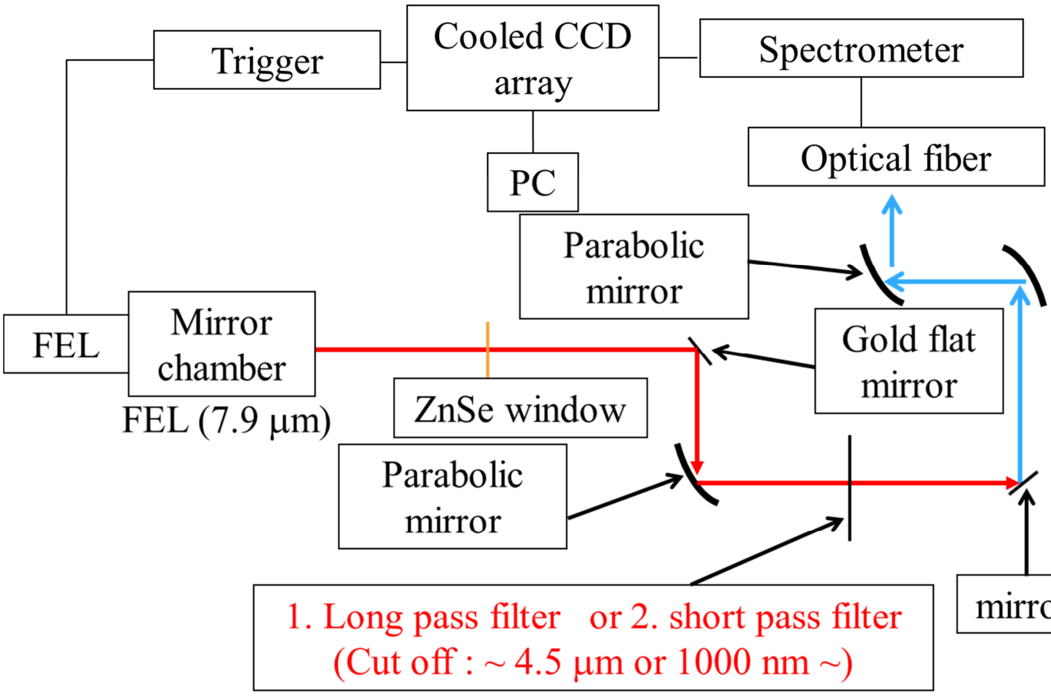

Fig. 4.29. Experimental setup to confirm the harmonics.

Figure 4.29 depicts a schematic of the experimental setup to confirm the harmonics. A spectrometer (Zolix Omni-λ, 300) and a charge-coupled device (CCD) array (Intevac, Mosir 350) were used for detection. The CCD array was triggered by the master trigger of the KU-FEL in order to synchronize the timing between the MIR-FEL radiation and the acquisition of the CCD array. The wavelength of the FEL and the macro-pulse energy were 7.9 μm and 3 mJ, respectively. The exposure time on the CCD array was 10 ms, and the observed spectrum was averaged over 90 shots measured at 300 K (room temperature). The repetition rate of the FEL was 1 Hz. A short-pass filter (cut-off wavelength: 1000 μm) and a long-pass filter (cut-off wavelength: 4.5 μm) were used to confirm the harmonics in the FEL beam. If harmonics are contained in FEL beam, then peaks will be observed when the short-pass filter is inserted (Experiment 1), but not when the long-pass filter is inserted (Experiment 2). The background (the spectra measured without FEL and filters) has been subtracted from the spectra in Fig. 4.30.

4-6-3 **Results of the experiments**

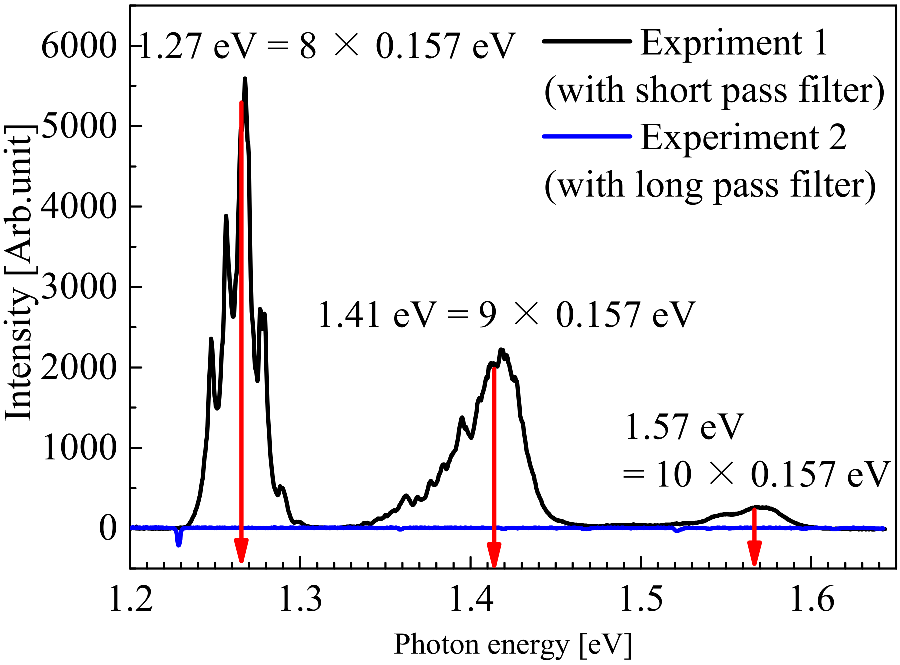

Fig. 4.30. Observed spectrum when a short-pass filter and a long-pass filter are inserted.

Experiment 1 has three broad peaks in addition to the negative peaks that were observed in Experiment 2.

4-6-4 **Discussion**

The center energies of the peaks observed with a short-pass filter are 1.27 eV, 1.41 eV, and 1.57 eV (Fig. 4.30). The center energies of the peaks correspond to the integral multiple of the center energy of the radiated FEL beam (7.9 μm : 0.157 eV), while 1.27 eV, 1.41 eV and 1.57 eV correspond to 8, 9, and 10 times that of 0.157 eV, respectively. When the long-pass filter is inserted, peaks of the energies corresponding to the integral multiple of 0.157 eV are not observed, but negative peaks were observed in the spectrum. The negative peak in the spectrum originates to the background spectrum, which is shown in Fig. 4.31.

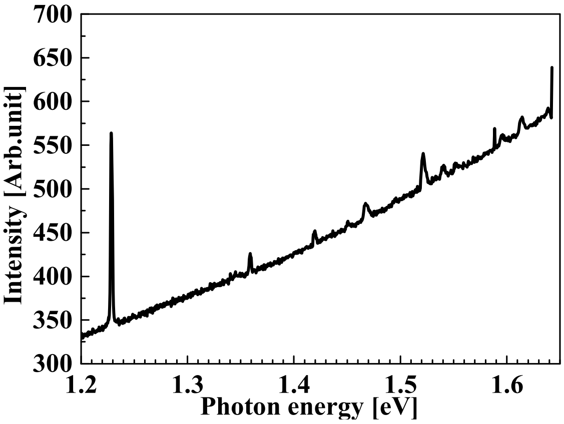

Fig. 4.31. Background spectrum (without FEL and filters).

The peaks shown in Fig. 4.31 are coincident with the emission lines of argon and mercury [96]. Thus, the negative peaks observed in Fig. 4.30 and Fig. 4.31 are due to the emission line of the mercury lamp transported by the mirrors in the FEL beam transport line. From these results, we conclude that the FEL beam contains harmonics, of which the 8th, 9th, and 10th are observed. In addition, the FEL beam contains emissions from the mercury lamp.

4-6-5 **Origin of the harmonics**

Although Section 4-6-4 clarifies the harmonics of the MIR-FEL beam, the origin is unclear. Our FEL beam transport line uses a beam splitter composed of ZnSe in the

FEL quasi-parallel beam system to sample part of the FEL beam. Because ZnSe is a nonlinear optical material [97], MIR-FEL radiation is responsible for the harmonics from the ZnSe window. Therefore, the harmonics may be radiated from the ZnSe window by the MIR-FEL radiation.

Once again, we confirmed the origin of the harmonics using the short-pass filter. The experimental setup is shown in Figure 4.32. A short-pass filter (cut-off wavelength: 1000 nm) was placed after the mirror chamber. Because the fundamental is removed by the short-pass filter, harmonic generation by ZnSe does not occur. Thus, if harmonics are generated in the optical cavity, then they will be observed by this configuration. The parameters of the experimental system are the same as those for the one described in Section 4-6-2.

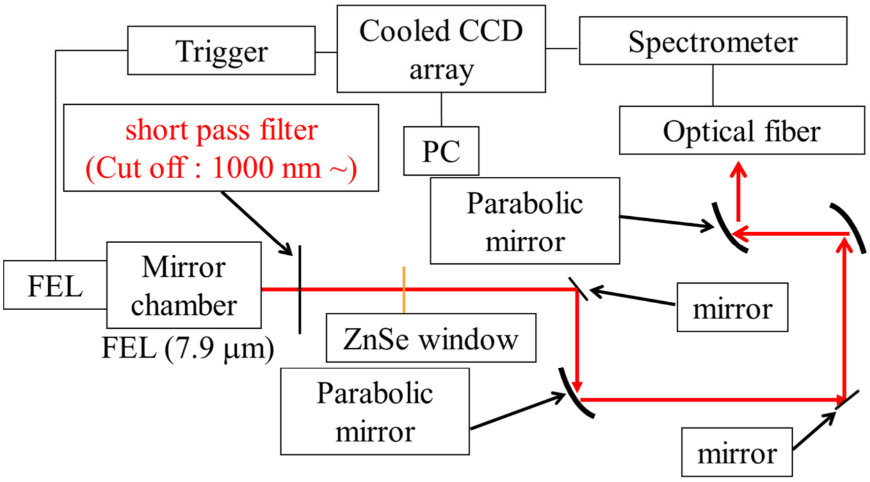

Fig. 4.32. Schematic of the experimental setup.

4-6-5-4 **Result of the experiment**

Figure 4.33 shows the experimental results, where the central wavelengths of the peaks correspond to the integral multiples of the fundamental (7.9 μm: 0.157 eV). The intensity is lower than the measured spectrum in Fig. 4.30 because the FEL beam and parabolic mirrors are not perfectly aligned. These results indicate that the harmonics are generated at the optical cavity of the FEL.

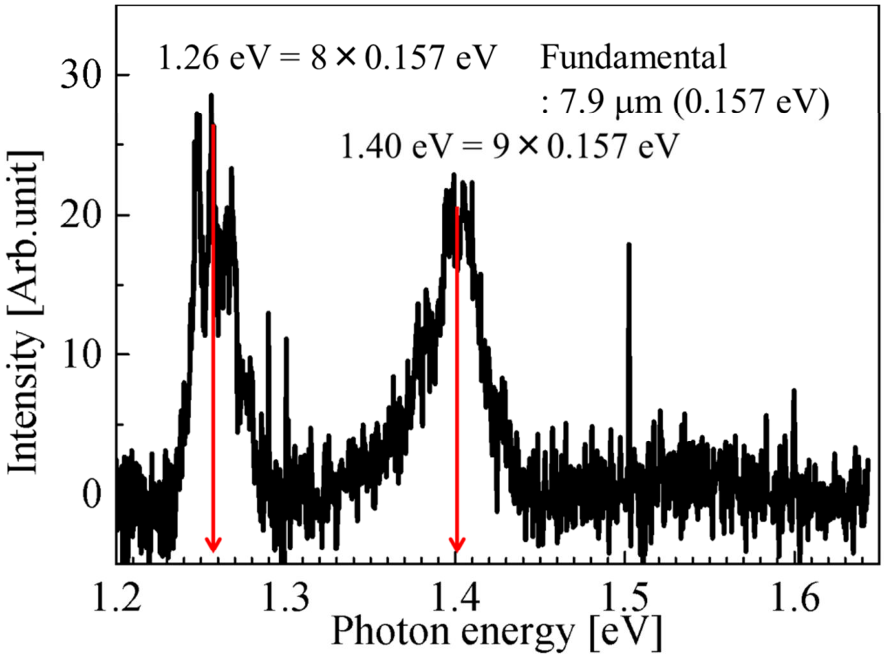

Fig. 4.33. Observed spectrum when the short pass filter is inserted.

In addition, to verify whether harmonics are generated by ZnSe, we measured the spectrum when the FEL beam is radiated onto a ZnSe window using the same parameters described in Section 4-6-2 (Fig. 4.34). Peaks are not observed, which indicates that the harmonics are generated in the optical cavity of the FEL (Fig. 4.35).

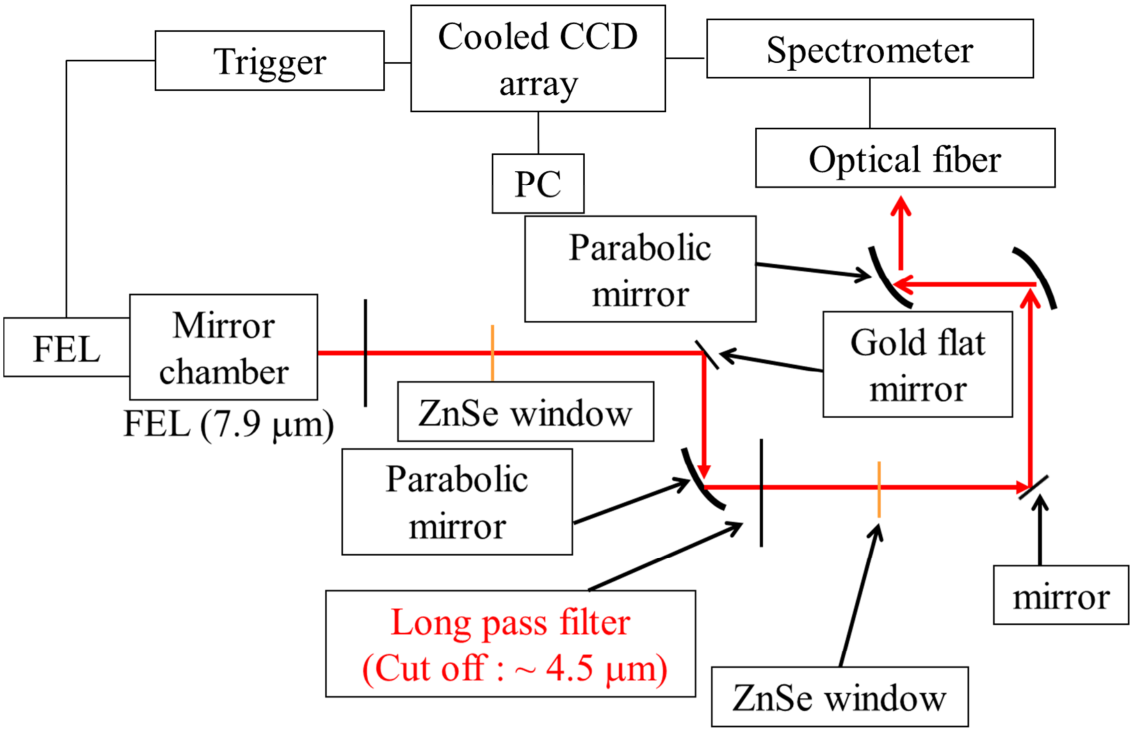

Fig. 4.34. Experimental setup to verify harmonics from ZnSe

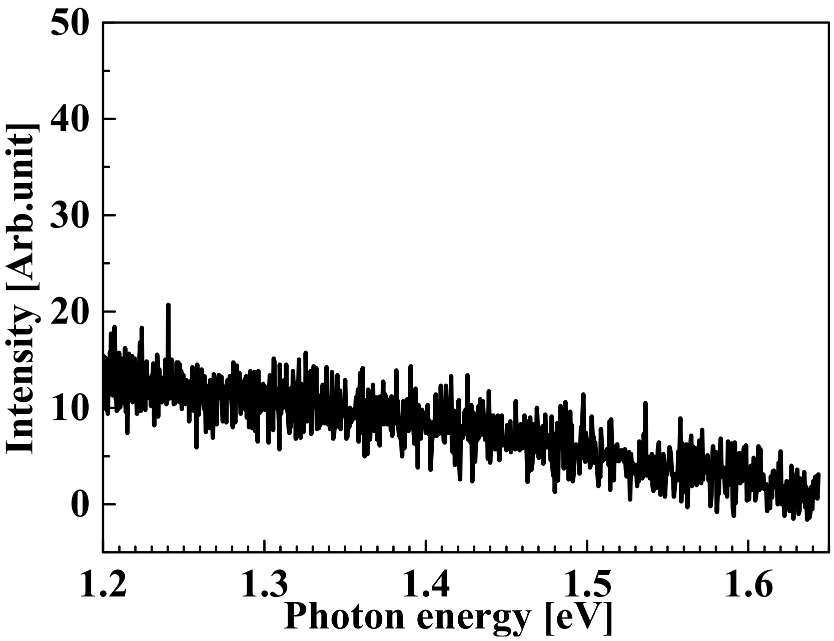

Fig. 4.35. Spectrum from ZnSe.

4-7 **Conclusion**

Calculations and evaluations of the beam size at the user stations were conducted. A spherical mirror with a focal length of 750 mm can be employed in the FEL beam transportation system. The suitable distance between the spherical mirror and the cavity mirror for the quasi-parallel FEL beam is 770 mm. The beam profiles were measured at six points. The beam radii in the horizontal and vertical directions at each measurement point were less than 17.7 mm for a 12-μm FEL beam. From the measured beam radii, the beam waist at the out-coupling hole was calculated to be 0.43 mm in the vertical and horizontal directions, and the distance between the spherical mirror and the cavity mirror was calculated to be 770 mm. Using these values, the beam radius of an FEL beam with wavelength of 20 μm was calculated. From the calculation, it was confirmed that the present parameters, namely, focal length F = 750 mm and distance between the spherical mirror and the cavity mirror d = 770 mm, satisfied the design concept of the FEL quasi-parallel beam system.

The transportation ratios between the accelerator room and user stations A and B were measured for a 12-μm FEL, and found to be 87 % and 73 %, respectively. Contamination by multiple reflections of light expected to be the cause the reduced transportation ratio.

To confirm the effectiveness of N_2 gas filling at preventing the absorption of the MIR-FEL beam by air, the differences of the spectra and the transportation ratio between the cases with and without N2 gas filling were measured. Because the absorption of the MIR-FEL beam was not observed in the FEL spectrum with N_2 gas filling and the transportation ratio was enhanced, it was confirmed that the absorption of the MIR-FEL beam by air could be prevented by using an N_2 gas filling.

We measured a spectrum in the visible region of light to verify of the existence of high harmonics in the FEL beam. As the result, high harmonics up to the 10th were observed, and they were generated in the optical cavity of the FEL. These results show that filters to remove unwanted light are essential when the KU-FEL is used to measure the spectrum of visible light.

5 Direct observation of MSPE

After successfully constructing the user station and verifying the high harmonics within the beam, we experimentally demonstrated mode-selective phonon excitation (MSPE) via mid-infrared (MIR)- free electron laser (FEL) using anti-Stokes Raman scattering spectroscopy.

This chapter is organized as follows. Section 5-1 describes the test material, silicon carbide. The principles and method for demonstration of MSPE via an MIR pulse laser are detailed in Section 5-2. The experimental conditions, including the setup and lasers, are described in Section 5-3 . Section 5-4 outlines the expected experimental results. Section 5-5 presents the results and 5-6 discusses them.

5-1 **Sample material**

The sample material was composed of silicon carbide (SiC), which is a wide-gap semiconductor. There are over 200 kinds of silicon carbide [98]. In particular, 3C-SiC, 4H-SiC, 6H-SiC, and 15R-SiC are famous as materials for wide-gap semiconductor devices, because their physical properties (*e.g.*, electron mobility) are suitable for semiconductor devices. The letters “C”, “ H”, and “R” indicate that the crystal structure is cubic, hexagonal, and rhombohedral, respectively. Figure 5.1 schematically depicts the stacking structure of each silicon carbide poly-type, where “A”, “B”, and “C”, each indicate a layer. For example, the 3C-SiC crystal is stacked in following order:

Layer A→Layer B→ Layer C → Layer A → Layer B → Layer C…

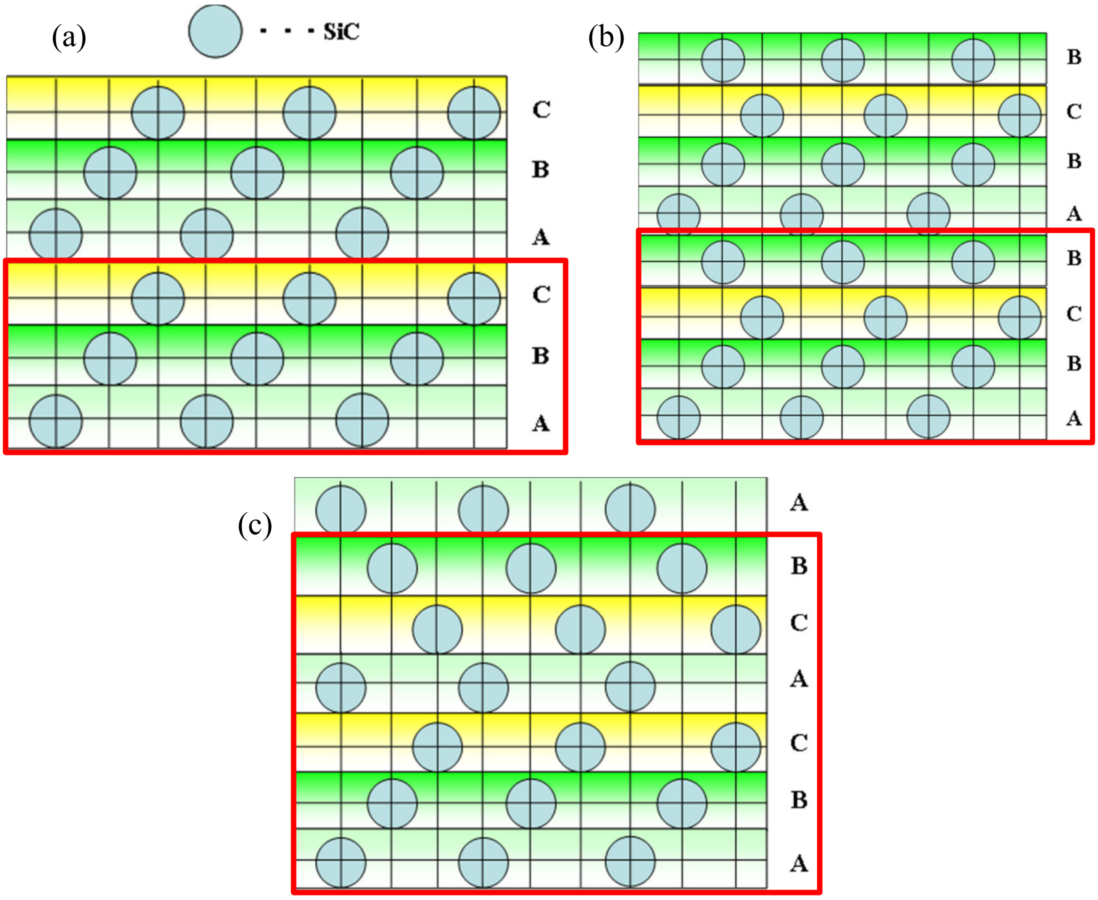

Fig. 5.1. Schematics of the stacking structure in the silicon carbide poly-types, red squares denote a unit layer: (a) 3C-SiC, (b) 4H-SiC, and (c) 6H-SiC.

Silicon carbide is an interesting material in mechanical science, electronics, and materials science. Because silicon carbide is chemically, mechanically, and thermally stable, it has been investigated as a material for the construction of nuclear reactors [99]. In addition, it has been investigated as a replacement for Si-based devices in next-generation power devices, because it has a high breakdown resistance and a wide band-gap [30, 98]. As a functional material, boron-doped silicon carbide exhibits superconductivity [100, 101], while a silicon carbide nanowire exhibits photocatalytic activity [102]. In addition, silicon carbide has been investigated for use as a nonlinear optical material [103, 104].

For silicon carbide devices, it is important to understand electron–phonon interaction, because this contributes significantly to the performance of the devices [30]. When studying this interaction, controlling the phonon excitation is desired.

In this research, we chose 6H-SiC (semi-insulator 6H-SiC : SiC, Xlamen Powerway Advanced Material Co., Ltd) as the sample material, because it is an inexpensive, commercially available, high-quality crystal. In addition, the absorption wavelength of the phonon mode in 6H-SiC is in the tunable range of the KU-FEL. The dimensions of the sample material were 15 mm × 15 mm × 0.33 mm. The SiC (0001) surface was used for the measurements.

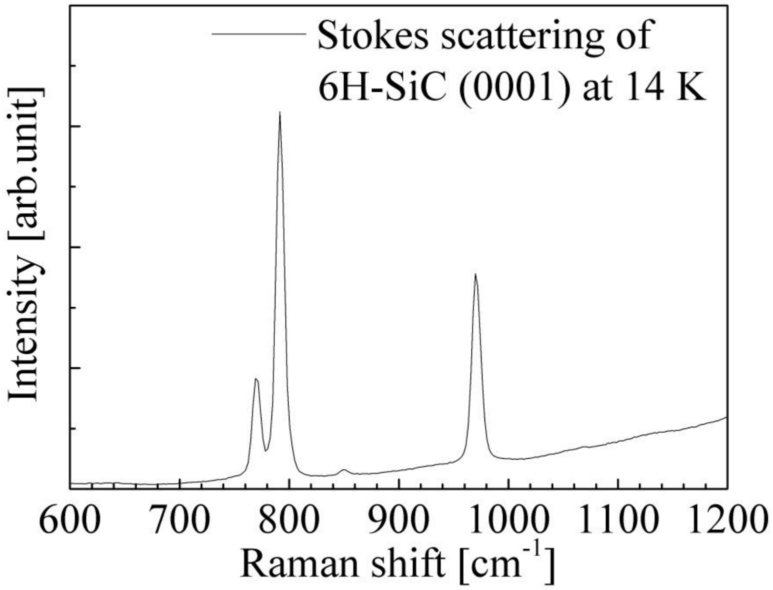

Fig. 5.2. Stokes Raman scattering of 6H-SiC (0001) at 14 K

Figure 5.2 shows the Stokes Raman scattering at 14 K of the sample material, which was measured using a Raman scattering system (Probe: RIP-RPB-785, Ocean Optics, Spectrometer: QE65000, Ocean Optics). The spectrum contains three peaks. The peak at 970 cm^{-1} (10.4 μm) corresponds to the folded longitudinal optical mode at x = 0 (FLO(0)) [38], where x is the reduced wave vector of the phonon modes in the basic Brillouin zone [38], as the lattice of the SiC poly-type becomes superlattice-like owing to the repetition of the layer. The peaks at 790 cm^{-1} and 770 cm^{-1} correspond to the folded transverse optical mode at x = 1/3 and 1, respectively (FTO(1/3) and FTO(1)). A longitudinal optical (LO) phonon mode does not interact with the infrared for normal incident light because the electromagnetic wave is a transverse wave that cannot interact with a longitudinal wave [32]. However, the oblique incidence of the infrared light induces the interaction between the LO phonon mode and the infrared light [105, 106]. Therefore, we chose the FLO(0) phonon mode (10.4 μm) as the target to demonstrate MSPE via irradiation by an MIR-FEL, because the phonon mode FLO(0) is both infrared-active and Raman-active and should be excited by the oblique incidence of the infrared light.

5-2 **Principles and method for demonstration of MSPE via an MIR pulse laser**

In this research, Raman scattering spectroscopy was conducted to demonstrate MSPE via a MIR pulse laser because the state of the phonon is observed directly and simply.

Figure 5.3 demonstrates the principles of MSPE in this research. We hypothesize that the material shown in Fig. 5.3 has three phonon modes. Electrons excited by phonons cause anti-Stokes scattering. The intensity of the anti-Stokes scattering light depends on the electron population in the vibrationally excited state. A hot material has three peaks in the anti-Stokes Raman scattering spectrum (Fig. 5.3 (a)), whereas a cold material does not exhibit anti-Stokes Raman scattering at an adequately low temperature, because the electron population in the vibrationally excited state is too low, even at the lowest-energy excited state (Fig. 5.3 (b)). However, if irradiation by an MIR pulse causes MSPE, then an electron will be excited in a particular vibrationally excited state, even at such a low temperature (Fig. 5.3 (c)). In addition to irradiation by an MIR laser, anti-Stokes Raman scattering light will be emitted if the probe light is irradiated onto the material, because MIR laser radiation generates an electron in the vibration state. For a cold material irradiated by an MIR laser, a single peak should be observed (Fig. 5.3 (c)). Therefore, we can demonstrate MSPE by determining if the peak corresponds to the wavelength of the MIR laser in the anti-Stokes Raman scattering spectrum.

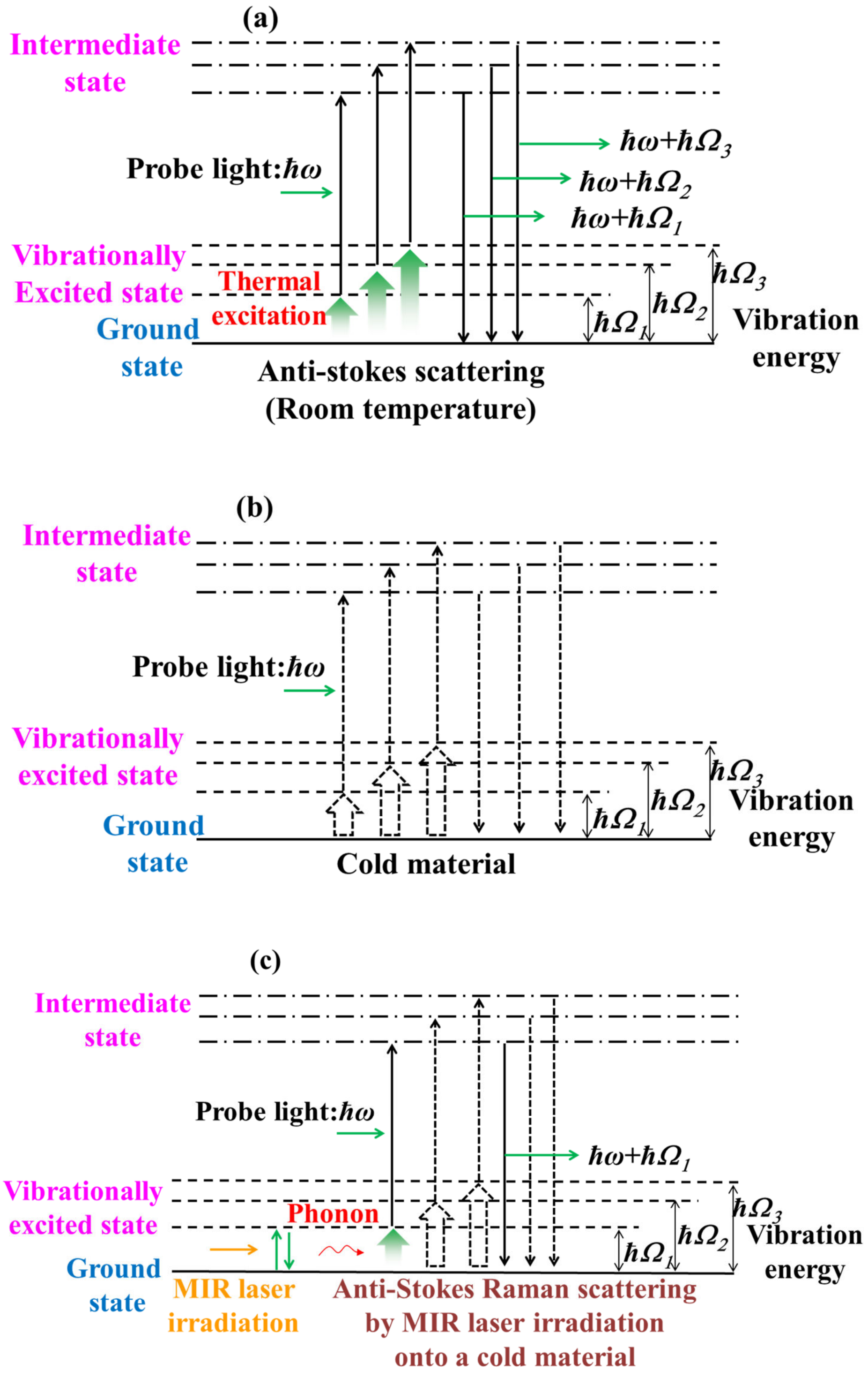

Fig. 5.3. Schematics of the principle of anti-Stokes Raman scattering in (a) a hot material, (b) a cold material, and (c) a cold material via MIR laser irradiation.

5-3 **Experimental setup and conditions**

5-3-1 **Outline of the experimental setup**

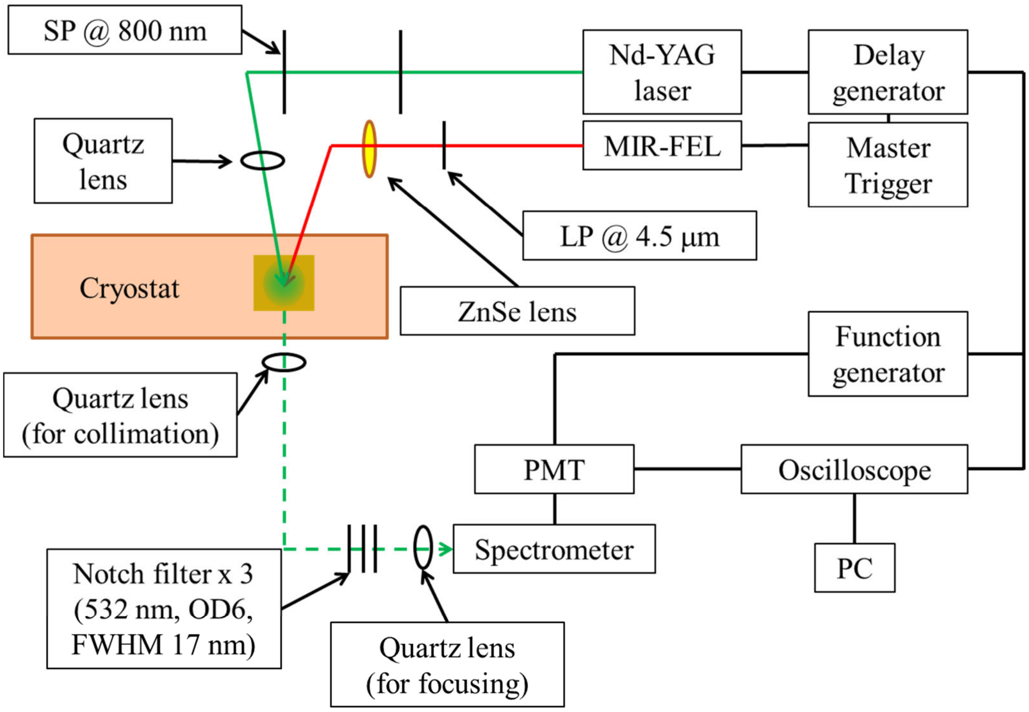

Fig. 5.4. Schematic of the measurement system for anti-Stokes Raman scattering.

Figure 5.4 shows the experiment setup. The probe light was an Nd-YAG laser (Gaia-1. Rayture Systems Co. Ltd). The wavelength, pulse width, and pulse energy were 532 nm (second-harmonic generation), 4 ns (FWHM), and 3 mJ, respectively. The fluence of the Nd-YAG was 130 MW cm^{-2}, and polarization was in the horizontal direction. To remove light from the fundamental wavelength (1064 nm), a short-pass filter (high-performance OD4 short-pass filter, cut-off: 800 nm; ‘SP’ in Fig. 5.4; 64333, Edmund Optics) was installed, while a quartz lens focused the laser onto the sample surface.

A pump laser generated from the KU-FEL was focused onto the sample by a ZnSe lens (f = 200 mm). Prior to the focusing lens, a long-pass filter (LP in Fig. 5.4;

4.50ILP-25, Andover) was installed to remove the inherently generated high harmonics contained in the MIR-FEL. The MIR-FEL was radiated onto the material at an oblique incidence.

The light emitted from the sample was collimated by a quartz lens, and transferred to a spectrometer. Three notch filters removed the light from Rayleigh scattering (532 nm) (two NF533-17, Thorlabs and one StopLine NF03-532E-25, Opto-line). The Raman scattering light was focused on the entrance slit of the spectrometer by a quartz lens. A photon counting method was used to detect Raman scattering light by a spectrometer (Triax 190, Horiba Scientific) and a photomultiplier tube (PMT) with a gating system (R3896 and C1392, Hamamatsu Photonics). A function generator synchronized the gate of the PMT with the master trigger of the KU-FEL, and a closed-cycle helium refrigerator (cryostat : SRDK-205, Sumitomo Heavy Industries, Ltd.) cooled the sample to 14 K. The measurement data was averaged over 100 trials to obtain one measurement point. Figures 5.5, 5.6, and 5.7 show photographs of the experimental setup, cryostat, and spectrometer with PMT, respectively.

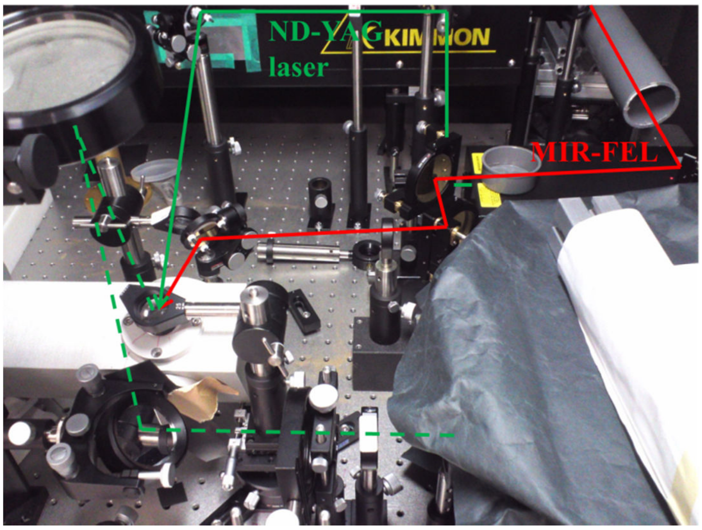

Fig. 5.5. Photograph of the experimental setup.

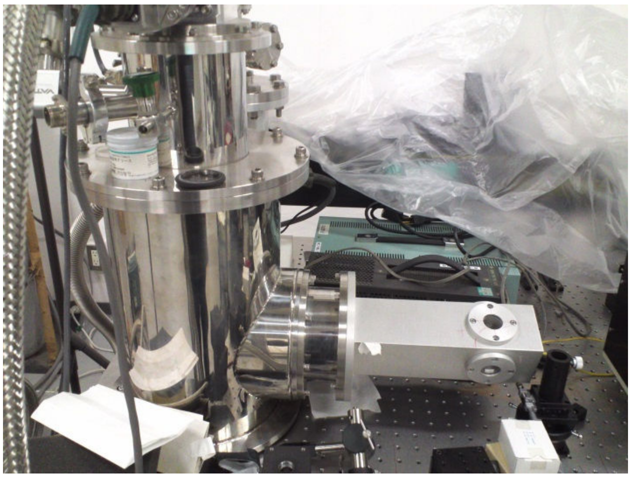

Fig. 5.6. Photograph of the cryostat.

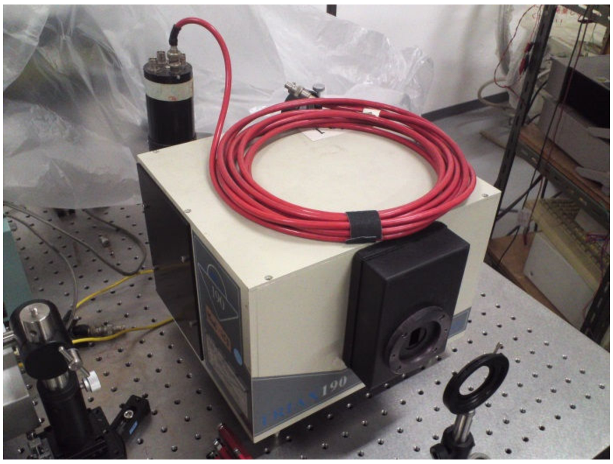

Fig. 5.7. Photograph of the spectrometer and photomultiplier.

5-3-2 **Conditions for the MIR-FEL**

The 6H-SiC has phonon modes that absorb infrared light at energies of 10.4 μm and 12.5 μm [98, 107]. The experiment employed three irradiation wavelengths: 9.05, 10.4 and 12.5 μm. The first, 9.05 μm, was selected to investigate the possibility of sum-frequency generation (SFG) by the MIR-FEL and an Nd-YAG laser. The targeted phonon mode was the folded longitudinal optical mode at $x = 0$ (FLO(0)), which has a corresponding wavelength of 10.4 μm (965 cm^{-1}). The infrared absorption at 12.5 μm corresponds to the folded transverse optical phonon mode at x

= 0, which is indexed as FTO(0) [38, 98]. Table 1 lists the pulse energy, and the fluence of the radiated MIR-FEL at each wavelength.

Table 5.1. Conditions of the radiated MIR-FEL at each wavelength.

Wavelength of MIR-FEL (μm)	Pulse energy (mJ)	Fluence (MWcm^{-2})
9.05	5	1.67
10.4	5	1.67
12.5	1.5	0.5

5-3-3 **Waveforms and timing of each laser**

Figure 5.8 shows the waveforms of the Nd-YAG laser and the MIR-FEL. The black line denotes the trigger of the oscilloscope. The pulse widths of the MIR-FEL (macro-pulse) and the Nd-YAG laser are 2 μs (FWHM) and 4 ns (FWHM) respectively, and the timing between the MIR-FEL and the Nd-YAG laser is synchronized.

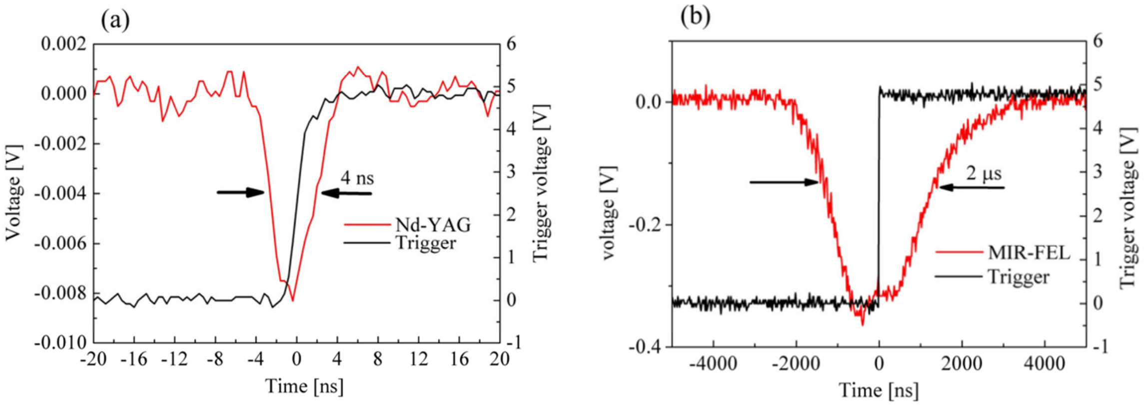

Fig. 5.8. Waveforms and timing of (a) the Nd-YAG laser and (b) the MIR-FEL.

5-3-4 **Relationship between each pulse of the Nd-YAG laser and the MIR-FEL**

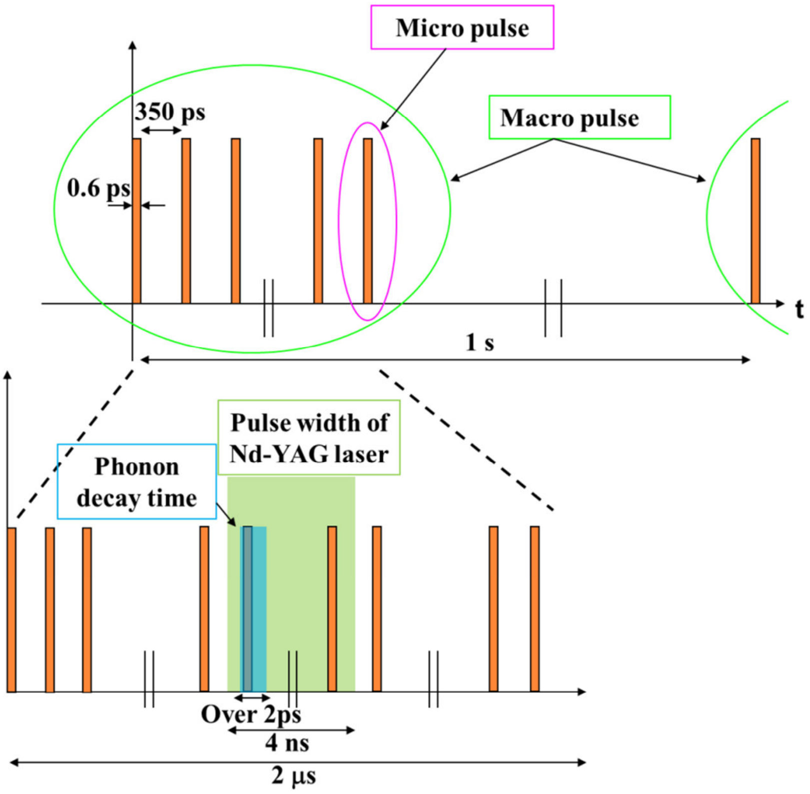

Fig. 5.9. Relationship between the pulse structures of the MIR-FEL and the Nd-YAG laser.

The MIR-FEL, which excites the phonons, has a pulse structure composed of two types of pulses: macro- and micro-pulses (Fig. 5.9). A single macro-pulse in the KU-FEL contains around 5700 micro-pulses. The pulse widths of the macro-pulse and micro-pulse are 2 μs (FWHM) and 0.6 ps (FWHM) at 12 μm, respectively [79,51].

In this experiment, the pulse width of the micro-pulse of the KU-FEL is shorter than the time of the phonon decay time at low temperatures. Therefore, irradiation by the MIR-FEL should induce MSPE owing to a photo-excitation effect.

5-4 **Expected experimental results**

Table 5.2. Expected experimental results when MSPE occurs.

Experiment No.	Wavelength of MIR-FEL (μm)	Temperature (K)	Wavenumber and wavelength of peaks cm^{-1} (μm)
1	Without MIR-FEL radiation	298	965, 787, 767 (10.4, 12.7, 13.0)
2	Without MIR-FEL radiation	14	Not observed
3	10.4 (FLO(0) phonon mode)	14	965 (10.4)
4	9.05	14	Not observed
5	12.5 (FTO(0) phonon mode)	14	Not observed

The expected experimental results for the demonstration of MSPE are shown in Table 5.2. Three peaks will be observed when only the Nd-YAG laser is radiated at 298 K owing to the occurrence of thermal excitation (Experiment 1). However, no peaks will be observed when the Nd-YAG laser is radiated at 14 K, because the phonon excitation is suppressed (Experiment 2).

When the MIR-FEL with 10.4 μm and the Nd-YAG laser are radiated at 14 K, a peak at 965 cm^{-1} will be observed, caused by MSPE (Experiment 3). However, irradiation by the MIR-FEL with 9.05 μm and the Nd-YAG laser will not induce peaks in the spectrum unless SFG is introduced, because 9.05 μm does not correspond to the wavelength of a phonon mode (Experiment 4). The photon energy of 12.5 μm (797 cm^{-1}) corresponds to the energy of a phonon mode (FTO(0)) with Raman-inactive and infrared-active modes in the case of 6H-SiC with the plane direction of (0001). SFG is strong when the energy of the incident laser matches at the vibrational level. Therefore, MIR-FEL radiation with a wavelength of 12.5 μm also works as a sensitive probe to check the possibility of SFG. Additionally, the MIR-FEL with 12.5 μm (797 cm^{-1}) contains a photon of 12.7 μm (789 cm^{-1}) that matches the energy of a phonon mode (FTO(1)) with Raman-active and infrared-inactive modes, because the spectrum width of the KU-FEL is 3%. Therefore, if MSPE is caused by infrared absorption and SFG is not introduced, then no peaks will be observed when the sample is irradiated by the MIR-FEL with 12.5 μm.

5-5 **Results**

5-5-1 **Anti-Stokes Raman scattering at 298 K with and without the MIR-FEL**

To observe the thermally excited anti-Stokes Raman scattering spectrum, which arises from non-MSPE, we measured the anti-Stokes Raman scattering spectrum at 298 K without irradiation by the MIR-FEL. Two peaks are observed (Fig. 5.10). The peak at 970 cm^{-1} corresponds to the FLO(0) phonon mode [38], while the one at 790 cm^{-1} corresponds to the folded transverse optical phonon mode at $x = 1/3$, which is denoted as FTO(1/3) [38]. The FTO(1/3) mode is Raman-active but not infrared-active. Therefore, it is impossible to excite the FTO (1/3) mode using the photo-excitation method. Owing to the bandwidth, the peak at 790 cm^{-1} is considered to contain the peak corresponding to the FTO (1) mode (770 cm^{-1}).

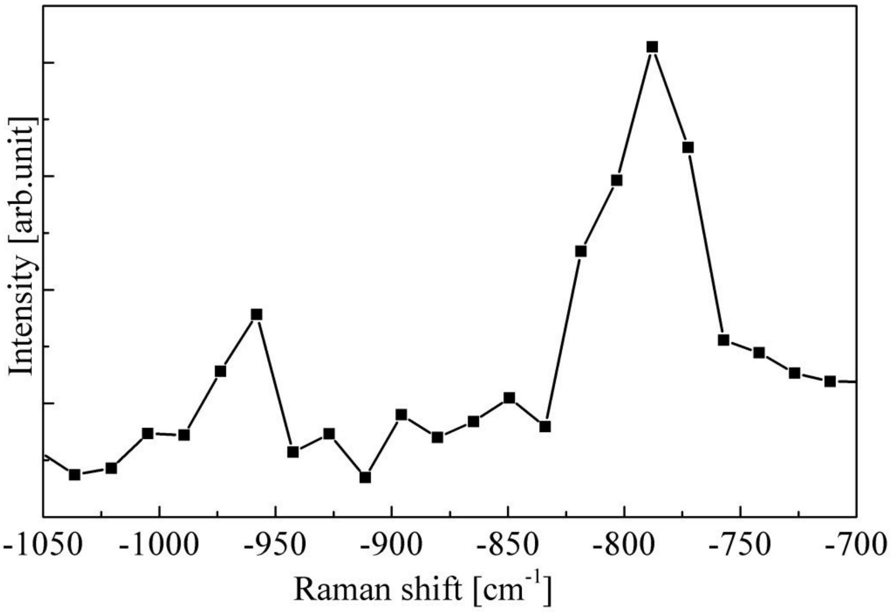

Fig. 5.10. Anti-Stokes Raman scattering spectrum without irradiation by the MIR-FEL at 298 K.

5-5-2 **Anti-Stokes Raman scattering at 14 K with and without the MIR-FEL**

Figure 5.11 shows the anti-Stokes Raman scattering spectra with and without irradiation by the MIR-FEL at 14 K. Tuning the wavelength of the MIR-FEL to 10.4 μm results in a peak at 970 cm^{-1}. When the anti-Stokes Raman scattering without irradiation by the MIR-FEL at 14 K (green open squares in Fig. 5.11) was measured, the peak at 970 cm^{-1} was absent. Additionally, the peaks for the 9.05 and 12.5 μm excitations are not present.

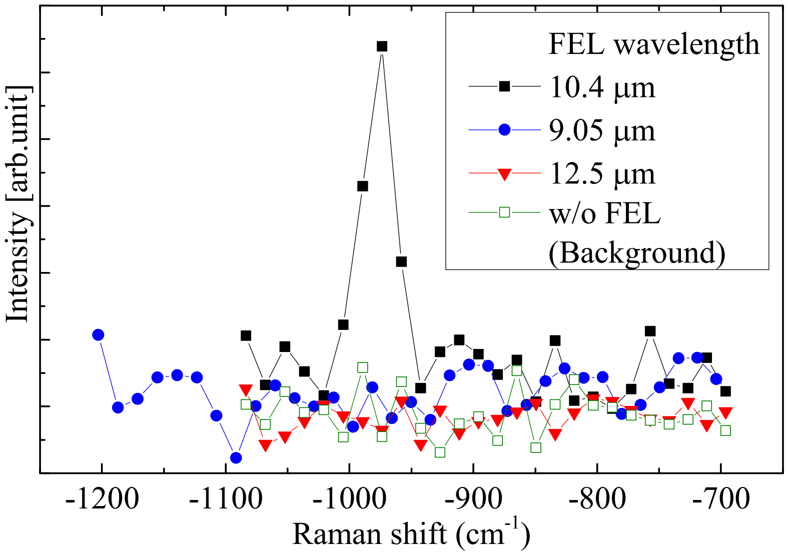

Fig. 5.11. Anti-Stokes Raman scattering spectra with and without irradiation by the MIR-FEL at 14 K.

5-6 **Discussion**

Table 5.3. Results for each experimental condition.

Experiment No.	Wavelength of MIR-FEL (μm)	Temperature (K)	Wave number and wavelength of peaks cm^{-1} (μm)
1	Without MIR-FEL radiation	298	970, 790 (10.4, 12.7)
2	Without MIR-FEL radiation	14	Not observed
3	10.4 (FLO(0) phonon mode)	14	970 (10.4)
4	9.05	14	Not observed
5	12.5 (FTO(0) phonon mode)	14	Not observed

Table 5.3 summarizes the excitation conditions and the observed peaks. Phonons excited by a thermal effect result in two peaks (Experiment 1). However, no peaks were observed when the sample was cooled (Experiment 2). Therefore, we found that phonon excitation by thermal effects is suppressed by cooling.

A peak corresponding to the photon energy of the MIR-FEL is observed in the anti-Stokes Raman scattering spectrum (Experiment 3), but this does not originate from the SFG induced by the MIR-FEL and the Nd-YAG laser (Experiment 4). In addition, the SFG is strong when the energy of the incident laser matches at the vibrational level, as in Section 5-4. Therefore, if the cause of the peak at 970 cm^{-1} in

Experiment 3 was SFG, then a peak at 800 cm^{-1} should be observed when irradiating with the 12.5-μm MIR-FEL, because the photon energy of 12.5 μm corresponds to the energy of FTO(0) phonon mode. However, no such peak is observed, which supports the belief that the peak at 970 cm^{-1} in Experiment 3 does not originate from SFG (Experiment 5). The peak at 970 cm^{-1} is caused by the effect of infrared absorption (by comparison of Experiments 3 and 5). Additionally, because MIR-FEL irradiation is essential to observe the peak at 970 cm^{-1}, the peak is not induced by irradiation by the Nd-YAG laser irradiation (by comparison of Experiments 2 and 3). From these results, it is shown that the peak at 970 cm^{-1} in Experiment 3 is induced by the photo-excitation effect with infrared absorption.

5-7 **Conclusion**

We set out to demonstrate MSPE in a bulk material caused by anti-Stokes Raman scattering spectroscopy, using irradiation by an MIR pulse laser. We selected silicon carbide as our bulk material. The peak at 970 cm^{-1} observed in the anti-Stokes Raman scattering spectrum at 14 K with irradiation by an MIR-FEL is not induced by a thermal effect through laser heating, but instead is a photo-excitation effect. Because the peak is attributed to the selective excitation of the FLO(0) phonon mode by irradiation by the MIR-FEL irradiation, we directly observed MSPE in 6H-SiC using an MIR laser, which was confirmed by anti-Stokes Raman scattering spectroscopy.

6 Summary

6-1 Conclusion

This thesis discussed the mode-selective phonon excitation (MSPE) of a bulk solid material via a mid-infrared (MIR) pulse laser. MSPE is a powerful tool for studying ultrafast dynamics, such as electron-phonon interaction or phonon-phonon interaction. In addition to applications in ultrafast dynamics, MSPE is a useful tool to control the electric and magnetic phases of strongly correlated materials.

Two methods have been reported for MSPE of bulk solid materials: coherent phonon generation (CPG) and an MIR pulse laser. CPG is used to selectively excite a particular phonon in the terahertz region, because the excited phonon mode is limited by the pulse width and the repetition rate of the laser. To selectively excite a particular phonon in the MIR region, an MIR pulse laser has been employed, but, until this work, a direct demonstration of MSPE for a bulk material by an MIR pulse laser had yet to be reported. Therefore, the objective of this thesis was to demonstrate MSPE of a bulk material by an MIR pulse laser.

The Kyoto University Free electron Laser (KU-FEL) was employed as the light source for the MIR laser. To prepare the KU-FEL, the free electron laser (FEL) beam transportation line was first designed and constructed. Then, beam sizes in the FEL beam transportation line and transportation ratios from the accelerator room to the user stations were investigated. Next, the effectiveness of nitrogen (N_2) gas filling in preventing absorption of the MIR-FEL beam by air was investigated. Finally, the origin of high harmonics in the FEL beam was verified. The results of this work are summarized below.

(i) Calculations and evaluations of the beam size at the user stations were conducted. A spherical mirror with a focal length of 750 mm can be employed in the FEL quasi-parallel beam system in the FEL beam transportation system. A suitable distance between the spherical mirror and the cavity mirror for the quasi-parallel FEL beam was calculated to be 770 mm. After the calculations and the construction of the FEL quasi-parallel beam system, the beam profiles at the six measurement points were measured. The beam radii in the horizontal and vertical directions at each measured point were less than 17.7 mm at an FEL wavelength of 12 μm. From the measured beam radii, the beam waist at the out-coupling hole was calculated to be 0.43 mm in the vertical and horizontal direction, and the distance between the spherical mirror and the cavity mirror was calculated to be 770 mm. By using these values, the beam radius of an FEL beam whose wavelength is 20 μm was calculated. From the calculations, it was confirmed that the parameters of the spherical mirror, which had focal length F = 750 mm and distance between the spherical mirror and the cavity mirror d = 770 mm, satisfied the design concept of the quasi-parallel beam system, which makes FEL beam radius less than 17.7 mm at FEL wavelengths of 5 ~ 20 μm.

(ii) The transportation ratios between the accelerator room and user stations were measured at a 12-μm FEL wavelength. The transportation ratios from the accelerator room to user stations A and B were 87% and 73%, respectively. Contamination by multiple reflections of light is expected to have caused the loss of the transportation ratio.

(iii) The differences in the FEL spectra and the transportation ratio with and without nitrogen gas filling were measured. FEL light with a wavelength of 10.6 μm was absorbed by atmospheric air. Possible origins for this included SF_6 used in the beam guide for microwave transportation to accelerate the electron, water vapor excited by the high-power laser, *etc*. However, we demonstrated the effectiveness of N_2 gas filling in transporting 10.6-μm FEL light. Additionally, it was confirmed that the transportation ratio with the N_2 gas filling was three times that without the N_2 gas filling.

(iv) The high harmonics in the FEL beam were confirmed. The 10th harmonic, whose fundamental is 7.9 μm (wavelength 790 nm), was observed in the visible light range. In addition, the emission line of the Hg atom appeared in the spectrum, which likely originated from the mercury lamp used in the accelerator room and the control room. Harmonics were generated in the optical cavity of the FEL. These results show that filters are necessary to remove unwanted light when conducting visible light photoluminescence spectroscopy or Raman scattering spectroscopy.

After the preparation of the KU-FEL, an experiment was conducted to demonstrate MSPE via an MIR pulse laser using a bulk single crystal of 6H-silicon carbide (SiC) as a sample material. Anti-Stokes Raman scattering spectroscopy was performed to demonstrate MSPE via a MIR pulse laser, because the status of a phonon can be investigated directly. Two peaks were observed when the sample was only irradiated by the Nd-YAG laser at 298 K. However, no peaks were observed when it was only irradiated by the probe laser (an Nd-YAG laser) at 14 K. This shows that the thermal excitation of phonon modes in SiC was suppressed by cooling at 14 K. In addition, irradiation by the FEL with a wavelength of 10.4 μm (970 cm^{-1}) at 14 K produces a peak at 970 cm^{-1}. However, irradiation by the FEL at other wavelengths (9.05 μm and 12.5 μm) does not produce any other peaks. Therefore, it was shown that the peak at 970 cm^{-1} appeared only when the photon energy of the MIR-FEL matched the FLO(0) phonon mode (119 meV, 10.4 μm), and the origin of the peak at 970 cm^{-1} was not sum-frequency generation. From these results, it was shown that the observed peak at 970 cm^{-1} was not induced by a thermal effect through laser heating but instead was due to a photo-excitation effect. Because the peak at 970 cm^{-1} is attributed to the selective excitation of the phonon mode in SiC by irradiation by the MIR-FEL, MSPE was thus directly observed using an MIR laser, 6H-SiC, and anti-Stokes Raman scattering spectroscopy.

These results show that the phonon mode can be excited selectively using an MIR pulse laser. Hence, this technique has promise as an effective tool to investigate the ultrafast dynamics of bulk solid materials, as well as to control the electric, magnetic, and insulator phases of strongly correlated materials.

6-2 **Suggestions for future works**

In this research, MSPE via an MIR pulse laser can be demonstrated using silicon carbide with a hexagonal crystal structure (wurtzite). To apply MSPE via an MIR pulse laser more widely, it is important to demonstrate it using other crystal structures (*e.g.*, rutile, zinc-blende, perovskite, *etc.*). In addition, it is important to demonstrate that MSPE can occur using other wurtzite materials (*e.g.*, ZnO, GaN, *etc.*).

It is also important to investigate the polarization dependence of the MIR pulse laser on the intensity of anti-Stokes scattering on SiC, the surface direction dependence, and the population of phonons excited by an MIR pulse laser.

Acknowledgements

Many people contributed to this thesis. Without the help of them, I could not live the daily life as well as writing this thesis. First and foremost, I would like to thank my supervisor, Prof. Hideaki Ohgaki, for his guidance, support, excellent advices and encouragement. In addition, I thank so much that Prof. Ohgaki invited me to Ohgaki lab when I was a student of Master course in institute of chemical research. I am glad that I could belong to Ohgaki lab.

I would like to thank for Prof. Kazunari Matsuda for his meaningful discussion and advices. In addition, when I was a student of master course, he reviewed also my master thesis. Therefore, I want to thank many times.

I would like to thank Prof. Yasuyuki Shirai for his meaningful discussion, guidance and recommendations. By his helps, I could modify and improve this thesis.

I would like to thank for Associated Prof. Toshiteru Kii and Associated Prof. Kai Masuda. In my research life, I could receive precious comments and advices from them. In addition, I could enjoy my research life by their helps.

I would like to thank for Dr. Taro Sonobe, an officer of URA in Kyoto University. My research was started from his ideas and his suggestion. If I did not belong to his research group, my research was not succeeded. In addition, I thank for his help for my daily life. Especially, he gave me many precious advices for daily life as well as research life.

I would like to thank for assistant Prof. Heishun Zen. By his contribution, the FEL operation was very stable and I could start my research. He gave me many recommendations, advices and the many important things as researcher. In addition, he helped my experiment regardless of midnight. I have a great esteem for his kindness.

I would like to thank for assistant Prof. Kan Hachiya. I received many precious advices, meaningful recommendation, and kind help for my research. In addition, I thank for his help on my experiments.

I would like to thank Associated for Prof. Takashi Nakajima. He gave me valuable comments and suggestions. In addition, I could succeed my research by his experimental support and meaningful comments.

Without my friends, I could not spend my daily life and my life would have been much less exciting. I would like to thank for Dr. Ryota Kinjo, Mr. Taiju Kajiwara, Mr. Keisuke Higashimura, Mr. Satoshi Ueda, Mr. Masato Takasaki, Mr, Keiichi Ishida, Mr Naoki Kimura, Mr. Kazuyoshi Hada, Ms. Marie Shibata, Mr. Hidekazu Imon, Mr. Kyohei Shimahashi, Mr Motoharu Inukai, Mr. Kensuke Okumura, Mr. Yusuke Tsugamura, Mr. Kenta Mishima, Dr. M. Bakr, Dr. M. Omer, Mr. Y. W. Choi, and my precious friends.

I would like to thank Ms. Yumiko Nagaya. By her support, I could spend my research life without any trouble.

And last but not least, I would like to thank my family for their aid, support and encouragement.

List of Publications

Peer reviewed publications in scientific journals or international conferences:

Chapter 3

Kyohei Yoshida, et al., Application of MIR-FEL Irradiation to Selectively Excite Phonons in Wide-gap Semiconductors, J. Korean Phys. Soc., Springer, 59 (2011) 3235-3238

Chapter 3

Kyohei Yoshida, et al., Material Analysis Laboratory in KU-FEL, Energy Procedia, Elsevier, 9 (2011) 483-490

Chapter 5

Kyohei Yoshida, et al., Experimental demonstration of mode-selective phonon excitation of 6H-SiC by a mid-infrared laser with anti-Stokes Raman scattering spectroscopy, Appl. Phys. Lett., American Institute of Physics, 103, (2013)182103

Peer reviewed publication as a chapter in a book:

Chapter 4

Kyohei Yoshida, et al., Optimization of the new designed FEL beam transport line, Zero-Carbon Energy Kyoto 2012, Springer, (2012) 205

Proceedings:

1. Kyohei Yoshida, et al., Development of evaluation system for Silicon Carbide by MiR-tunable laser, Proc. of the 7th Annual Meeting of Particle Accelerator Society of Japan (2010), THPS109

2. Kyohei Yoshida, et al., Development of Material Analysis Facility in KU-FEL, Proc. of FEL2011, TUPA02

Oral presentations:

1. Kyohei Yoshida, et al., “Research on MIR-FEL influence on the semiconductor properties”, Atomic Energy Society of Japan Spring meeting, University of Ibaraki, Ibaraki, Japan, 26-28 March 2010

2. Kyohei Yoshida, et al., The investigation of influence to property of wide-gap semiconductor by irradiation of MIR-FEL, (4-5)-November, 2010, 17th International Symposium on Laser Spectroscopy, Deajeon, Korea

3. Kyohei Yoshida et al., Material Analysis Laboratory in KU-FEL, Kyoto University, 25-28 May. 2011, 9th Eco-Energy and Materials Science and Engineering Symposium, Chiang Rai, Thailand

4. Kyohei Yoshida et al., Evaluation of beam transportation line and preparation of experimental station in KU-FEL, 31 January- 1 February, 2011, Ajou-KIT-Kyoto University Joint International Symposium, Ohbaku, Japan,

5. Kyohei Yoshida, et al., Observation of high harmonic generation from SiC by MIR-FEL, 5-8 December, 2012, 10th Eco-Energy and Materials Science and Engineering Symposium 2012, Sunee grand hotel, Ubon-ratchathani, Thailand

6. Kyohei Yoshida, et al., "Demonstration of mode-selective phonon excitation by MIR-FEL with anti-Stokes Raman scattering spectroscopy", 20th workshop of FEL and high-power radiation, University of Nihon, Tokyo, Japan, 13-14 March, 2014

Awards:

1. ***Best poster award***, Kyohei Yoshida, et al., Development of the evaluation system for wide-gap semiconductors by MIR-tunable laser, 21-Auguest, 2010, 8th Eco-Energy and Materials Science and Engineering Symposium, Obaku Plaza, Kyoto

2. **Student award in Institute of Advanced Energy** 7- March, 2014

References

---

[1] T. Kanda, Y. Kato, T. Imai, and K. Tsukiyama, NIM B, 269, (2011)1944

[2] S. Sato, H. Niimi, S. Suzuki, W.-J. Chun, K. Irokawa, Chem. Lett., 33, (2004)558

[3] J. L. Lyman, B. E. Newnam, and J. W. Early, J. Phys. Chem. A, 101, (1997), 49

[4] E. Minehara, T. Yamauchi, Japanese patent 2001-231881

[5] Y. Nakajima, K. Iwatsuki, K. Ishii, S. Suzuki, T. Fujinaka, T. Yoshimine, and K. Awazu, J Neurosurg 104, (2006)426

[6] J. J. Valle, J. R. Eyler, J. Oomens, D. T. Moore, A. F. G. van der, Meer, G. von Helden, G. Meijer, C. L. Hendrickson, A. G. Marshall and G. T. Blakney, Rev. Sci. Instrum., 76, (2005)023103.

[7] Y. Kasai, D. Suzuki, H. Kunugita, and K. Ema, J. Lumin. 129, (2009)1820.

[8]M. Rini, R. Tobey, N. Dean, J. Itatani, Y. Tomioka, Y. Tokura, R. W. Schoenlein, and A. Cavalleri, Nature 449, 72 (2007).

[9] Fundamental and application of photophysics, Association for condensed matter photophysics, Optonics (Japanese)

[10] D. H. Hurley, R. Leis, O. B. Wright, and O. Matsuda, Appl. Phys. Lett. 93, (2008)113101.

[11] K. J. Yee, H. S. Lee, K. G. Lee, and D. S. Kim, Phys. Rev B 74, 113201(2006).

[12] H. Takahashi, K. Kato, H. Nakano, M. Kitajima, K. Ohmori, and K. G. Nakamura, Solid State Commun. 149, (2009)1955.

[13] J.-H. Kim, K.-J. Han, N.-J. Kim, K.-J. Yee, Y.-S. Lim, G. D. Standers, C.J. Stanton, L. G. Booshehri, E. H. Haroz, and J. Kono, Phys. Rev. Lett. 102, (2009)037402

[14] D. C. Heinecke, O. Kliebisch, J. Flock, A. Bruchhausen, K. Kohler, and T. Dekorsy, Phys. Rev. B 87, (2013)075307.

[15] M. Hase, T. Itano, M. Kohji, and S. Nakashima, Jpn. J. Appl. Phys., Part 2, 37, (1998)L281

[16] M. Hase, K. Mizoguchi, H. Harima, S. Nakashima, M. Tani, K. Sakai and M. Hangyo, Appl. Phys. Lett. 69, (1996)2474

[17] K. Watanabe, N. Takagi, and Y. Matsumoto, Phys. Chem. Chem. Phys. 7, (2005)2697.

[18] H.J. Zeiger, J. Vidal, T. K. Cheng, E.P. Ippen, G. Dresselhaus, and M.S. Dresselhaus, Phys. Rev. B, 45, 768(1991)

[19] Lisa Dhar, John A. Rogers, and Keith A. Nelson, Chem. Rev. 94, 157(1994)

[20] H.L. Fragnito,, J.-Y. Bigot, P.C. Becker and C.V. Shank, Chem. Phys. Lett., 160, 101(1989)

[21] M. Forst, R. I. Tobey, S. Wall, H. Bromberger, V. Khanna, A. L. Cavalieri, Y.-D. Chuang, W. S. Lee, R. Moore, W. F. Schlotter, J. J. Turner, O. Krupin, M. Trigo, H. Zheng, J. F. Mitchell, S. S. Dhesi, J. P. Hill, and A. Cavalleri1, Phys. Rev B 84, 241104 (2011).

[22] M. Forst, C. Manzoni, S. Kaiser, Y. Tomioka, Y. Tokura, R. Merlin, and A. Cavalleri, Nat. Phys. 7, 854 (2011)

[23] C. Y. Wang, L. Kuznetsova, V. M. Gkortsas, Optics express, 17, 12929(2009)

[24] M. van der Voort, G. D. J. Smit, A.V. Akimov, J. I. Dijkhuis, N. A. Feoktistov, A. A. Kaplyanskii, A. B. Pevtsov, Physica B 263-264, (1999) 473

[25] M. Bakr, K. Yoshida, K. Higashimura, S. Ueda, R. Kinjo, H. Zen, T. Sonobe, T. Kii, K. Masuda, H. Ohgaki, AIP conference proceedings, 1214, 45(2009)

[26] K. Carlson, W. Fann and J.M.J. Madey, NIM A, 272, 92(1988)

[27] D. J. Bamford and D. A. G. Deacon, NIM A, 285, 23(1989)

[28] Y. Hayakawa, I. Sato, K. Hayakawa , T. Tanaka, K. Yokoyama, T. Sakai, K. Kanno, K. Ishiwata and E. Hashimoto, Jpn. J. Appl. Phys. 41, Suppl. 41-1, 54 (2002)

[29] M. Hase, Ph. D. Dissertation, Osaka University, 1998

[30] K. Kato, K. Oguri, A. Ishizawa, H. Nakano and T. Sogawa, J. Appl. Phys. 111, (2012)113520

[31] M. Hesse, H. Meier B. Zeeh, Spectroscopic Methods in Organic Chemistory, Kagakudoujin, 2005

[32] M. Fox, *Optical Properties of Solids*, Oxford master sedies in condensed matter physics (2010).

[33] W. S. Lau, *Infrared Characterization for Microelectronics*, world scientific, 1999

[34] H. Hamaguchi and A. Hirakawa, Raman spectroscopy, 学会出版センター (Japanese)

[35] L. Bergman, D. Alexson, P. L. Murphy, R. J. Nemanich, M. Dutta, M. A. Stroscio, C. Balkas, H. Shin, and R. F. Davis, Phys. Rev. B, 59, 12977(1999)

[36] R. L. McCreery, *Raman Spectroscopy for Chemical Analysis,* WILEY-INTERSCIENCE 2000. ISBN 0-471-25287-5

[37] S. N. White, Chem. Geol. 259, 240(2009)

[38] S. Nakashima and H. Harima, Phys. Stat. Sol. (a), 169, 39(1997)

[39] M. Nakayama, K. Kubota, T. Kanata, H. Kato, S. Chika, and N. Sano, J. Appl. Phys., 58, 4323(1985)

[40] M. A. Soto, T. Nannipieri, A. Signorini, A. Lazzeri, F. Baronti, R. Roncella, G. Bolognini, and F. Di Pasquale, Opt. Lett., 36, 13, 2557(2011)

[41] Maruzen, experimental chemistry, Chemical Society of Japan

[42] Y. Yao, A. J. Hoffman and C. F. Gmachl, Nature photonics, 6, 432(2012)

[43] K. T. Tsen, D. K. Ferry, A. Botchkarev, B. Sverdlov, A. Salvador, et al., Appl. Phys. Lett. 72, 132 (1998);

[44] A. Matulionis, J. Liberis, I. Matulionienė, H.-Y. Cha, L. F. Eastman, et al. J. Appl. Phys. 96, 6439 (2004)

[45] V. Petrov, Optical Materials, 34, (2012) 536

[46] V. Petrov, F. Rotermund, F. Noack, and P. Schunemann,, Opt. Lett., 24, (1999)414

[47] S. Marzenell, R. Beigang, R. Wallenstein, Appl. Phys. B 69 (1999) 423.

[48] I.M. Bayanov, R. Danielius, P. Heinz, A. Seilmeier, Opt. Commun. 113, (1994)99.

[49] S. Ehret, H. Schneider, Appl. Phys. B 66 (1998) 27.

[50] M.R.X. de Barros, R.S. Miranda, T.M. Jedju, P.C. Becker, Opt. Lett. 20 (1995)480

[51] Y. Qin, et al., Optics Lett., 38, 7, (2013)1068

[52] OperA Solo, Coherent Inc., accessed : 2014/7/10 http://www.coherent.co.jp/laser/femto/amplifier/opa/opera_solo/index.php

[53] Atomic Energy Society of Japan, “ Introductory Book on Free Electron Laser”, August, 1995 (Japanese)

[54] J. Blau, K. Cohn, W. B. Colson and R. Vigil, Proc. of FEL2013, New York, NY, USA, WEPSO01

[55] P. R. Ribic, and G Margaritondo, J. Phys. D: Appl. Phys. 45, (2012)213001

[56] D. Pile, Nature photonics, 5, 8, 456(2011)

[57] N. Sei, H. Ogawa, and K. Yamada, Proc. of Particle Accelerator Socierty Meeting 2009, JAEA, Tokai, pp720-pp722

[58] J. Blau, et al., Proc. of FEL2013, New York, NY, USA, WEPSO01

[59] V. N. Litvinenko, et al., NIM A, 407, (1998)8

[60] S. Adachi, Performance and Science of Energy Recovry Linac (ERL), Science and technology of high pressure, 23, 3, 214(2013)

[61] E. J. Minehara, R. Hajima, H. Iijima, N. Kikuzawa, R. Nagai, N. Nishimori, T. ishitani, M.Sawamura, and T. Yamauchi, Proc. of FEL2005, Livepool, California, USA, C0508213

[62] K. Siegbahn, Ragnar Hellborg, Electrostatic Accelerators: Fundamentals and Applications, Springer, (2005)

[63] M. Yasumoto, “FEL intensity Profile Analysis and Applicatons”, Ph. D Dissertation

[64] K. Imazaki, Laser Research, May, (1998)356 (Japanese)

[65] Murdin, BN, Contemporary Phys., 50, (2009)391

[66] A. Lagutschenkov, J. Langer, G. Berden, J. Oomensbc and O. Dopfer, Phys. Chem. Chem. Phys, 13, (2011)2815

[67] S. Sato, H. Niimi, S. Suzuki, W-J Chun, K. Irokawa, H. Kuroda and K. Asakura, chem. Lett., 33, (2004)558

[68] A. Lagutschenkov, J. Langer, G. Berden, J. Oomensbc and O. Dopfer, Phys. Chem. Chem. Phys, 13, (2011)2815

[69] http://www.differ.nl/research/guthz/felix/highlights#high_2012 : accessed 12/27 2013

[70] H. N. Chapman, et al. Nature, 470, 73

[71] P. G. O’Shea and H. P. Freund, Scince, 292, (2001)1953

[72] J. L. Lyman, B. E. Newnam, J. W. Early and A. F. G. van der Meer, J. Phys. Chem. A 101, (1997)49

[73] N. Yasumoto, T. Tomimasu, NIM A, 480, (2002)92

[74] S. Ogino and K. Awazu, NIM A, 144, (1998)236

[75] Y. Nakajima, et al., J. Neurosurg, 104, (2006)426

[76] H. Zen, "Generation of High Quality electron Beam Using a Thermionic RF Gun for Mid-Infrared Free Electron Lasers", PhD thesis Kyoto University, (2009)

[77] OHO 2013 text (Radio-frequency acceleration), Hirohumi Keigo,

[78] H. Zen, K. Okumura, K. Shimahashi, M. Shibata, H. Imon, T. Konstantin, H. Negm, M. Omer, K. Yoshida, Y.W. Choi, R. Kinjo, M. A. Bakr, T. Kii, K. Masuda, H. Ohgaki, Proc. FEL2012, WEPD38

[79] H. Zen, Y. Tsugamura, M. Inukai, K. Okumura, K. Mishima, K. Torgasin, H. Negm, M. Omer, K. Yoshida, K. Takami, T. Kii, K. Masuda, H. Ohgaki, Poster-10, WIRMS2013, Lorne, Victoria, Australi

[80] H. Zen, Y. Tsugamura, M. Inukai, K. Okumura, K. Mishima, K. Torgasin, H. Negm, M. Omer, K. Yoshida, K. Takami, T. Kii, K. Masuda, H. Ohgaki, WIRMS2013

[81] T. Tomimasu, et al., Nucl. Instr. and Meth. Phys. Res. A. 407, (1998) 494

[82] P. J. Colwell, et al., Phys. Rev. B 6, (1972) 498

[83] K. Nomaru, M. Kawai, M. Yokoyama, F. Oda, A. Nakayama, H. Koike, H. Kuroda, NIM A, 445, 379(2000)

[84] D. Oepts, A. F. G. Van Der Meer and P. W. Van Amersfoot, Infrared Phys. Technol.36, 297(1995)

[85] K. Saeki, E. Nishimura, A. Kobayashi, S. Abe, A. Zako, M. Yasumoto, T. Tomimasu, NIM A, 358, ABS 56(1995)

[86] M. Bakr, K. Yoshida, K. Higashimura, S. Ueda, R. Kinjo, H. Zen, T. Sonobe, T. Kii, K. Masuda, H. Ohgaki, AIP conference proceedings, 1214, 45(2009)

[87] H. Ohgaki, T. Kii, K. Masuda, M. A. Bakr, K. Higashimura, R. Kinjo, K. Yoshida, S. Ueda, T. Sonobe, H. Zen, and Y. U. Jeong, Proc. of FEL2009, Livepool, UK, WEPC35

[88] C. C. Ferriso, et al, J. Quant. Spectrosc. Transfer, 6, 241(1966)

[89] Global optics web site, http://www.globalopticsuk.com/KRS-5.htm, accessed : 2014/6/16
[90] crystal techno web site, http://www.crystaltechno.com/Cu_en.htm, accessed : 2014/6/16
[91] Thorlabs web site, http://www.thorlabs.co.jp/NewGroupPage9.cfm?ObjectGroup_ID=264, accessed : 2014/6/12
[92] C. C. Ferrisot, C. B. Ludwig and A. L. Thomson, J. Quant. Specrrosc. Radiat. Transfer. 6, 241(1966)
[93] H. Brunet, J. Q. E., 6, 11, 678(1970)
[94] E. R. Pugh and R. H. Krech, AIAA Jurnal, 20, 6, 863(1982)
[95] B. Girard, Y. Lapierre, J. M. Ortega, C. Bazin, M. Billardon, P. Elleaume, M. Bergher, M. Velghe, and Y. Petroff, PRL, 53, 25, 2405(1984)
[96] Joseph Reader, Charles H. Corliss, W. L. Wiese and G. A. martin, Wavelengths and Transition Probabilities of Atoms and Atomic Ions, NSRDS-National Bureau of Standards #68, 1980
[97] A. H. Chin, O. G. Calderón and J. Kono, PRL, 86, 3292(2001)
[98] H. Matsunami, Technology of Semiconductor SiC and Its Application, Nikkan Kogyo Sinbunsya(2010) (Japanese)
[99] R. Naslain, Compos. Sci. Technol., 64, 155(2004)
[100] J. Noffsinger, F. Giustino, S. G. Louie, and M. L. Cohen, Phys. Rev. B 79, 104511(2009)
[101] Z.-A. Ren, J. Kato, T. Muranaka, J. Akimitsu, J. Phys. Soc. Jpn., 76, 103710(2007)
[102] W. Zhou, L. Yan, Y. Wang, and Y. Zhang, Appl. Phys. Lett. 89, 013105 (2006)
[103] P. M. Lundquist, W. P. Lin, G. K. Wong, M. Razeghi, and J. B. Ketterson, Appl. Phys. Lett. 66, 1883 (1995)
[104] S. Niedermeier, H. Schillinger, R. Sauerbrey, B. Adolph, and F. Bechstedt, Appl. Phys. Lett. 75, 618 (1999).
[105] K. HUBNER, L. SCHUMA, A. LEHMA, H.H. VAJEN, and G. ZUTHER, phys. stat. sol. (b) -104, (1981)Kl

[106] H. Ohyama, T. Suzuki, K. Nishi, T. Mitsuyu, and T. Tomimasu, Appl. Phys. Lett., 71, (1997)823

[107] W. G. Spitzer, D. Kleinman, and D. Walsh, Phys. Rev. 113, 127 (1959)